Alma Mater Studiorum · Università di Bologna

Scuola di Scienze
Dipartimento di Fisica e Astronomia
Corso di Laurea Magistrale in Fisica

Electrical Contact Properties of Ultrathin Transition Metal Dichalcogenide Sheets

Relatrice:
Prof.ssa Daniela Cavalcoli

Presentata da:
Lorenzo Gorini

Correlatore:
Prof. Klaus Kern

Correlatore:
Dr. Marko Burghard

Anno Accademico 2017/2018

Abstract

The graphene discovery led to advances in exfoliation and synthetic techniques, and the lack of a bandgap in graphene has stimulated the research for new 2D semiconducting materials. Transition metal dichalcogenides (TMDCs), semiconductors of the type MX_2, where M is a transition metal atom (such as Mo or W) and X is a chalcogen atom (such as S, Se or Te), have recently been isolated. TMDCs exhibit a unique combination of atomic-scale thickness, strong spin–orbit coupling and favourable electronic and mechanical properties, which make them interesting for fundamental studies and for applications in high-end electronics, spintronics, valleytronics and optoelectronics.

According to optical measurements, single-layer WS_2 sheets exhibit a direct band gap of at least 2.0 eV [1]. Because of its strong spin-orbit coupling induced valence band splitting, [2] WS_2 shows spin-valley coupling, even in few-layer sheets [3], which may allow easier observation of the valley Hall effect than in the other TMDCs.

The thesis reviews the theoretical background of TMDCs and their optoelectronic properties. It also reports on the fabrication of field-effect transistors based on few-layer sheets of WS_2 and the investigation of their electronic transport properties. Particularly the project focuses on improving the interface between the metal contact and WS_2 sheet, where annealing improves the contact transparency. Together with van der Pauw geometry, annealing allows four-terminal measurements to be performed and the pristine properties of the material to be recovered at room temperature, where the devices show n-type behaviour and a linear I-V curve.

The promising improvements and the electronic properties shown in this thesis make WS_2 interesting for future applications in valleytronic devices.

Contents

1 Introduction

Technology is omnipresent in daily life. In the past years, the relentless research has focused on miniaturization of the silicon-based electronics. Data processing, infact, relies upon binary bits to encode information, with the bits "1" and "0" representing the *on* and *off* states. Since the computational power depends on the integration density of transistors, according to Moore's law, the exponential increase of transistor density over the years goes along with improved computing efficiency and higher memory density, leading to increased storage capacity for minimized production and storage costs. Impressively, while the first Intel processor fabricated in 1971 contained 2300 transistors, in modern processors this number exceeds staggering 10 billion transistors [4].

From smartphones to wearables and the Internet of Things, the downsizing of transistors led to higher current densities and gate leakage currents. Hence, the scientists' attention has shifted towards strategies to solve problems like higher power consumption and higher heat production, both of which slow down further innovation. These huge efforts have led to the realization of the *3D MOSFET* by Intel [4], and of chipsets with channel lengths down to 7 nm [5] by Huawei in 2018, allowing the processor computation capability to further obey Moore's law. This latest commercialized version of the so called "finFETs" (namely, fin-Field Effect Transistors) was achieved already in 2000. Afterwards, it became apparent that this approach will reach its limit due to the increasing difficulty to control the quantum behaviours that are becoming predominant, and due to the intrinsic limits of silicon. In the meanwhile, the scientific community has therefore shifted focus toward new materials and approaches like vacuum transistors, carbon nanotube transistors [6], silicon photonics [7], phosphorene and organic semiconductors [8].

Historically, the dawn of classical valleytronics is associated with studies in the late 1970s on two-dimensional (2D) electron gases in silicon inversion layers [9][10], which examined the roles of valley degeneracy and inter-valley coupling in various contexts. In particular, theory predicted that at low densities in the inversion layer, the electron

intravalley exchange and correlation could lead to a spontaneous valley polarization where the electrons preferentially occupy one valley. In analogy to spin ferromagnetism, such formation of *valley ferromagnetism* suggests that the valley pseudospin might also be exploited for non-volatile information storage.

Subsequent studies achieved effective control over valley pseudospin in a number of material systems, including aluminium arsenide quantum wells, silicon heterostructures, diamond and bismuth [11]. However, the ability to control valley pseudospin was limited owing to the lack of intrinsic physical properties associated with valley occupancy. This limitation stood in contrast to the versatile means available to control electron spin, for example, by magnetic fields through the spin magnetic moment, by electric fields through spin-orbit coupling, or by optical fields via momentum transfer from the photons.

Novel opportunities were opened up in 2006, when Novoselov and Geim discovered the fascinating properties of graphene (a monolayer of graphite). The isolation of graphene was enabled by the weak interlayer bonds in graphite, allowing its exfoliation into monolayers. Transition metal dichalcogenides (TMDCs) host similarly weak van der Waals interlayer interactions, and hence can likewise be exfoliated into monolayers.

The discovery of the new 2D materials, together with the interest in the valley index as another binary quantum degree of freedom of electrons (which may be viewed as pseudospin), triggered numerous investigations on TMDCs. According to theoretical studies, spatial inversion symmetry breaking in monolayer TMDCs may couple valley occupancy to electric and magnetic fields and to polarized light, thus enabling to create valley currents. In this manner, valley pseudospin control could be achieved in analogy to the control over the electron spin. The quantum effects associated with the new degree of freedom may open up remarkable possibilities in the field of *valleytronics*, where the valley index is used as binary value.

The holy grail of valleytronics is the realization of a quantum computer, in which the classical binary bits are replaced by the two possible values of the valley index, and logical operations are performed based upon a linear superposition of the two. The resulting *qubits* could provide access to unprecedented computational power for applications in cryptography or quantum simulation by exploiting parallel computational capability, whereas conventional computers can perform only one task at a time.

The strive towards quantum computation is driven by the aim to understand, generate and control electrons with a specific valley index in solid state devices. In fact, different valley indices are associated with different Berry curvature, thus allowing to generate pure valley currents in TMDCs by illuminating them with circularly polarized light. This process may also be used to transfer information from one transistor to another.

On this basis, modern valleytronics research envisions the following aims: (i) engineering of materials with improved properties, which can generate and host valley currents by providing high valley polarization and long valley coherence times; (ii) achieving efficient conversion between polarized light and valley currents; (iii) developing and optimizing all-electric techniques to create and manipulate valley accumulation. Progress along

these directions would have great potential to revolutionize current technologies towards all-valley-based information processing.

The present thesis set out to explore the magnetotransport properties of ultrathin TMDC sheets, with focus on WS_2. This compound was chosen due to its remarkable band splitting for the different valley index values, even for sheets that comprise not only one but several layers. A major focus was on improving the interface between the metal contacts and the semiconductor, in order to demonstrate the suitability of WS_2 as valley current generator in valleytronics devices.

The thesis is organized as follows.

Chapter 2 provides a brief overview of the physical and electronic structure of TMDCs and their interaction with light, and it furthermore highlights recent experimental studies on the interface between TMDCs and metals.

Chapter 3 describes the experimental methods employed in this work and provides details on WS_2 device fabrication and measurement techniques. Chapter 4 presents the results of the magnetotransport experiments, with a focus on the achieved improvements of the contact quality. Furthermore, the material resistance, as well as carrier mobility and concentration are compared to values found in previous studies as a function of temperature. Chapter 5 concludes this thesis with a short summary of the gained results and an outline of possible future experiments.

2 Structural and electronic properties of Transition Metal Dichalcogenides

2.1 Transition Metal Dichalcogenides

Transition metal dichalcogenides (TMDCs) have a long and intriguing history. Linus Pauling first determined their structure in 1923 [12] and in the late 1960s almost 60 TMDCs were already known [14]. The first production of monolayer MoS_2 has been reported in 1986 [15]. Since the discovery of graphene in 2004 [17], the development of manipulation techniques for layered materials has stimulated novel studies on TMDCs, and increasing attention has been directed to alternative 2D materials different from graphene. Thus far, only a small fraction of the available layered van der Waals solids has been isolated as air-stable, high-quality, two-dimensional semiconductors. TMDCs are among the most studied of this list, especially in their monolayer form [18]. They provide a whole new testbed for exploring the internal quantum degrees of freedom of electrons, like the layer pseudospin and the valley pseudospin. Particularly the Berry phase-related physical properties and strong spin-orbit coupling open new perspectives for the quantum control of the spin and pseudospins. The former enables the versatile control of the valley pseudospin, whereas the latter allows an interplay between the spin and pseudospin. [11] The present chapter gives a brief introduction to the properties of TMDCs.

2.2 Crystal Structures

TMDCs have the chemical formula MX_2, where M is a transition metal and X is a chalcogen. In bulk TMDCs, the layers are stacked through van der Waals forces. Although these forces are relatively weak, TMDC monolayers and multilayers often display different physical properties (which can also arise from changes of symmetry).

2.2.1 Monolayer Structure

A TMDC monolayer is characterized by a hexagonally ordered plane of metal atoms between two layers of chalcogen atoms, with the formal oxidation states of +4 for the metal and -2 for the chalcogen, see fig. 2.1(a).

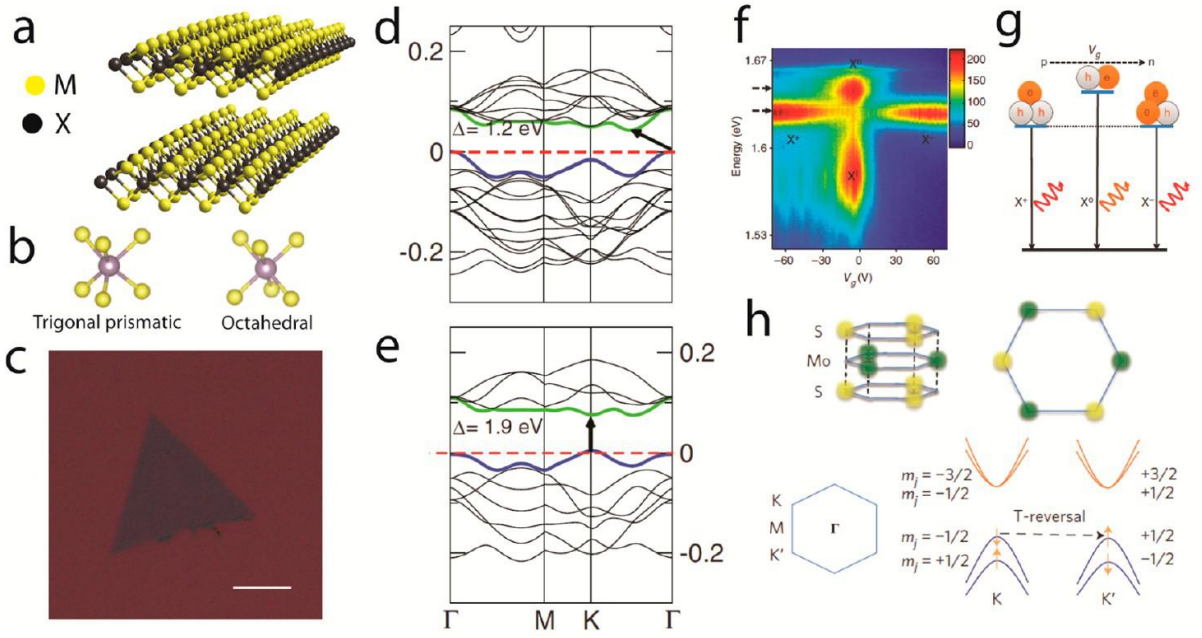

Figure 2.1: *Physical properties of layered semiconducting transition metal dichalcogenides (TMDCs). (a) Chemical structure of two layers of a TMDC where M is a transition metal and X is a chalcogen. (b) Two polytypes of single-layer TMDCs: trigonal prismatic (1H) and octahedral (1T). (c) Optical micrograph of single-layer MoS2 on a 300 nm SiO_2/Si substrate (scale bar = 20 μ m). (d) Band structure of bulk MoS_2 and (e) single-layer MoS_2 as calculated from density functional theory. (f) Photoluminescence energy of single-layer $MoSe_2$ plotted as a function of gate voltage. At zero gate voltage, there are neutral (X^0) and impurity-trapped excitons (X^I). With large electron and hole doping, charged excitons (trions) dominate the spectrum. (g) Schematic of a gate-dependent transition of a positive trion (X^+) to a neutral exciton and then to a negative trion (X^-). (h) Top: Honeycomb lattice of single-layer MoS_2 where alternating corners are occupied by one Mo and two S atoms, resulting in broken spatial inversion symmetry. Bottom: Conduction band minima and valence band maxima are shown with corresponding z-components of their total angular momentum. The valence bands are split due to strong spin-orbit coupling. Adapted from [18] .*

Each layer has a thickness of 6-7 $\AA$ with strong in-plane covalent bonding and weak out-of-plane van der Waals interactions. It is the former in-plane bonds that ensure the air stability of many TMDC monolayers. TMDC monolayers exist in two main structural phases, namely trigonal prismatic or octahedral, wich are distinguished by the position of the chalcogen within the coordination sphere of the transition metal atoms [19]. The former has a D_3h point group of symmetry, resulting in a honeycomb lattice (denoted

as 1H for monolayer), and the latter has a D_3d point group, with a centered honeycomb lattice (denoted as 1T). For semiconducting TMDCs, commonly the 2H polytype is the thermodynamically stable phase, although there are some exceptions (like WTe_2) and reversible transition to the 1T polytype can be induced by chemical processing. [20]

The thinner the sheet thickness, the lower the interference effects (fig. 2.2 and this is why identifying monolayers is very difficult for some TMDCs (like WS_2) since they interact very little with the light.

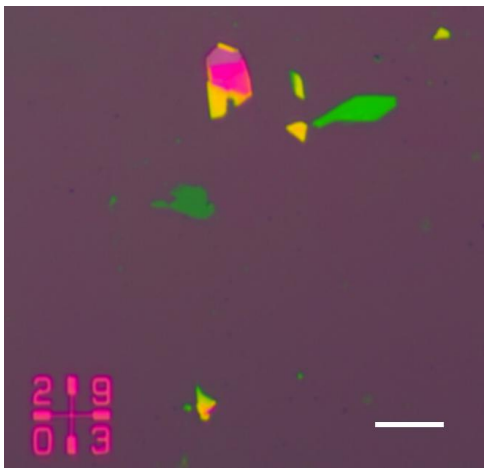

Figure 2.2: *Optical image of WS_2 flakes on a Si/SiO_2 substrate. The long and light green flake is about 6 nm thick, while the dark green one is about 3.5 nm thick. The scale bar is 10 μm.*

2.2.2 Multilayer Structure

Bulk TMDCs are distinguished by the stacking configuration of the contained layers. As shown in figure 2.3, there exist three different lattice types: 1T, 2H and 3R. While the 2H structure is the most abundant, bulk TMDCs may comprise all three types combined within the crystal. Structural distortions can also be present, resulting in the formation of metal-metal bonds, sometimes accompanied by charge density wave phases [33].

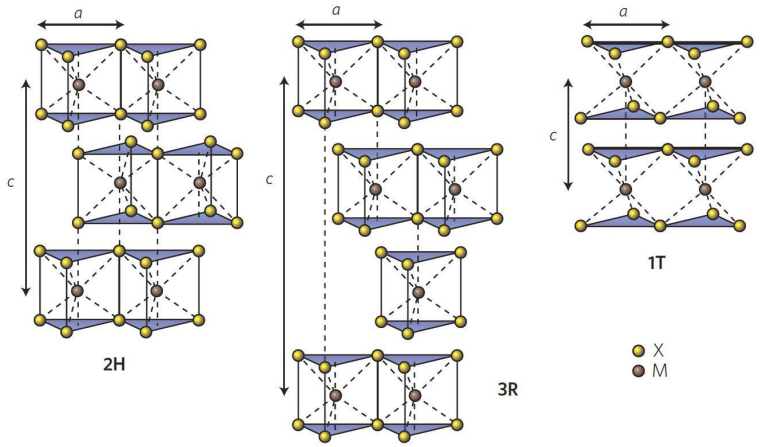

Figure 2.3: *Schematic depiction of the three different structural polytypes of TMDCs, specifically 2H (hexagonal symmetry, two layers per repeat unit, trigonal prismatic coordination), 3R (rhombohedral symmetry, three layers per repeat unit, trigonal prismatic coordination) and 1T (tetragonal symmetry, one layer per repeat unit, octahedral coordination). The chalcogen atoms (X) are yellow and the metal atoms (M) are grey. The lattice constants a are in the range 3.1 to 3.7 Å for different materials. The stacking index c indicates the number of layers in each stacking order, and the interlayer spacing is ≃6.5 Å. Adapted from [21] .*

Figure 2.4: *Photograph of bulk MoS_2 crystal, which is approximately 1 cm long.*

2.3 Electronic Properties of WS_2

2.3.1 Band Structure

Recent experiments and theoretical calculations [34] have demonstrated that certain TMDCs undergo transformation from an indirect band-gap semiconductor in the multi-layer form to a direct band-gap in the monolayer form (see fig. 2.9). The direct band gap is in the visible frequency range, which is relevant for optoelectronic applications.

The band structure of monolayer 1H-MX_2 in figure 2.6 has been obtained by Density Functional Theory (DFT) calculation along the high symmetry points $\Gamma - M - K - \Gamma$ in the Brillouin zone [34] (see fig. 2.5). In the case of 2H-MX_2, the conduction band minima are located between the Γ and K high symmetry points, while valence band minima occurr at the Γ point, revealing the indirect band gap of bulk MX_2.

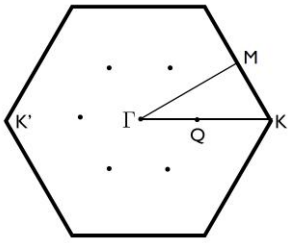

Figure 2.5: *Two dimensional Brillouin zone of MX_2. The high symmetry points $\Gamma = (0;0)$, $K = 4\pi/3a(1;0)$ and $M = 4\pi/3a(0;\sqrt{3}/2)$ are shown. The Q points (which are not high symmetry points) indicate the position of the edges of the conduction band in multilayer samples. Adapted from [23].*

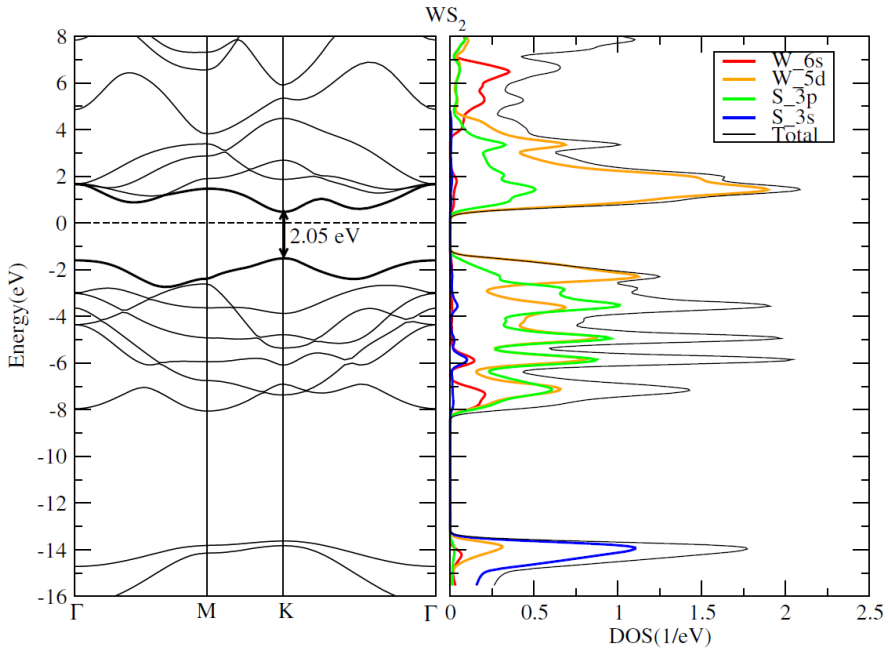

Figure 2.6: *Electronic band structure and corresponding total and partial density of states of 1H-WS2. The direct band gap is 2.05 eV, and occurs at high symmetry point K. All the partial DOS are multiplied by 1.5. The Fermi level is set at 0 eV. Adapted from [34].*

As a consequene of quantum confinement, as the number of layers decreases, the indirect band gap increases (blue shift). By comparison, the magnitude of this increase

Table 2.1: *Comparison between the blue shift of the indirect band gap energies and the one from the direct band gap, when thinning down the materials listed from bulk up to monolayers.*

Material	Blue shift in indirect band gap energies	Blue shift in direct band gap energies
MoS_2	1.14 eV	0.19 eV
WS_2	1.16 eV	0.16 eV
$MoSe_2$	0.78 eV	0.11 eV
WSe_2	0.64 eV	0.12 eV
$MoTe_2$	0.57 eV	0.18 eV
WTe_2	0.37 eV	0.14 eV

is significantly smaller for the direct band gap at the K point (see table 2.1). Similar theoretical values were obtained using Gaussian basis functions [24].

These results confirm the transition from an indirect band gap to a direct one, as the TMDCs are thinned down to a monolayer. In other studies, DFT-derived values have been compared to values obtained by the tight-binding (TB) model [23]. As it can be seen from fig. 2.7, there are some slight differences between the two models, although the main characteristics are in good agreement with each other and the previous results.

As tungsten is a heavier element than molybdenum, the former exhibits a stronger spin-orbit coupling (SOC). There are also some differences between sulphides and tellurides, in particular because sulphur has a larger electronegativity than tellurium. Thus, for the sulphides, the orbital radius is reduced and the effects of the chalcogen ligand field become less pronounced, resulting in narrower d-bands and a larger band gap, as compared to the tellurides.

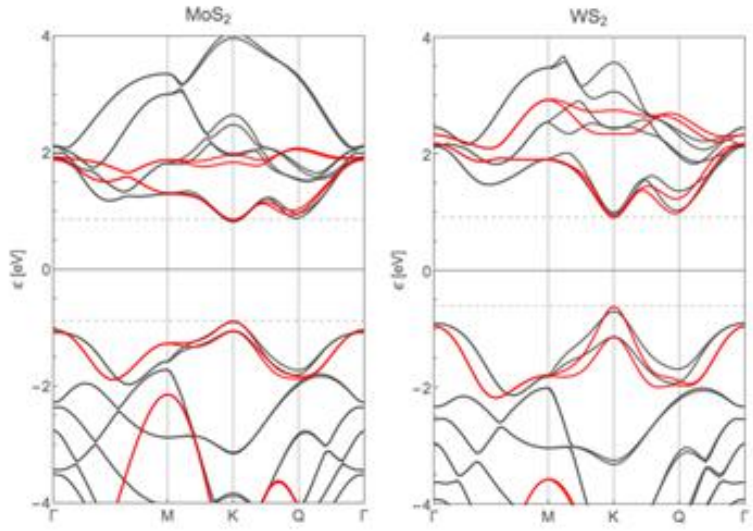

Figure 2.7: *Electronic band structure of single-layer MoS_2 and WS_2 obtained by DFT calculation (black lines) and tight-binding (red lines). Adapted from [35].*

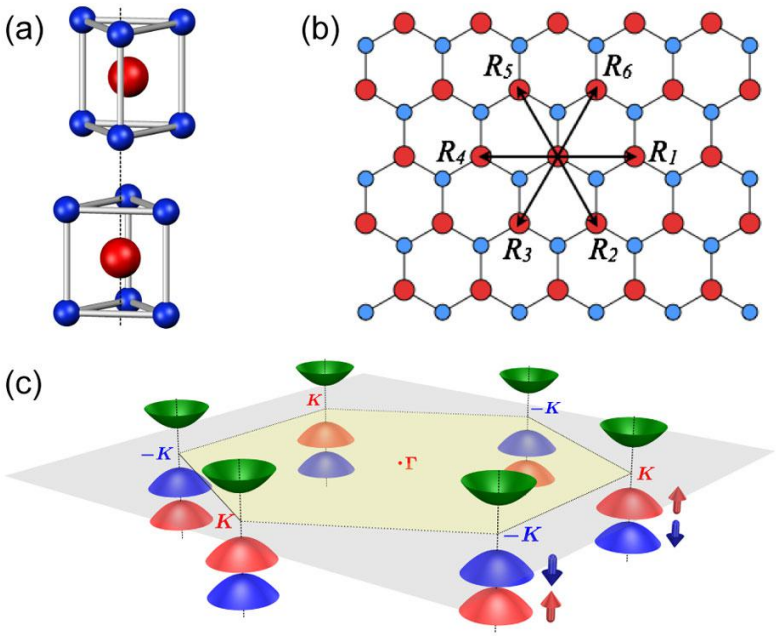

Figure 2.8: *(a) The unit cell of bulk 2H-MoS2, which has the inversion center located in the middle plane. It contains two unit cells of MoS2 monolayers, which lacks an inversion center. (b) Top view of the MoS2 monolayer. Ri are the vectors connecting nearest Mo atoms. (c) Schematic drawing of the band structure at the band edges located at the K points. Adapted from [3].*

As apparent from figures 2.7 and 2.8(c), the conduction and valence-band edges are

located at the corners (K points) of the 2D hexagonal Brillouin zone. Owing to the large valley separation in momentum space, the valley index is expected to be robust against scattering by smooth deformations and long wavelength phonons. Therefore, the two inequivalent valleys represent a suitable binary index for low energy carriers. In contrast to graphene, the group VI-dichalcogenides monolayers show inversion symmetry breaking and a strong SOC typical of heavy metal atoms (especially for WS_2). The former feature leads to two important effects. Firstly, it gives rise to the so-called valley Hall effect where carriers in different valleys flow to opposite transverse edges when an in-plane electric field is applied. Secondly, the symmetry breaking can lead to valley-dependent optical selection rules for interband transitions at the K points. In the following, after describing the symmetries and these two properties, the end of this chapter is devoted to how these two features can be combined with the strong SOC of the group-VI dichalcogenides to enable spin and valley control in 2D materials.

2.3.2 Symmetries and Inversion Symmetry Breaking

As a prerequisite for performing calculations, the symmetries of the crystal structure must be properly described. In its most common bulk form, WS_2 has the 2H stacking order with the space group D_{6h}^4. This means it has a 6-fold rotation axis, 6 two-fold rotation axis and one horizontal mirror plane. Accordingly, its structure is symmetric along 6 vertical mirror planes, each containing the 6-fold axis and one of the two-fold axis. When WS_2 is thinned down to a monolayer, the inversion symmetry is explicitly broken, and the symmetry reduces to D_{3h}^1. The monolayer has a 3-fold rotation axis, 3 two-fold ones, 1 horizontal mirror plane and 3 vertical mirror planes. Moreover, there is an even-odd variation in the structural symmetry of ultrathin films: an even number of layers gives rise to inversion symmetry and the space group D_{6h}^4, while an odd number of layers breaks the inversion symmetry, resulting in the space group D_{3h}^1. The following symmetry analysis provides the necessary basis for understanding the most important physical quantities under transformations.

Monolayer TMDCs

As mentioned before, in monolayer TMDCs the inversion symmetry breaking is broken and this leads to the possibility to distinguish the two valleys. To this end, it is often useful to introduce the magnetic moment expressed as:

$$m_v = \chi * \tau_z \tag{2.1}$$

where $\tau_z = \pm 1$ labels the two valleys and χ is a coefficient characteristic of the material. Under time inversion, the magnetic moment (proportional to a charge movement) changes the sign, and so does the valley label τ_z (because the crystal momentum is inverted and hence also the position of the valley). Under spatial inversion, the valley label

changes sign (for the same as before), but the magnetic moment does not. Overall, the magnetic moment must satisfy the following equations:

$$m_v = \chi * \tau_z = \chi * \tau_{-z} = -\chi * \tau_z = -m_v$$

From this, it in turn follows that

$$m_v = 0$$

in case the crystal structure shows a spatial inversion symmetry.

Breaking of this symmetry is needed to observe the Valley Hall effect, and the valley current is defined as

$$\mathbf{j^v} = \sum_{i=1}^{N} \tau_z^i * \hat{\mathbf{v}}$$

This can be also calculated as

$$\mathbf{j^v} = \sigma_H^v \hat{\mathbf{z}} \times \mathbf{E}$$

where σ_H^v is the transport coefficient (valley Hall conductivity). Under time reversal, the valley current is invariant (speed and valley index change sign) as well as the electric field. Conversely, under spatial inversion, only the latter changes sign (the direction is opposite), which leads to:

$$\hat{P}(\mathbf{j}^v) = \sigma_H^v(-\hat{\mathbf{z}}) \times (-\mathbf{E}) = -\sigma_H^v \hat{\mathbf{z}} \times \mathbf{E} = -\mathbf{j}^v$$

(because of the vector product) with $\hat{P}$ as parity operator. Since the valley current is invariant, it follows:

$$\mathbf{j}^v = -\mathbf{j}^v \Longrightarrow \mathbf{j}^v = 0 \Longrightarrow \sigma_H^v = 0$$

In conclusion, the time reversal symmetry can remain, but if there is no spatial inversion symmetry breaking (like in the graphene), the entire crystal is uniform, the two valleys are equally populated and the overall valley current vanishes.

Multilayer TMDCs and special properties of WS_2

Due to the broken spatial inversion symmetry, the two inequivalent valleys (K and K') obey opposite selection rules. One immediate consequence of this property is the possibility to achieve valley polarization via optical control, which is the first step towards valleytronics. The underlying mechanism will be explained in the following sections.

In TMDC bilayer or other sheets with an even number of layers, the valley-dependent physics is expected to disappear, as has been demonstrated for bilayer MoS_2 [67],[68]. Indeed, even-layer samples are symmetric under spatial inversion (parity transformation) while odd-layer samples are asymmetric. In principle, this would result in complex and layer-number dependent splitting patterns in TMDC multilayers [25].

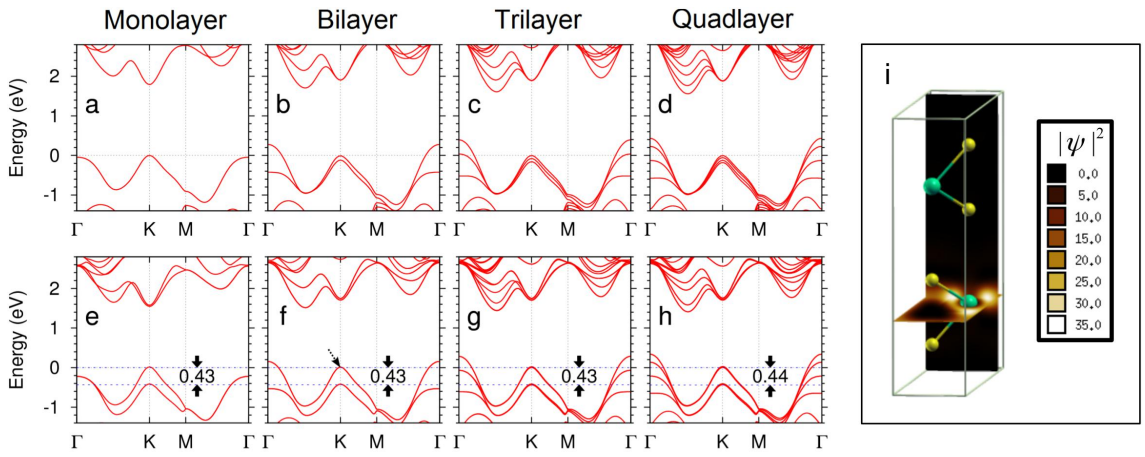

Figure 2.9: *Ab initio calculated band structures for WS2 ultrathin films. (a–d): without spin-orbit coupling; (e–h): with spin-orbit coupling. The valence band splittings at K point are nearly constants, with a value of approximately 0.43 eV for mono-,bi-, tri-, and quad-layers; (i) Electron density map for one valence band Bloch state at the K point in a WS_2 bilayer (indicated by the dashed arrow in (f)). The wavefunction is fully spin-polarized in the down state and almost fully localized in the bottom layer. The other degenerate state at the same K point can be obtained by a spatial inversion plus a time reversal operation. Adapted from [25].*

However, an exception is tungsten disulfide (WS_2), whose anomalously robust valley polarization of the "A" exciton photoluminescence (corresponding to the prominent direct transition peak) was observed for its bilayer form, with a valley polarization close to 90% under near-resonant excitation at 10 K [69].

Later on, it has been documented that similarly high valley polarization (near 80%) can be achieved for multilayer WS_2 with various thicknesses (more than one layer) on near-resonant excitation at 10 K [37]. Even at room temperature, a valley polarization up to 70% could be detected for WS_2 sheets comprising more than three layers. This represents a significant step towards the development of valley-based optoelectronic devices operating at room temperature.

The anomalous behaviour of WS_2 can be explained on the basis of ab initio band structure calculations [25] (see fig. 2.9). The comparison between the band structures in absence (a)-(d) and presence (e)-(h) of SOC reveals that the valence band edges split into two degenerate manifolds with a splitting magnitude independent of the film thickness for both cases . This is in perfect agreement with the strong valley polarization in multilayer WS_2 experimentally observed in ref. [37].

In further detail, in WS_2 monolayers, the Kramer's doublet $|K\uparrow\rangle$ and $|K'\downarrow\rangle$ is separated from the other doublet $|K'\uparrow\rangle$ and $|K\downarrow\rangle$ by the spin-valley coupling energy of $\lambda_{svc} \sim 0.4eV$. In the 2H stacked multilayers, any two neighboring layers are $180^{c}irc$ in-plane rotation of each other. Thus, the states with the same energy in different layers are characterized by the same spin value and an opposite valley index. Therefore, the

spin-valley coupling changes sign from layer to layer and the spin-conserving interlayer hopping can only couple states in neighboring layers with a detuning λ_{svc}. This means that the Bloch states need a sizable energy for interlayer hopping, which is strongly suppressed by the giant spin-valley coupling.

A direct consequence is that the splitting patterns remain as in the monolayer, because the Bloch states in the valence band near the K points are strongly localized on individual layers.

The full suppression of interlayer hopping at the K points by the spin-valley coupling is unique to tungsten dichalcogenides, for which $\lambda_{svc} \sim 0.45eV$ is much greater than the hopping matrix element $t \sim 0.1eV$. For molybdenum dichalcogenides, $\lambda_{svc} \sim t$, such that interlayer hopping is enhanced, thus leading to a dependence of the splitting pattern on the number of layers.

2.3.3 The Hamiltonian without Spin-Orbit Coupling

As previously noted, the inversion symmetry breaking renders the valley Hall effect allowed. This section will describe the phenomenon in more detail. In this context, it is of interest that a single graphene layer with a staggered sublattice potential (expected in epitaxial graphene) has broken inversion symmetry and can be described by a Hamiltonian of a TMDC without SOC. This provides a suitable basis to explain the valley Hall effect (sec. 2.3.4). The effects that arise from SOC will then be described in section 2.5. Starting from a general symmetry consideration, the band structure of TMDCs consists of partially filled metal d-bands lying between metal-chalcogenide $s-p$ bonding and antibonding bands. The trigonal prismatic coordination of the metal M atom splits its d orbitals into three groups: $A_1(d_{z^2}), A_1(d_{xy}, d_{x^2\text{-}y^2})$ and $E'(d_{xz}, d_{yz})$. In the monolayer limit, the reflection symmetry in the $\hat{z}$ direction permits hybridization only between A_1 and E orbitals, which opens a band gap at the K and -K points [26].

In the tight-binding approximation, the TMDCs can be modeled with a nearest-neighbor hopping parameter t and an energy gap Δ [27]. For relatively low doping, most of the carriers (electrons in this case) will gather near the Dirac point, allowing for a low-energy description. It is hence sufficient to focus on the conduction and valence band edges at the $\pm$K valleys, modelled by a massive Dirac fermion Hamiltonian. To first order in k, the C_{3h} symmetry dictates that the two band $k \cdot p$ Hamiltonian has the form

$$H = at(\tau_z k_x \hat{\sigma}_x + k_y \hat{\sigma}_y) + \frac{\Delta}{2}\hat{\sigma}_z \tag{2.2}$$

where $\mathbf{k}$ is measured from the valley center, which is $\mathbf{K_{1,2}} \equiv (\mp 4\pi/3a)\hat{\mathbf{x}}$ with a being the lattice constant. Due to the same symmetry properties, the effective Hamiltonian also describes the graphene with a staggered sublattice potential, where a site energy difference Δ between the sublattices and Pauli matrix $\hat{\sigma}$ is accounting for the A-B sublattice index. For monolayer TMDCs, $\hat{\sigma}$ is the Pauli matrix defined based upon the two

d-orbitals of the metal atom with the magnetic quantum numbers of $m = 0$ and $m = 2\tau_z$, respectively. Without losing generality, one can further consider n-doped-graphene, and a valley magnetic moment of orbital nature only. As noted previously, for TMDCs the spin part needs to be involved, but the strong SOC will not affect this description substantially (sec. 2.5). According to the semiclassical formulation, the equations of motion of Bloch electrons under applied electric and magnetic fields are:

$$\begin{cases} \dot{\mathbf{r}} = \frac{1}{\hbar}\frac{\partial E_n(\mathbf{k})}{\partial \mathbf{k}} - \dot{\mathbf{k}} \times \mathbf{\Omega}_n(\mathbf{k}) \\ \dot{\mathbf{k}} = -e\mathbf{E} - e\dot{\mathbf{r}} \times \mathbf{B} \end{cases} \tag{2.3}$$

where Ω is a pseudovector known as the Berry curvature,

$$\mathbf{\Omega}_n(\mathbf{k}) = i\frac{\hbar^2}{m^2}\sum_{i\neq n}\frac{\mathbf{P}_{n,i}(\mathbf{k}) \times \mathbf{P}_{i,n}(\mathbf{k})}{[E_n^0(\mathbf{k}) - E_i^0(\mathbf{k})]^2} \tag{2.4}$$

with $\mathbf{P}_{n,i}(\mathbf{k}) \equiv \langle u_{n,\mathbf{k}}|\hat{\mathbf{p}}|u_{i,\mathbf{k}}\rangle$ as the interband matrix element of the canonical momentum operator $\hat{\mathbf{p}}$. $\mathbf{E}_n^0(\mathbf{k})$ is the dispersion of the n-th band and $\mathbf{E}_n(\mathbf{k}) = \mathbf{E}_n^0(\mathbf{k}) - \mathbf{m}_n(\mathbf{k}) \cdot \mathbf{B}$ is the electron energy, with the magnetic-field correction. The quantity $\mathbf{m}$ is also a pseudo-vector, specifically the orbital magnetic moment:

$$\mathbf{m}_n(\mathbf{k}) = -i\frac{e\hbar}{2m^2}\sum_{i\neq n}\frac{\mathbf{P}_{n,i}(\mathbf{k}) \times \mathbf{P}_{i,n}(\mathbf{k})}{E_n^0(\mathbf{k}) - E_i^0(\mathbf{k})} \tag{2.5}$$

For a 2D system, the orbital magnetic moment is always normal to the plane, written as $m(\mathbf{k})\hat{z}$.

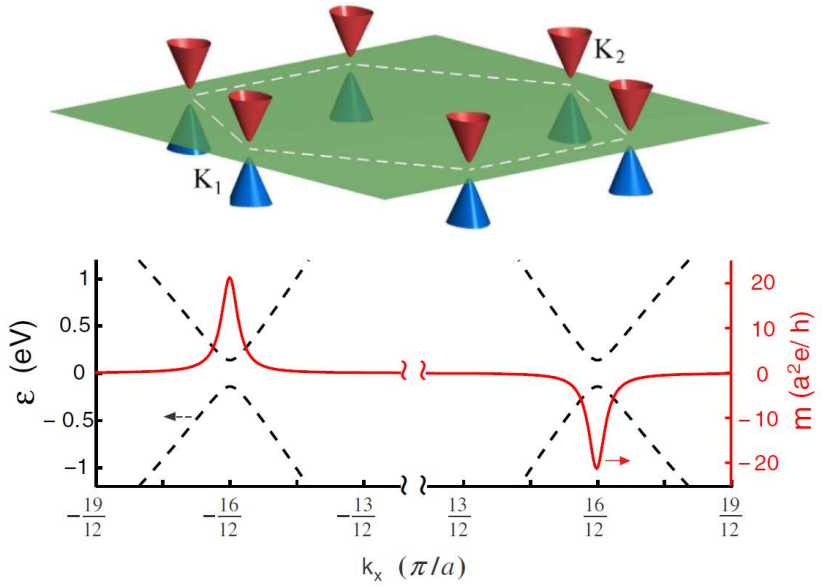

Figure 2.10: *Energy bands (top panel) and orbital magnetic moment of the conduction bands (bottom panel) of a graphene sheet with broken inversion symmetry. The Berry curvature* $\Omega(\mathbf{k})$ *has a distribution similar to that of* $m(\mathbf{k})$*. The first Brillouin zone is outlined by the dashed lines, and two inequivalent valleys are labelled as* K_1 *and* K_2*. The top panel shows the conduction and valence bands in the energy range from -1 to 1 eV. The parameters used are* $t = 2.82$ *eV and* $\Delta = 0.28$ *eV. Adapted from [22] .*

The analytic expressions for the magnetic moment and Berry curvature can be obtained from the Hamiltonian (eq. 2.2) with the tight-binding Bloch states, and taking into account that the magnetic moment is concentrated in the valleys with opposite signs in the two inequivalent ones (see fig.2.10):

$$\mathbf{m}(\mathbf{k}) = -\hat{\mathbf{z}}\frac{2a^2t^2\Delta}{4a^2t^2k^2 + \Delta^2}\frac{e}{2\hbar}\tau_z \tag{2.6}$$

The magnetic moment has identical but opposite values in the conduction and valence bands, while at the Dirac points ($k = 0$) it assumes a simple and suggestive form: $\mathbf{m} = -\hat{\mathbf{z}}\tau_z\mu_B^*$, where $\mu_B* \equiv e\hbar/2m*$ represents the spin Bohr magneton, with the electron effective mass at the band edge. This equation confirms the initial assumption in section 2.3.2,which was made to demonstrate the need for spatial inversion symmetry breaking. On this basis, it is reasonable to call the orbital moment calculated above as the intrinsic magnetic moment associated with the valley degree of freedom and pseudospin. Within this framework, the Berry curvature in the conduction band is given by:

$$\mathbf{\Omega}_c(\mathbf{k}) = -\hat{\mathbf{z}}\frac{2a^2t^2\Delta}{(4a^2t^2k^2 + \Delta^2)^{3/2}}\tau_z \tag{2.7}$$

In the valence band, it has the same magnitude, but opposite sign. In the next subsection, this characteristic will be exploited to describe the Valley Hall effect.

2.3.4 The Valley Hall effect

The valley-dependent magnetic moment **m** enables coupling of the valley pseudospin to a magnetic field, and in turn the detection of valley polarization as a magnetic signal.

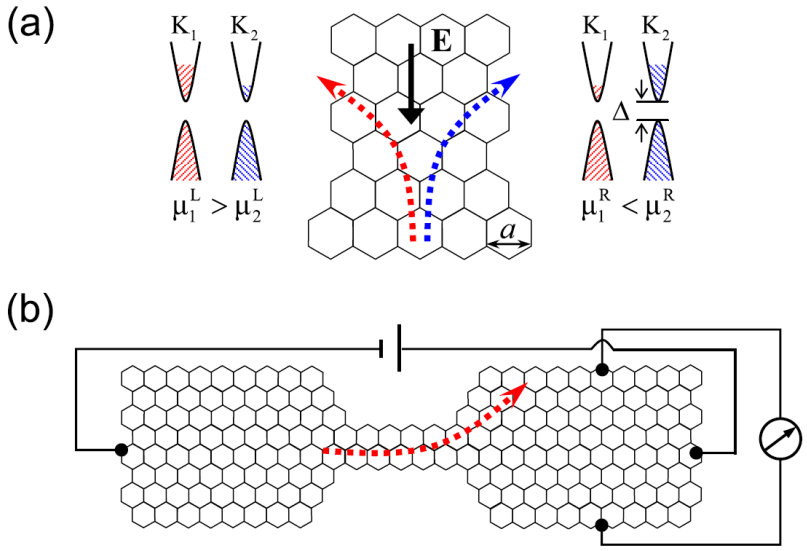

Figure 2.11: *Electric generation (a) and detection (b) of the valley polarization. (a) An in-plane electric field will generate a transverse valley current, which leads to a net valley polarization on the sample edges. (b) A valley polarization results in a transverse voltage across the sample. Adapted from [22].*

In particular, while spin polarization of electrons can be created by a magnetic field (Pauli paramagnetism), the analogous valley polarization in TMDCs is due to coupling between a magnetic field along the $\hat{z}$ direction and the valley magnetic moment. It should be noted that, for typical values of $\Delta \sim 0.28eV$ and $t \sim 2.82eV$ with a lattice constant a $= 2.46$ $\mathring{A}$, μ_B^* is found to be about 30 times the Bohr magneton. Therefore, the response to a perpendicular magnetic field is dominated by the valley magnetic moment, especially at low doping. Interestingly, unlike the spin moment, which will respond to magnetic fields in any direction, the valley magnetic moment only couples to magnetic fields in the z-direction. Conversely, a population difference in the two valleys may be detected as a signal of orbital magnetization. The orbital magnetization consists of the orbital moments of the carriers plus a correction from the Berry curvature

$$M = 2\int \frac{d^2k}{(2\pi)^2}[m(\mathbf{k}) + (e/\hbar)[\mu - \epsilon(\mathbf{k})]\Omega(\mathbf{k})] \tag{2.8}$$

where μ is the local chemical potential, and the integration is over states below the chemical potential.

On the basis of a two-band model with particle-hole symmetry, the simple relation $m(\mathbf{k}) = (e/\hbar)\epsilon(\mathbf{k})\Omega(\mathbf{k})$ can be used. Therefore substituting this in the integral and

assuming a population difference, characterized by different chemical potentials in the two valleys $\mu_1 \neq \mu_2$, the net orbital magnetization becomes:

$$\delta M = 2\frac{e}{h}[\mu_1 C_1(\mu_1) + \mu_2 C_2(\mu_2)] \approx 2\frac{e}{h} C_1(\bar{\mu})\delta\mu \tag{2.9}$$

where $2\pi C_i(\mu_i) = \int^{\mu_i} d^2k\Omega(\mathbf{k})$ is the Berry phase around the Fermi circle in valley K_i, $\delta\mu \equiv \mu_1 - \mu_2$ and $\bar{\mu}$ is the average chemical potential between μ_1 and μ_2.

It has been established that in the presence of an in-plane electric field, an electron will acquire an anomalous velocity perpendicular to the field and proportional to the Berry curvature[13], giving rise to an intrinsic contribution to the Hall conductivity [31] [32]:

$$\sigma_H^{int} = 2(e^2/\hbar)\int \frac{d^2k}{(2\pi)^2} f(\mathbf{k})\Omega(\mathbf{k}) \tag{2.10}$$

where $f(\mathbf{k})$ is the Fermi-Dirac distribution function. This illustrates the importance of symmetry breaking for the properties of the Berry curvature $\Omega(\mathbf{k})$, i.e. that the function changes sign under time reversal and parity transformation. Correspondingly, if the symmetry is preserved, the integral and the conductivity vanish, and hence the two valleys are equally populated and there is no net orbital magnetization. Moreover, using the relation for the Berry curvature (eq. 2.4) and ignoring intervalley scattering, the valley-dependent Hall conductivity can be approximated to [22]

$$\sigma_H(\tau_z) = \tau_z \frac{e^2}{h}\left[1 - \frac{\Delta}{2\mu} - \frac{3\Delta t^2 q_F^2 a^2}{8\mu^3}\right] \tag{2.11}$$

where q_F is the Fermi wave vector defined by $\mu = \frac{1}{2}\sqrt{\Delta^2 + 3q_F^2 a^2 t^2}$ This valley dependence will lead to an accumulation of electrons on opposite sides of the sample according to the opposite valley indices (see 2.11). Upon application of an electric field E_y, a valley population difference will be generated:

$$\delta n = j_x^v \tau_v = \sigma_H^v E_y \tau_v \tag{2.12}$$

with τ_v as the intervalley life-time, and the difference in valley dependent Hall conductivity given by

$$\sigma_H^v = \sum_{valleys} \tau_z \sigma_H(\tau_z) \tag{2.13}$$

This valley polarization distributed along the edge may be detected as a magnetic signal, as already discussed in connection with eq.2.9, or as a Hall current:

$$j_x = \frac{e^2}{h}\left[\frac{\Delta}{2\bar{\mu}^2} - \frac{9\Delta t^2 \bar{q}_F^2 a^2}{8\bar{\mu}^4}\right]\delta\mu E_y \tag{2.14}$$

This accumulation of electrons at opposite sides will lead to a measurable transverse voltage across the sample.

In conclusion, the inversion symmetry breaking leads to a net orbital magnetization and a transverse valley Hall current, which creates a net valley polarization at the sample edges.

2.4 Optoelectronic Properties of TMDCs

The inversion symmetry breaking of TMDCs monolayers imparts additional, remarkable optoelectronic properties. Specifically, the symmetry breaking allows for valley-contrasting circular dichroism for interband transitions in different regions of the Brillouin zone. Recalling the magnetic moment relation (eq. 2.5), it can be seen that in the upper and lower bands (switching i with c), $\mathbf{m}(\mathbf{k})$ remains unchanged (the sign changes in both, the numerator and denominator). Its projection along the light propagation direction $\hat{\mathbf{z}}$ can be expressed as

$$-2\frac{\mathbf{m}(\mathbf{k})\cdot\hat{\mathbf{z}}}{\mu_B} = \frac{|P_+(\mathbf{k})|^2 - |P_-(\mathbf{k})|^2}{m_e[\epsilon_c(\mathbf{k}) - \epsilon_v(\mathbf{k})]} \tag{2.15}$$

where the numerator is the difference in k-resolved oscillator strength of σ_+ and σ_- circular polarizations, $P_\pm \equiv P_x^{c,v} \pm iP_y^{c,v}$. The comparison between the oscillator strength of the polarization averaged over energies and the sum of the momenta from the conducting band

$$\frac{|P_+(\mathbf{k})|^2 + |P_-(\mathbf{k})|^2}{2m_e[\epsilon_c(\mathbf{k}) - \epsilon_v(\mathbf{k})]} = m_e Tr\left[\frac{1}{2\hbar^2}\frac{\partial^2\epsilon_c(\mathbf{k})}{\partial k_\alpha \partial k_\beta}\right] \tag{2.16}$$

illustrates the connection between the orbital magnetic moment and the degree of circular polarization. In fact, the latter is defined as:

$$\eta(\mathbf{k}) = \frac{|P_+(\mathbf{k})|^2 - |P_-(\mathbf{k})|^2}{|P_+(\mathbf{k})|^2 + |P_-(\mathbf{k})|^2} \tag{2.17}$$

By including the effective mass:

$$\left[\frac{1}{m*}\right]_{\alpha\beta} = \left[\frac{1}{\hbar^2}\frac{\partial^2\epsilon_c(\mathbf{k})}{\partial k_\alpha \partial k_\beta}\right] \tag{2.18}$$

the expression for $\eta(\mathbf{k})$ can be obtained by dividing eq. 2.15 through eq.2.16:

$$\eta(\mathbf{k}) = -\frac{\mathbf{m}(\mathbf{k})\cdot\hat{\mathbf{z}}}{\mu_B^*(\mathbf{k})} \tag{2.19}$$

with $\mu_B^*(\mathbf{k})$ as the *effective* Bohr magneton (where m is substituted by the effective mass). It follows that in the presence of time reversal symmetry, two Bloch states with opposite crystal momentum have opposite orbital moment too, and hence, the overall

circular dichroism vanishes. Comparison between the previous definition of the Berry curvature

$$\mathbf{\Omega}_n(\mathbf{k}) = i\frac{\hbar^2}{m^2}\sum_{i\neq n}\frac{\mathbf{P}_{n,i}(\mathbf{k})\times\mathbf{P}_{i,n}(\mathbf{k})}{[E_n^0(\mathbf{k})-E_i^0(\mathbf{k})]^2} \tag{2.20}$$

and the one for magnetic moment (see eq.2.5), yields the relation between these physical quantities as:

$$\eta(\mathbf{k}) = -\frac{\mathbf{m}(\mathbf{k})\cdot\hat{\mathbf{z}}}{\mu_B^*(\mathbf{k})} = -\frac{\mathbf{\Omega}(\mathbf{k})\cdot\hat{\mathbf{z}}}{\mu_B^*(\mathbf{k})}[\epsilon_c(\mathbf{k})-\epsilon_i(\mathbf{k})]\frac{e}{2\hbar} \tag{2.21}$$

where the index i, $\mathbf{m}(\mathbf{k})$ and $\mathbf{\Omega}(\mathbf{k})$ indicates their value in the upper band.

In conclusion, this relation represents a connection between k-resolved valley contrasted optical circular dichroism, the valley Hall conductivity (proportional to $\mathbf{\Omega}(\mathbf{k})$) and the orbital magnetization (proportional to the valley magnetic moment).

2.5 Coupled Spin and Valley Physics

Compared to graphene, TMDCs comprise heavier atoms and accordingly much stronger SOC, which leads to coupled spin and valley physics and the possibility to control them by external means. Approximating the SOC by the intra-atomic contribution $\mathbf{L}\cdot\mathbf{S}$, the total Hamiltonian is given by:

$$H = at(\tau_z k_x\hat{\sigma}_x + k_y\hat{\sigma}_y) + \frac{\Delta}{2}\hat{\sigma}_z - \lambda\tau_z\frac{\hat{\sigma}_z-1}{2}\hat{s}_z \tag{2.22}$$

where $\hat{s_z}$ is the Pauli matrix for spin and 2λ is the spin splitting at the valence band top. It is noteworthy that the latter arises exclusively from the inversion symmetry breaking and SOC in the material. Moreover, the time reversal symmetry requires that the valence-band spin splitting at different valleys in K points must be opposite. This new contribution to the Hamiltonian makes the band structure change, especially in the neighbourhood of the K points, as apparent from fig.2.9. The spin splitting in the different valleys is depicted in fig.2.8(c).

The valley Hall and spin Hall effects are driven by the Berry phase associated with the Bloch electrons. As has been established above, in the presence of an in-plane electric field an electron will acquire an anomalous velocity proportional to the Berry curvature in the transverse direction. This is the already described valley Hall effect, wherein the electrons move according to their valley index, which gives rise to the intrinsic contribution (compare eq. 2.10):

$$\sigma_H^{int} = 2(e^2/\hbar)\int\frac{d^2k}{(2\pi)^2}f(\mathbf{k})\Omega(\mathbf{k}) \tag{2.23}$$

For massive Dirac fermions described by the previous Hamiltonian, the Berry curvature is:

$$\mathbf{\Omega}_c(\mathbf{k}) = -\hat{\mathbf{z}}\frac{2a^2t^2\Delta'}{(4a^2t^2k^2+\Delta'^2)^{3/2}}\tau_z \tag{2.24}$$

Note that the Berry curvature is similar to eq.2.7 for the Hamiltonian without SOC, but this is dependent on spin via the band gap $\Delta' \equiv \Delta - \tau s_z \lambda$, which acquires a contribution from SOC coupling. The Berry curvature for the valence band is $\mathbf{\Omega}_v(\mathbf{k}) = -\mathbf{\Omega}_c(\mathbf{k})$.

The valley Hall conductivity is then obtained as:

$$\sigma_v^n = 2(e^2/\hbar)\int d\mathbf{k}[f_{n,\uparrow}(\mathbf{k})\Omega_{n,\uparrow}(\mathbf{k}) + f_{n,\downarrow}(\mathbf{k})\Omega_{n,\downarrow}(\mathbf{k}) \tag{2.25}$$

where n denotes the carriers (electrons or holes).

The spin Hall conductivity is given by:

$$\sigma_s^n = 2(e/2)\int d\mathbf{k}[f_{n,\uparrow}(\mathbf{k})\Omega_{n,\uparrow}(\mathbf{k}) - f_{n,\downarrow}(\mathbf{k})\Omega_{n,\downarrow}(\mathbf{k}) \tag{2.26}$$

Both these integrations are performed over the neighborhood of one K point, where the curvature is nearly constant, since $\Delta >> atk$ (for typical values see table 2.2). Furthermore, assuming a moderate hole doping, with the Fermi energy lying between the two split valence-band tops, which means $f_{n,\downarrow} \simeq 0$ because it is a band over the Fermi energy. On this basis, the valley and spin Hall conductivities of holes can be approximated to:

$$\sigma_s^{holes} = \sigma_v^{holes} = \frac{1}{\pi}\frac{\mu}{\Delta - \lambda} \tag{2.27}$$

for $\mu << \Delta - \lambda$, where μ is the Fermi energy measured from the valence-band maximum, and the latter term being the difference between the band gap and the spin splitting energy, the integral can be calculated to the first order in $\frac{\mu}{\Delta-\lambda}$.

If the system is electron doped, one must consider both conduction bands, which are degenerate at the K points as can be seen from the band structures shown in fig.2.9 and

Table 2.2: *Fitting result from first-principles band structure calculations. In each case, the monolayer is relaxed. The spin splitting values 2λ at valence-band edge were previously reported in the first principle studies. The Berry curvature values $\Omega_1(\Omega_2)$ are evaluated at -K point for the spin-up (-down) conduction band. Adapted from [3]*

Material	a ($\mathring{A}$)	Δ(eV)	t(eV)	2λ(eV)	$\Omega_1(\mathring{A}^2)$	$\Omega_2(\mathring{A}^2)$
MoS2	3.193	1.66	1.10	0.15	9.88	8.26
WS2	3.197	1.79	1.37	0.43	15.51	9.57
MoSe2	3.313	1.476	0.94	0.18	10.23	7.96
WSe2	3.310	1.60	1.19	0.46	16.81	9.39

in fig.2.12. Since they display a small spin-splitting quadratic in k, the conductivities are:

$$\begin{aligned} \sigma_s^{electrons} &= \frac{1}{\pi}\frac{\Delta}{\Delta^2-\lambda^2}\mu \\ \sigma_v^{electrons} &= \frac{1}{\pi}\frac{\lambda}{\Delta^2-\lambda^2}\mu \end{aligned} \tag{2.28}$$

and their ratio is $\frac{\lambda}{\Delta}$.

Flipping of the valley index requires atomic scale scatters, since the two valleys are separated by a wave vector comparable to the size of Brillouin zone. Similarly, spin flips require the coupling with magnetic defects, since s_z is a good quantum number at the conduction and valence band edges. Therefore, as can be concluded from fig.2.12(b) where the dashed line represents the Fermi energy, in the valence band simultaneous flipping of valley and spin under energy conservation requires atomic scale magnetic scatters. In the absence of such scatterers, the holes are expected to have long spin and valley lifetimes.

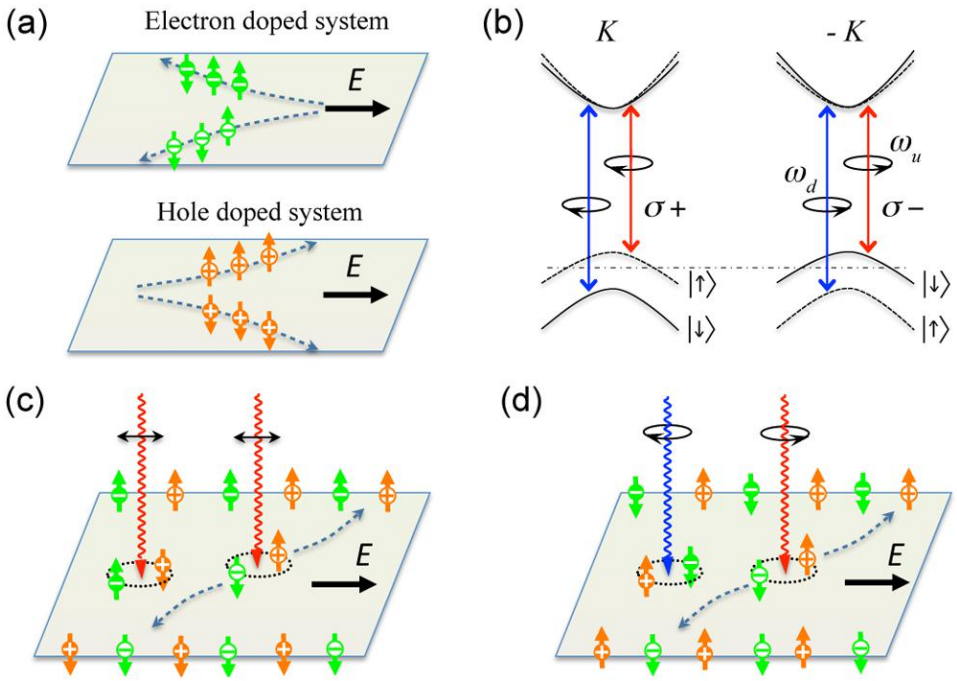

Figure 2.12: *Coupled spin and valley physics in monolayer group-VI dichalcogenides. The electrons and holes in the valley K are denoted by white "-", "+" symbols in dark circles and their counterparts in the valley -K are denoted by inverse color. (a) Valley and spin Hall effects in electron and hole-doped systems. (b) Valley and spin optical transition selection rules. Solid (dashed) curves denote bands with spin-down (-up) quantized along the out-of-plane direction. The splitting in the conduction band is exaggerated. ω_u and ω_d are, respectively, the transition frequencies from the two split valence-band tops to the conduction band bottom. (c) Spin and valley Hall effects of electrons and holes excited by a linearly polarized optical field with frequency ω_u. (d) Spin and valley Hall effects of electrons and holes excited by two-color optical fields with frequencies ω_u and ω_d and opposite circular polarizations. Adapted from [3] .*

2.5.1 Optical Interband Transitions

After the above theoretical discussion, it is useful to analyse the possible optical transitions in more details. In TMDCs, different valley and spin Hall currents can be generated, depending on the frequency and polarization of the incident light. Circular polarized light can selectively excite carriers with various combination of valley and spin index, as detailed in the following.

The coupling strength with the optical field of $\sigma_\pm$ circular polarization is given by

$$P_\pm(\mathbf{k}) \equiv P_x(\mathbf{k}) \pm P_y(\mathbf{k}) \tag{2.29}$$

where

$$P_\alpha(\mathbf{k}) \equiv m_0 \langle u_c(\mathbf{k})| \frac{1}{\hbar} \frac{\partial \hat{H}}{\partial k_\alpha} |u_v(\mathbf{k})\rangle \tag{2.30}$$

is the interband matrix element of the canonical momentum operator. For transitions near the K points:

$$|P_{\pm}(\mathbf{k})|^2 = \frac{m_0^2 a^2 t^2}{\hbar^2}\left(1 \pm \tau \frac{\Delta'}{\sqrt{\Delta'^2 + 4a^2t^2k^2}}\right)^2 \tag{2.31}$$

Since $\Delta' \gg atk$, the second term assumes a value close to 1, such that:

$$|P_{+}(\mathbf{k})|^2 \simeq \frac{m_0^2 a^2 t^2}{\hbar^2}(1 + 1 * 1)^2 \qquad \text{for } \tau = +1\text{, in K valley} \tag{2.32}$$

$$|P_{+}(\mathbf{k})|^2 \simeq \frac{m_0^2 a^2 t^2}{\hbar^2}(1 - 1 * 1)^2 = 0 \qquad \text{for } \tau = -1\text{, in -K valley} \tag{2.33}$$

$$|P_{-}(\mathbf{k})|^2 \simeq \frac{m_0^2 a^2 t^2}{\hbar^2}(1 - (-1) * (-1))^2 = 0 \qquad \text{for } \tau = +1\text{, in K valley} \tag{2.34}$$

$$|P_{-}(\mathbf{k})|^2 \simeq \frac{m_0^2 a^2 t^2}{\hbar^2}(1 + (-1) * (-1))^2 \qquad \text{for } \tau = -1\text{, in -K valley} \tag{2.35}$$

Therefore $\sigma_+(\sigma_-)$ may selectively excite carriers in K (-K) valleys.

It should be emphasized that the spin is always conserved in the optical transitions since the field couples only to the orbital part of the wave function. On the other hand, the valley-contrasting spin splitting of the valence-band tops couples the valley to the spin, such that the valley optical selection rule becomes spin-dependent. As mentioned before, depending on the frequency and polarization, the light can generate couples of electron and holes with different properties specified by:

circular polarization	frequency		electron spin	hole spin	valley
σ_+	ω_u	$\longrightarrow$	$\uparrow$	$\downarrow$	K
σ_+	ω_d	$\longrightarrow$	$\downarrow$	$\uparrow$	K
σ_-	ω_u	$\longrightarrow$	$\uparrow$	$\downarrow$	-K
σ_-	ω_d	$\longrightarrow$	$\downarrow$	$\uparrow$	-K

These spin- and valley-dependent selection rules allow to generate long-lived spin and valley accumulations at the sample boundaries in a Hall bar geometry. In such configuration, a longitudinal charge current can be applied to separate the electrons from the holes. Owing to the Berry curvature in the conduction and valence band, the electrons and holes will also acquire opposite transverse velocities, and hence move to the two opposite boundaries of the sample.

In case of σ_+ circularly polarized light with a frequency ω_u, for example, one spin-up electron and one spin-down hole are generated in the respective K valleys. These carriers move to the sample boundaries, with the electron assuming spin-up and the hole

assuming spin-down orientation. Assuming Ω_1 as the Berry curvature in the valence band with spin-down orientation in the valley K, and considering eq.2.26 with only the excited electron contributing to the distribution function, the electron spin Hall conductivity will be $\frac{e}{2}\Omega_1$.

Taking into the account the valley index, which makes the Berry curvature changing sign, along with eqs. 2.26 and 2.25, and that $\Omega_c = -\Omega_v$, the remaining cases can be calculated as summarized in table 2.3. It is noteworthy that in the same valley, the Berry curvature depends on spin through the gap $\Delta' = \Delta - \tau s_z \lambda$, such that there will be a different Berry curvature Ω_2 for a different spin. In the valley K', the values of the Berry curvature are inverted with respect to those in the K valley because $\Delta'' = \Delta - (-\tau)s_z\lambda$.

Table 2.3: *Photoinduced spin, valley, and charge Hall effects. The table lists the values of the electron and hole conductivity for different frequencies and polarization of the incident light.* $\sigma_s^{e(h)}$ *and* $\sigma_v^{e(h)}$ *denote the spin and valley Hall conductivity, respectively.* σ *is the total charge Hall conductivity from both carriers. All conductivities are normalized by the photoexcited carrier density of electrons or holes, and only intrinsic contribution are considered. Adapted from [3].*

Light frequency	Polarization	σ_s^e	σ_s^h	σ_v^e	σ_v^h	σ
ω_{up}	X or Y	$\frac{e}{2}\Omega_1$	$\frac{e}{2}\Omega_1$	$\frac{e}{\hbar}\Omega_1$	$\frac{e}{\hbar}\Omega_1$	0
ω_{down}	X or Y	$-\frac{e}{2}\Omega_2$	$-\frac{e}{2}\Omega_2$	$\frac{e}{\hbar}\Omega_2$	$\frac{e}{\hbar}\Omega_2$	0
ω_{up}	σ_+	$\frac{e}{2}\Omega_1$	$\frac{e}{2}\Omega_1$	$\frac{e}{\hbar}\Omega_1$	$\frac{e}{\hbar}\Omega_1$	$2\frac{e^2}{\hbar}\Omega_1$
ω_{down}	σ_-	$-\frac{e}{2}\Omega_2$	$-\frac{e}{2}\Omega_2$	$\frac{e}{\hbar}\Omega_2$	$\frac{e}{\hbar}\Omega_2$	$-2\frac{e^2}{\hbar}\Omega_2$

2.6 Progress in Optical Control of Valley Pseudospin

In the previous section, most relevant aspects of the electronic and optical properties of TMDCs were discussed. In this section, the experimental state-of-the-art in the control of spin and valley pseudospin will be described. Recently, experimental breakthroughs in the manipulation of valley pseudospin have been achieved for monolayer TMDCs with a direct band gap at the ±K points in the visible wavelength range.

Photoluminescence (PL) measurements provided the first experimental evidence for the transition to the direct bandgap at the monolayer limit, and the PL intensity was found to be up to two (four) orders of magnitude larger compared to the case of bilayers (bulk crystal). The elementary excitation that plays a key role in optoelectronic phenomena is the exciton, a bound electron and hole pair. In doped semiconductors, an extra electron may bind to the neutral exciton to form a charged exciton (trion).

Trions are particularly interesting, because their binding energy have been detected by photoluminescence measurements.Based upon the known ratio between the trion and exciton binding energy, the latter was determined to be at least a few hundreds meV [28]. Such strong Coulomb interactions are a consequence of the lowered dimensionality,

which leads to reduced dielectric screening in an atomically thin material, and also of the relatively large electron and hole effective masses in these materials.

The robust excitons and trions can produce a strongly polarized photoluminescence with the same circular polarization as the incident light. The Hanle effect can be used to distinguish whether the polarized photoluminescence is due to polarization of the valley or spin. To this end, a transverse magnetic field is applied to cause the spin to precess and thereby to suppress the corresponding photoluminescence polarization. The valley pseudospin, by contrast, does not couple to the transverse magnetic field. In practice, persistent photoluminescence polarization has been observed, confirming valley polarization as the origin of the polarized light [41]

A linearly polarized photon, a coherent superposition of left and right circularly polarized photon, can be photoemitted in monolayer WSe_2, with a polarization angle that always coincides with the linearly polarized excitation[42]. This observation directly evidences that the valley polarization of the photo-excited electrons and holes is largely conserved during hot-carrier relaxation, exciton formation, and radiative recombination processes. This again underscores that intervalley scattering is suppressed by the large momentum separation between valleys.

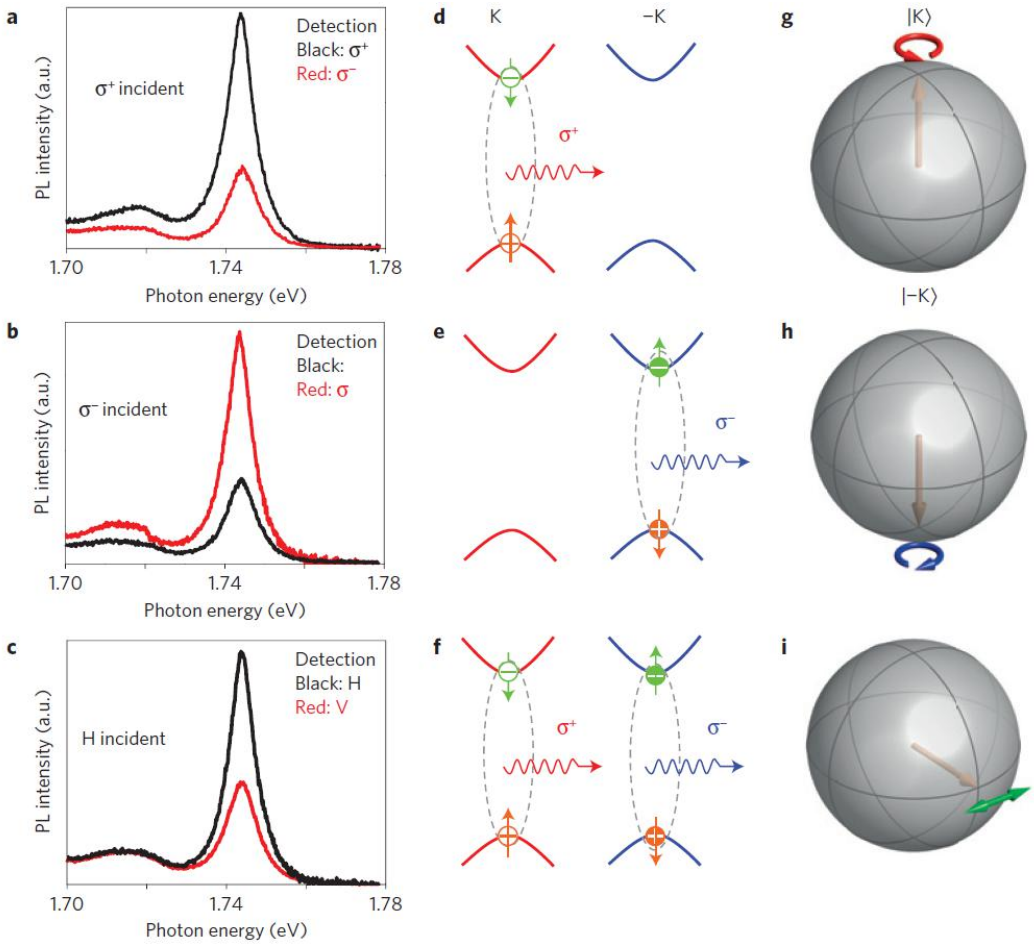

Figure 2.13: *Effects of valley polarization and valley coherence on the photoluminescence of a WSe_2 monolayer. a–c: Polarization-resolved photoluminescence of neutral excitons (X^0) induced by right (σ^+) (a), left (σ^-) (b) and linearly polarized (c) excitation. d–f: Energy level diagrams of the polarized emissions in a to c, respectively. The vertical arrows indicate the spin of the electrons and holes. g–i: Bloch vector representations of optical control of valley pseudospin corresponding to a–c, respectively. Arrows outside and inside the Bloch sphere correspond to the light polarization and valley pseudospin vectors, respectively. As shown in (g), the top (bottom) of the sphere corresponds to valley K(-K) and σ^+(σ^-) circularly polarized photons. Adapted from [11].*

2.7 Heterostructures

As already mentioned, monolayer TMDCs with a broken inversion symmetry possess two inequivalent valleys, a property that offers unique opportunities for valley control and to excite carriers selectively within a particular valley with a specific valley pseudospin using circularly polarized light. The two valleys are degenerate due to the time-reversal symmetry. Lifting the valley degeneracy is of great interest because, with the two valleys

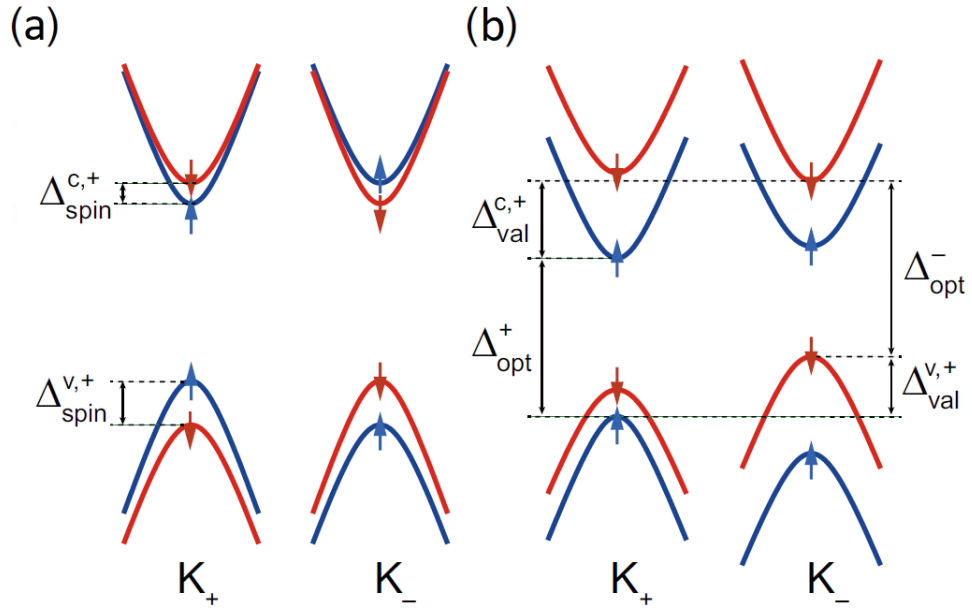

Figure 2.14: *Schematic band structure at two valleys of monolayer MX_2 without (a) and with (b) a Zeeman field. The electronic states with up/down spins are represented by blue/red lines with arrows ↑ / ↓. Adapted from [39].*

having different energies, they are also differently populated and this would allow the control of valley polarization for memory and logic applications. Such control has been experimentally demonstrated by applying an external magnetic field to induce Zeeman splitting of the bands in different valleys [38]. As shown in fig.2.14, this leads to an energetic rise of the spin-down states, well above the spin up states. In the experiment, only a moderate valley splitting of ∼0.2 meV/T was observed [38].

In order to realize stronger valley spitting in monolayer TMDCs, the interfacial magnetic exchange field (MEF) induced by a ferromagnetic substrate can be exploited. This is exemplified in fig.2.15for MoT2 on the ferromagnetic insulator EuO. Magnetoreflectance measurements on this type of heterostructure revealed a remarkable valley splitting of 2.5 meV at an external B-field of 1 T, corresponding to an effective exchange field of $\sim 12T$ [36]. Theory predicts that the exchange coupling between the ferromagnetic EuO (12 Eu/O atomic layers) and $MoTe_2$ may result in a valley splitting of 44 meV [39]. The MEF of a magnetic insulator can induce magnetic order and valley and spin polarization in TMDCs, which may enable valleytronic and quantum-computing applications.

Another suitable ferromagnetic insulator is EuS, due to the large magnetic moment of Eu^{2+} ($S_z \simeq 7\mu_B$) and the large exchange coupling ($J \simeq 10$ meV), leading to a large MEF ($\alpha J S_z$).

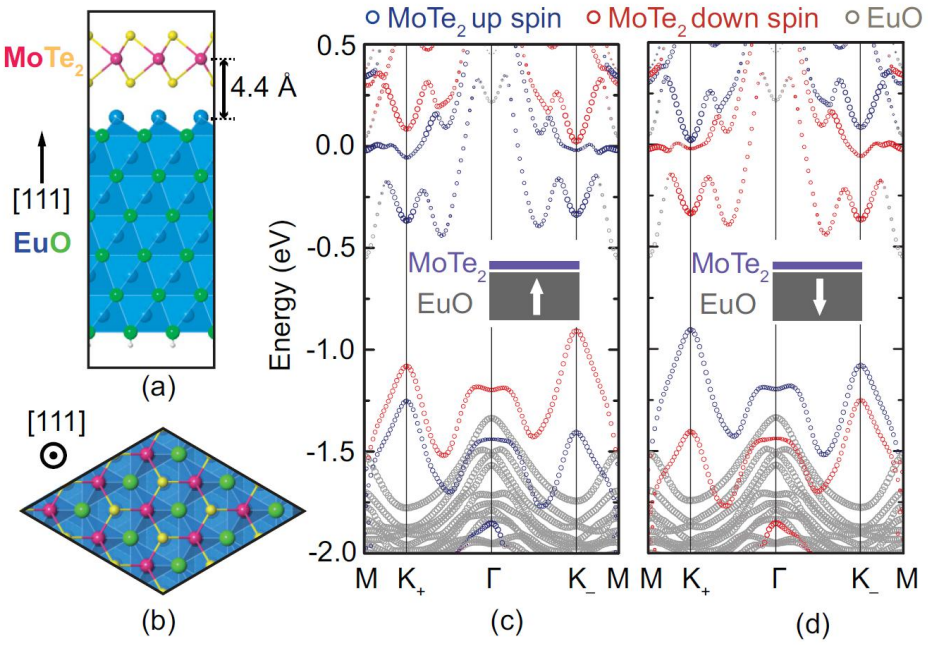

Figure 2.15: *(a) Side view and (b) top view of a $MoTe_2/EuO$ heterostructure. (c), (d) Calculated band structures with EuO magnetized upward and downward, respectively. A fat-band representation is used to indicate the projected weights on $MoTe_2$ (blue and red) and EuO (gray). For the $MoTe_2$ projections, blue/red states stand for up/down spin ones, respectively. The energy scale is zeroed to the Fermi level. Adapted from [39].*

Fig.2.16(c)the magnetoreflectance of a WSe2 monolayer on a Si/SiO2 substrate with that on a EuS substrate. In the case of the Si/SiO2 substrate (fig. 2.16c), at zero B-field the spectra recorded with opposite light helicity match perfectly, indicating the absence of an energy splitting of the two valleys, as required by the time-reversal symmetry. In contrast, upon application of B = 7 T perpendicular to the substrate plane, a modest valley splitting emerges (fig. 2.16(c), top).

The σ_+ spectrum (A-exciton transition at the K valley) shifts to a lower energy, whereas the σ_- spectrum shifts to a higher energy. The valley splitting is defined as $\Delta E \equiv E(\sigma_-) - E(\sigma_+)$, where E($\sigma_+$) and E($\sigma_-$) refer to the fitted peak energy of σ_+ and σ_-, respectively. When an opposite B-field of -7 T is applied, the sign of the valley splitting is reversed, as shown in the lower plot of fig.2.16(c), and ΔE is determined to be 1.5 meV at this magnetic field strength. For WSe_2 on EuS (fig. 2.16d), the valley splitting is equal to 3.9 meV at 7 T (fig.2.16(d)). at zero B-field no excitonic splitting can be observed. Under an applied B-field of 7 T, a valley splitting of 3.9 meV is detected. This enhanced value compared to the case of the Si/SiO_2 substrate demonstrates that in addition to the Zeeman effect, there is also a sizeable contribution from the ferromagnetic EuS substrate. Other interesting ferromagnetic substrates may

also be employed like $RuCl_3$.

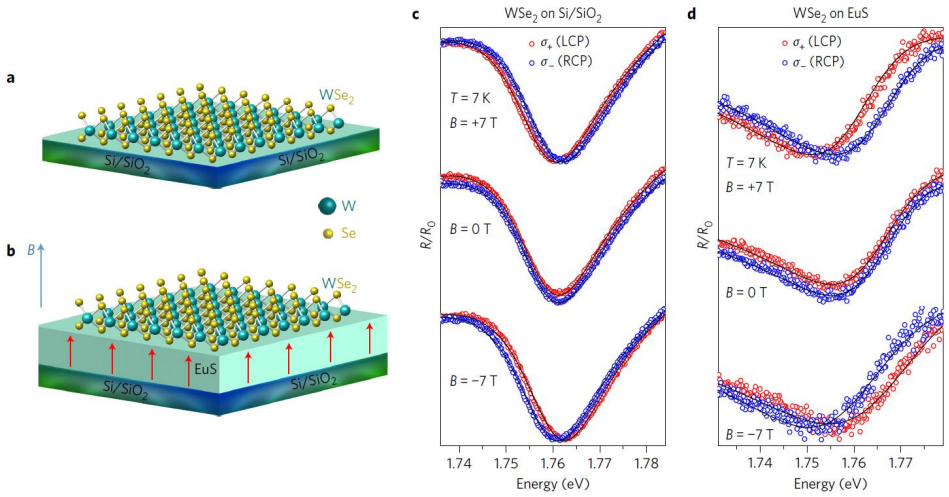

Figure 2.16: *Schematic depiction of a WSe2 monolayer on Si/SiO_2 substrates (a) and on a ferromagnetic EuS substrate (b). A magnetic field is applied perpendicular to the plane. (c,d) Reflectance spectra showing the A exciton of monolayer WSe_2 recorded at T=7 K, for the Si/SiO_2 substrate (c) and the EuS substrate (d). Top, B=+7 T; middle, B = 0; bottom, B = -7 T. σ_+ (σ_-) corresponds to the transition at the K (K') valley. There is no splitting for spectra at B = 0, for either the Si/SiO_2 or the EuS substrate. At +7 T, the σ_+ (σ_-) component shifts to lower (higher) energy. At -7 T, the energy shift is in the opposite direction. By comparing (c) and (d), it is clear that the energy splitting on the EuS substrate is noticeably higher than that on the Si/SiO_2 substrate. The red circles (blue squares) indicate the σ_+ (σ_-) incident polarization. The dots are experimental data, while the solid lines are fits obtained using the "absorptive and dispersive" line shape. Adapted from [36].*

2.8 Properties of the contact metal-TMDC interface

In order to perform optoelectronic experiments on ultrathin TMDC sheets, an essential prerequisite is the availability of Ohmic contacts. Achieving such contacts between a 2D semiconductor and a 3D metal electrode poses a significant challenge, for reasons explained in the following. In general, Fermi level pinning at the metal-TMDC interface, optimizing the contact with direct chemical bonding remains an open challenge [40] (see fig. 2.18).

A suitable measure for the contact quality (transparency) is the Schottky barrier height. It represents the potential energy needed for a charge carrier to propagate through the interface. According to the Schottky-Mott rule of Schottky barrier formation, the barrier for an n-type semiconductor is given by the difference between the vacuum work function of the metal Φ_{metal} and the vacuum electron affinity of the semiconductor (or ionization energy for a p-type one) χ_{semi}:

$$\Phi_{SB}^{(n)} \approx \Phi_{metal} - \chi_{semi} \tag{2.36}$$

Although some semiconductors obey well the Schottky–Mott rule and the model correctly predicts the existence of band bending in the semiconductor, it was found experimentally that it doesn't accurately predict the Schottky barrier height. The major issue is a phenomenon referred to as Fermi level pinning, which makes the Schottky barrier height almost completely insensitive to the metal's work function. In 1947, John Bardeen put forward that Fermi level pinning naturally arises if there were chargeable states in the semiconductor right at the interface. These states have energies inside the semiconductor's gap and they can be induced by the direct chemical bonding between the metal and semiconductor (metal-induced gap states), or already be present as surface states of the semiconductor. In both cases, these highly dense states are able to accept a large quantity of charge from the metal, whereby the semiconductor is shielded from the metal current flow. As a result, the Fermi level is pinned to a certain energy relative to the surface states inside the gap (see fig. 2.17).

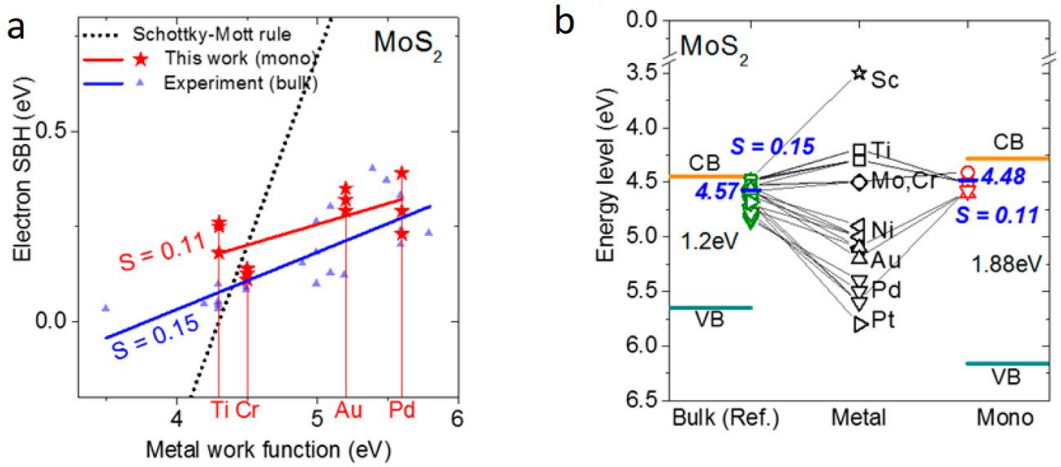

Figure 2.17: *Fermi level pinning of MoS2. (a) Schottky Barrier Height (SBH) of MoS2 for the various metal work functions. The pinning factor S was obtained from fits based upon Schottky-Mott model (dotted line), the bulk SBH (blue line), and the monolayer SBH (red line). (b) Comparison of the Fermi levels in the bulk MoS2 and monolayer MoS2 (orange line: conduction band edge; green line: valence band edge; blue bar: charge neutrality level; blue letters: the pinning factor). Adapted from [44].*

Experimental and computational studies point toward two additional causes of the Fermi level pinning, namely the surface states created from adsorbed contaminants, and possible interface damage due to kinetic energy transfer during metal deposition [43] (see fig. 5.1). This led to the view that through continued improvement of the metal deposition and FET fabrication, it should be possible to obtain clean metal-TMD interfaces without pinning. However, there are hints that the contact quality is also limited by the

fundamental bonding and chemistry at the $metal - MoS_2$ interface. While $metal - MoS_2$ contacts with vdW interactions have been engineered either by incorporating an intermediate layer (like HbN [29], Ti, or even graphene) or by using a metal with very low affinity to bond with sulfur [46], the transmittance of charge carriers will still be limited by the vdW barrier (see fig. 2.18).

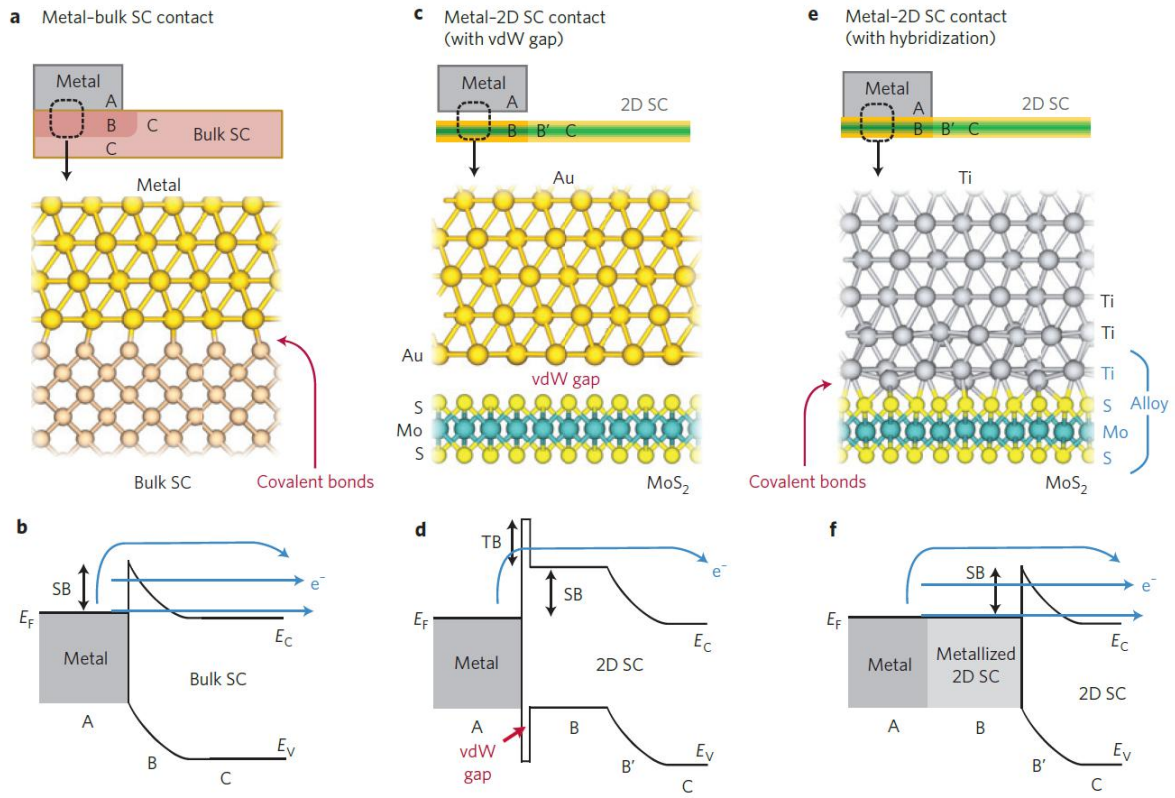

Figure 2.18: *Different types of metal–SC junction and their respective band diagrams. Schematic (a) and corresponding band diagram (b) of a typical metal/bulk SC interface. (c)(d) Metal/2D SC interface with vdW gap (for example, $Au - MoS_2$ contact). (e)(f) Metal/2D SC interface with hybridization (for example, $Ti - MoS_2$ contact, where MoS_2 under the contact is metallized by Ti). E_F, E_C and E_V represent the Fermi level of the metal, and the conduction and valence bands of the 2D SC, respectively. T_B and S_B indicate the tunnel and Schottky barrier heights, respectively. A, B, B' and C represent different regions in the current path from the metal to the SC. The blue arrows in (b), (d) and (f) represent the different injection mechanisms. From top to bottom: thermionic emission, thermionic field emission and field emission (tunnelling). In (d), only thermionic emission is available. Adapted from [40].*

Ultimately, even if the metal would not modify or restructure the TMDC-metal interface, moderate interatomic bonding that anchors the metal to the MoS_2 is needed for a high-mobility charge transfer in MoS_2-based FETs. Using atomic-resolution analytical scanning transmission electron microscopy (STEM), it has been possible to image and

characterize a contamination- and deposition damage-free interface between titanium and an MoS_2 channel in a FET to address the issue of pinning [30]. Titanium has a very strong affinity toward sulphur with a Ti-S bond dissociation energy of -3.69 eV (vs. -2.35 eV for Mo-S).Such Ti-S bond formation is likewise to be expected for WS_2.

As can be seen from fig. 2.19, the FET channel region shows a clean and flat MoS_2 monolayer in the bare region. By constrast, the monolayer under the evaporated metal is substantially distorted and hard to distinguish. This structural deformation is typical of TMDCs and severely compromises the contact quality.

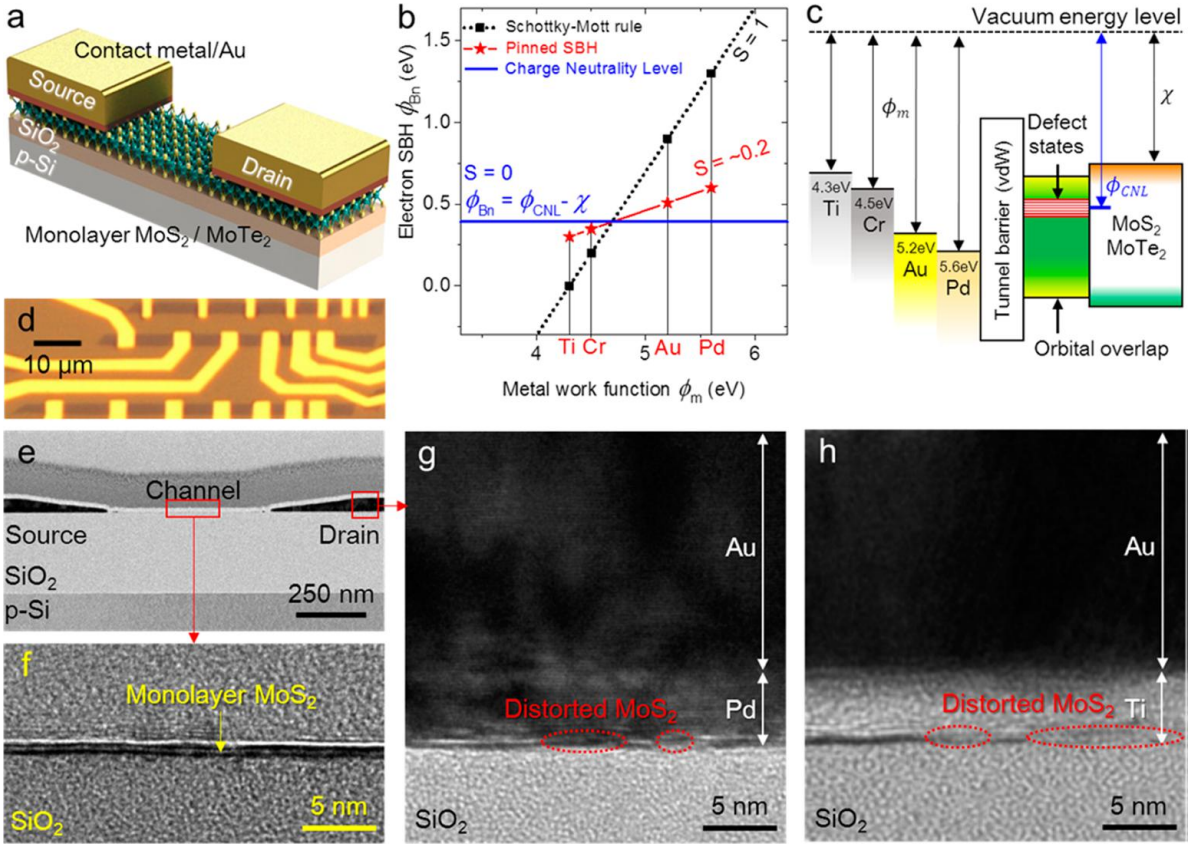

Figure 2.19: *Schematic illustrationof a FET comprising a monolayer MoS2 (or MoTe2) transport channel. (b) Definition of the pinning factor (S) and charge neutrality energy level (Φ_{CNL}). (c) Band diagram at the contact with interface states, including tunnel barrier (van der Waals gap), orbital overlapped TMDC under metal, and defect states. These can modify the SBH and induce Fermi level pinning. (d) Optical image of a device structure used for the transmission line method measurement. (e) Transmission electron microscopy (TEM) image of a monolayer MoS_2 transistor on a 285 nm thick SiO_2-covered Si wafer. (f) TEM image of the FET channel region. Between van der Waals gaps, monolayer MoS_2 is observed. TEM images of Pd contact (g) and Ti contact (h). Unlike the FET channel region, monolayer TMDC under the metal is distorted. Adapted from [40].*

Additional annular dark-field (ADF)-STEM imaging in conjunction with electron

energy-loss spectroscopy (EELS) furthermore enabled determining the changes in the atomic structure as well as the electronic structure at the interface between MoS_2 and Titanium [30] (see fig. 2.20).

In the first layers of the TMDC the peaks corresponding to Molybdenum and Sulphur are less pronounced - a strong indication that the atomic layer structure has lost its periodicity, in agreement with the ADF-STEM images. Moreover, layer 2 and even layer 3 can be seen to exhibit interfacial character since the peaks from sulphur are noticeably suppressed and some titanium edges can be identified [30]. Similar EELS analysis on an area of MoS_2 not in contact with Ti shows no change up to the fifth MoS_2 layer. Thus, only areas of the MoS2 channel directly in contact with Ti show changes in their electronic band structure. It can be concluded that the effects of the Ti contact on the MoS_2 channel go beyond the surface layer and, consequently, the pinning of the Fermi level likely is not limited only to the interface as speculated by previous papers [45]. Since the crystal structure of the topmost layer of MoS_2 is also degraded in areas in contact with Ti, the presence of Ti atoms in deeper layers cannot be ruled out.

From the above discussion, it becomes evident why optimizing contacts on monolayers or even few layer sheets of TMDCs constitutes a great challenge. Further details on that will be discussed in chapter 4.

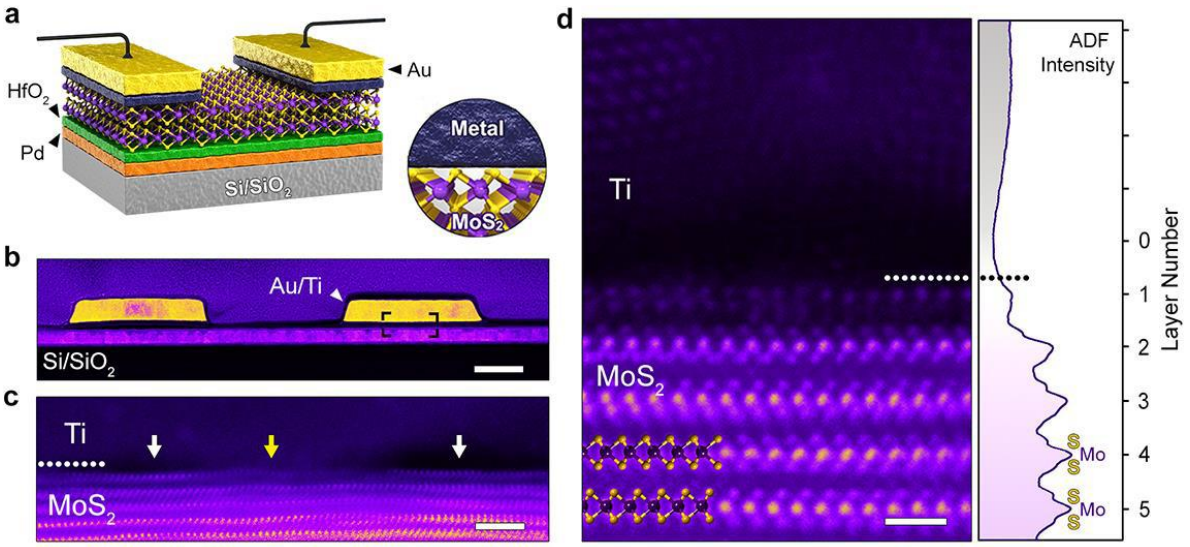

Figure 2.20: *Schematic layout and ADF-STEM images of a FET with a MoS2 channel: (a) Schematic layout of the FET showing the MoS_2 channel in contact with Au/Ti metal contacts and the remainder of the device. (b) Low-magnification cross-sectional ADF-STEM image of an actual FET prepared by FIB cutting. The protective amorphous C/Pt layers, also visible here, were deposited on top of the device during TEM sample preparation and are not part of the original FET. Scale bar is 0.2 μm. (c) High-magnification image of the $Ti - MoS_2$ interface acquired from the boxed area in (b). An area where Ti is clustered is indicated by a yellow arrow, and areas with void pockets are indicated by white arrows. Slight distortions in the lower MoS_2 layers are due to small wrinkling of the MoS_2. Scale bar is 2 nm. (d) Atomic-resolution ADF-STEM image of the $Ti - MoS_2$ interface acquired from a Ti clustered area. The topmost layer of MoS_2 is visibly altered compared to the pristine-like layers below. The horizontally-averaged ADF intensity of the image is shown on the right. A ball-and-stick model of MoS_2 is overlaid on the image for clarity of atomic positions. Scale bar is 1 nm. Adapted from [30].*

3 Experimental Techniques

As the miniaturization of electronic device components continues, it becomes necessary to identify new types of nanostructures and tailor their electronic properties. Top-down and bottom-up approaches are two complementary strategies for nanostructure fabrication.

The bottom-up approach provides convenient access to nanostructures of high structural quality. It works for a wide range of materials, especially if they do not belong to the class of layered materials. In general, wet chemical and vapor phase methods can be distinguished, the latter of which commonly yield samples of higher quality, i.e., a lower density of impurities and defects (see fig. 3.1). Nanostructures of high crystallinity can be obtained by evaporating the bulk material (source) at the hottest zone of a tube furnace under inert gas flow. The gas flow transports the material downstream, where it condenses on the colder surface and crystallizes. Size and shape of the resulting nanostructures are determined by the evaporation temperature, gas background pressure, amount of source materials, temperature gradient, gas flow rate and the type of deposition substrate.

The top-down approach requires a material whose dimensions can be reduced without significantly deteriorating its crystalline structure and integrity. For this reason, the layered materials are best suited for this approach, especially the TMDCs because, as explained before (section 2.2), their layers are bound to each other by van der Waals forces, which are notably weaker than the intralayer forces, such that they may be torn apart with limited breaking within the same layer. Thus, this approach can provide very good and clean flakes (fig. 3.1).

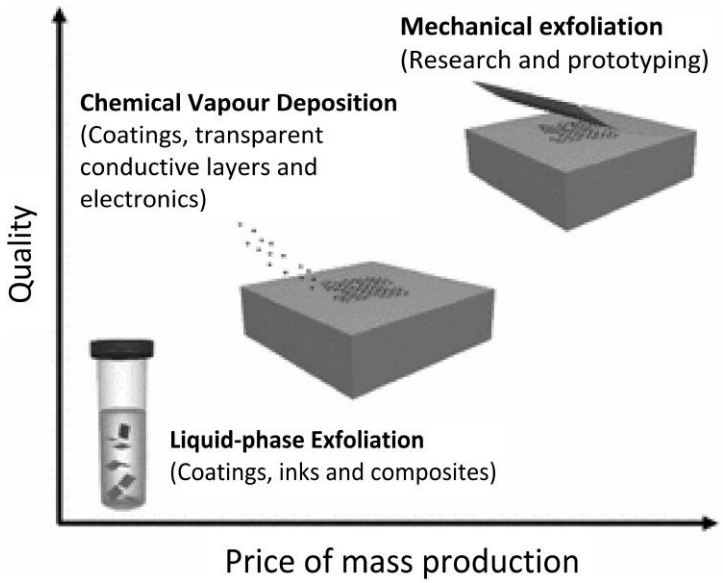

Figure 3.1: *Graphical representation of different exfoliation approaches, relating the price of mass production of the device using a certain technique and the corresponding quality of the sample produced. It also describes the most common uses for those specific techniques. It should be noted that mechanical exfoliation is difficult to scale up. Adapted from [53].*

3.1 Exfoliation

Various methods are used in order to thin down the layered materials, like intercalation. One approach starts with intercalation, whereupon ions are incorporated between the layers of the material in order to weaken the interlayer forces. Using agitation (like sonication), the layers can then be completely separated (see fig. 3.2).

In this thesis, the most common method is used, i.e., mechanical exfoliation. It involves the cleaving and thinning of a layered materials with the aid of an adhesive tape. In general, exfoliation requires that the material consists of only weakly (van der Waals) bonded layers. Suitable layered materials include graphite, and TMDCs like MoS_2, WSe_2 and WS_2.

The used substrates were silicon wafers covered by a thermally grown SiO_2 layer of 300 nm thickness to prevent the leakage current from the backgate. . After evaporating position markers (Ti/Au) required for the later e-beam lithography, the substrate can be covered with Poly(methyl methacrylate) (PMMA) and cut. Subsequently, it is cleaned in an ultrasonic bath with N-ethyl-2-pyrrolidone (NEP), aceton and isopropyl alcohol consecutively for fiffteen minutes each, and then it is blown dry with argon gas flow. To increase the adhesion to the substrate, it is cleaned by an oxygen plasma treatment for at least 10 min with a power of 100 W and a gas pressure of 0.4 mbar, and subsequent heating to 130 °C. Thus obtained substrates are ready to be used in the next steps.

For the mechanical exfoliation, blue Nitto tape (Nitto Denko Co., SPV 224PR-M) gave very good results, due to the limited residuals and the low adhesion, in order to prevent the flakes from breaking during the repeated folding and unfolding. By pulling adhesive tapes off each other, the material is thinned down until, in the last step, the adhesive tape is pressed onto the Si/SiO_2 substrate in order to transfer the ultrathin sheets. During this last step, a hot plate is used to heat the substrate, in order to ensure a better adhesion between the flakes and the substrate. After the latter is heated up in contact with the substrate, both can be removed from the hotplate to cool down, allowing the tape to retract and release the flake onto the substrate previously prepared.

The thickness of the exfoliated sheets may be further reduced by laser thinning, where a high power laser beam is used to sublimate the top most layers. Similarly, lateral structuring is achievable by reactive ion or wet chemical etching, in order to pattern the flake into a shape compatible with the device configuration. However, such processing is challenging for very thin flakes, which due to their fragility can be easily damaged.

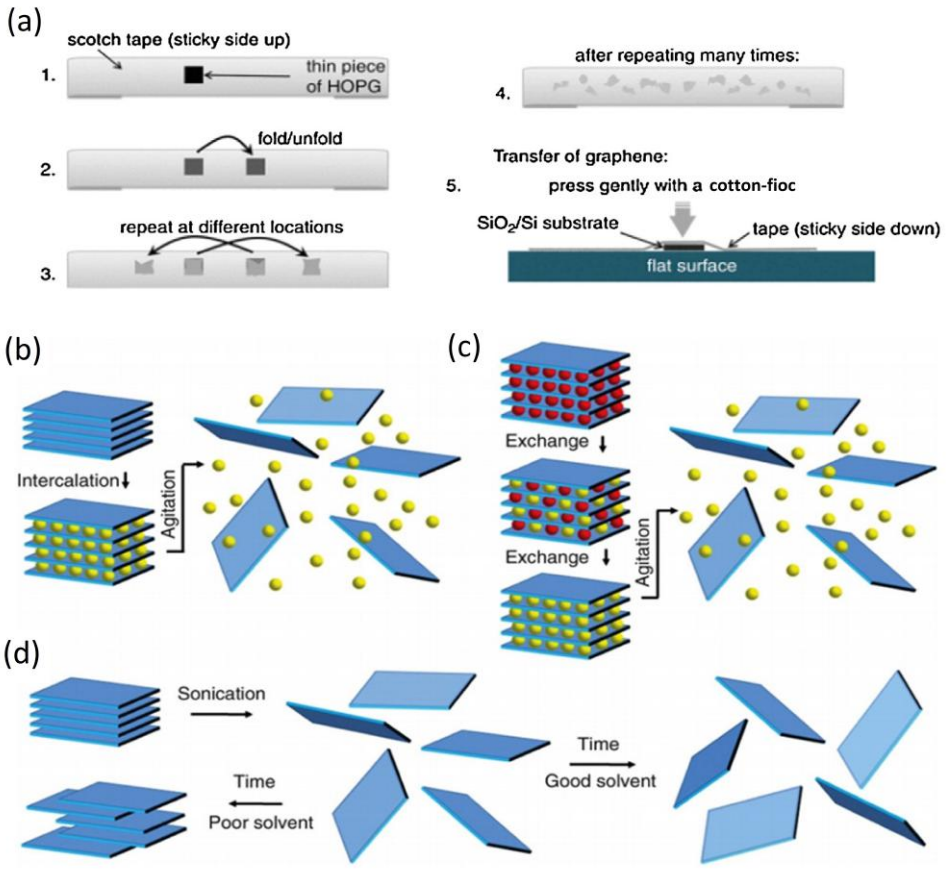

Figure 3.2: *Schematic illustration of the most common top-down approaches to exfoliate layered materials. (a) Mechanical exfoliation, which is the technique that has been used during this project. (b),(c): schematic description of liquid exfoliation of layered graphite materials. Ions (yellow spheres) can be intercalated between the layers, thereby expanding the crystal and weakening the interlayer attraction. Subsequently, two techniques can be used in order to completely separate the layers, namely agitation (such as sonication), resulting in an exfoliated dispersion (b), or ion exchange, in which the ions (red spheres) can be exchanged in a liquid environment for other, usually larger, ions (yellow spheres) (c). (d) Sonication-assisted exfoliation, involving sonication of the layered crystal in a solvent, resulting in exfoliation and sheet formation. Adapted from [51] and [52].*

Once the material is placed onto the substrate, it can be analyzed using an optical microscope in order to identify the thinnest flakes. For this purpose, the light source is directed against the sample, which helps distinguishing the flakes of different thickness according to their coloration and contrast. In this manner, it is possible to identify flakes down to 3-4 nm thickness, whereas thinner WS_2 flakes interact too weakly with the light to be distinguished.

The acquired microscopic images will be useful later for designing the metal contacts at the desired locations.

3.2 Atomic Force Microscopy

Once the WS_2 has been exfoliated on top of the Si/SiO_2 substrate, the topography of the WS_2 flakes surface need to be investigated, in order to determine their thickness, but also to get detect possible glue residuals, structural irregularities, or mechanical defomration or even breaks. For this purpose, atomic force microscopy (AFM) is often employed and in the present work all AFM images were taken using a Dimension Icon Scanning Probe Microscope by Bruker.

In a typical AFM experiment, a microfabricated cantilever with a sharp tip is being oscillated slightly below its resonant frequency by a drive signal, applied to the piezo-crystal. In this so-called *tapping mode*, a feedback loop maintains a constant oscillation amplitude, and adjusts the distance between the probe and the surface accordingly. The fact that the oscillating tip is not directly touching the surface ensures that the flake is not damaged during scanning.

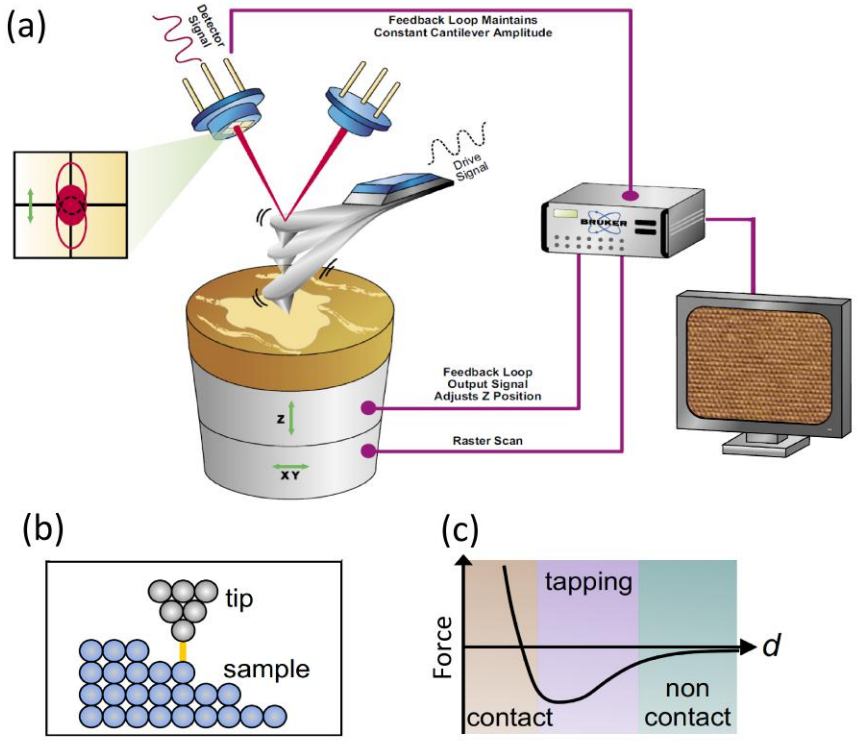

Figure 3.3: *Schematic representation of the Atomic Force Microscope in tapping mode. (a) A drive signal, applied to the "tapping piezo", mechanically oscillates the probe at or near its resonance frequency (usually the fundamental resonance). Zoom into the tip-sample interaction on the atomic level (b) and tip-sample interaction force as a function of tip-surface distance (c). Adapted from [54].*

The deflection of the cantilever is detected with the aid of a reflected laser beam

which is collected by a photodiode, thus yielding information about the vertical height of the sample surface (fig. 3.3(a)), together with the cantilever oscillation amplitude and its phase [54].

In this manner, a topographical image of the sample surface is obtained in a non-invasive manner, scanning line-by-line. Fig. 3.3(b) illustrates the tip-sample interaction at the atomic scale. The corresponding force depends on the distance between tip and sample as shown in fig. 3.3(c). Depending on the force range, three accessible AFM scanning regimes, namely contact, non-contact, and tapping mode, are defined, but they were not employed in the present work.

In fig. 3.3, a typical AFM topographic image recorded on a WS2 flake is shown (panel a), along with two cross-sectional profiles along the two different horizontal lines (fig. 3.4(b) and (c)). The latter were obtained using the software WSxM 5.0 [61].

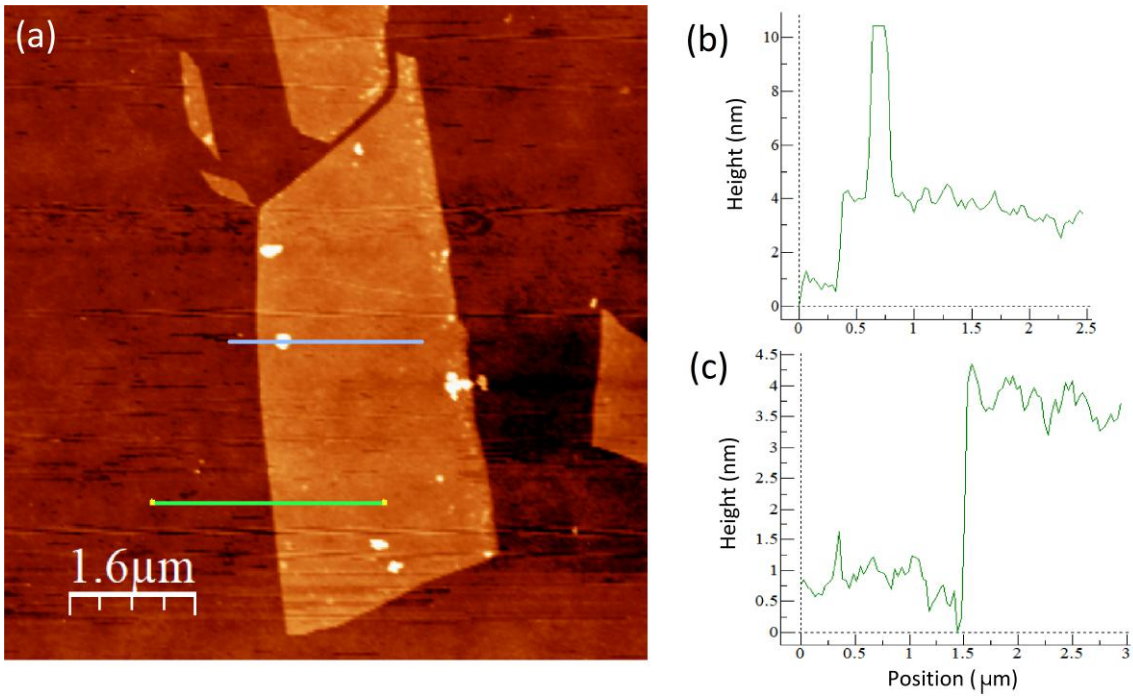

Figure 3.4: *Typical topographic AFM image of a WS_2 flake. From such type of images, the flake height can be derived by analyzing the section with the WSxM software. (b,c) Thus obtained height profiles, taken along the blue and green horizontal line in the topographic image. Some glue residuals can be recognized on top of the flake (b), with a height of up to 10 nm (sometimes even 30 nm). The flake thickness is around 3.5 nm, which corresponds to approximately 5 layers.*

3.3 Electron Beam Lithography

As mentioned before, the substrate is equipped with markers which help to identify the flakes and align the electron beam with the contact design such that they can be placed at the correct position.

This allows to precisely align the contacts with respect to the flakes within the e-beam software. The electron beam lithography (EBL) system will use this vectorial design to perform the corresponding exposure.

The EBL consists of several components, specifically an electron source, an optical setup with lenses for the e-beam guidance, a deflection unit to deviate the beam from the sample while setting up, a pattern generator, and a laser interferometer controlled stage, as shown in fig. 3.5(a). The sample chamber is kept at a pressure of $10^{-6} mbar$ in order to avoid the backscattering of the electrons and to limit the relative noise.

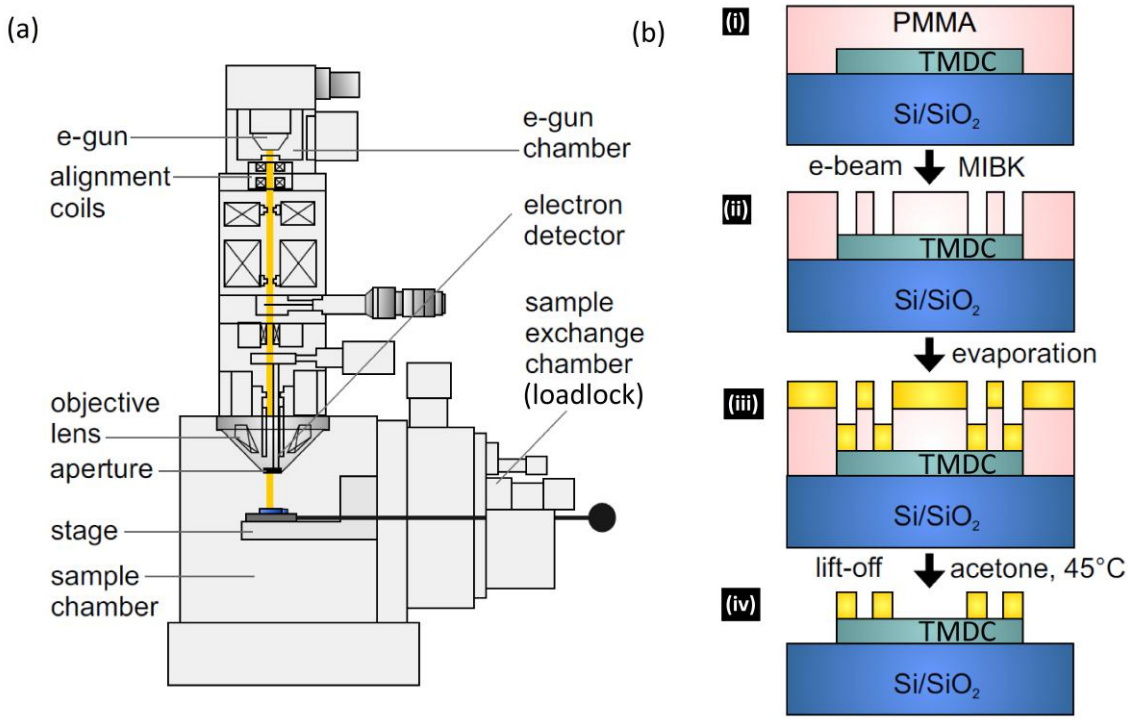

Figure 3.5: *Cross-sectional view of an electron beam lithography system. (b) A generalized step-by-step EBL fabrication process for the electrical contacting of TMDCs structures, involving in total four major steps.*

An advantage of EBL over optical lithography is the smaller wavelength of the electrons in comparison to photons (in the visible or UV range), which enables a better spatial resolution. The resolution accessible by a certain particle can be estimated from the de Broglie relation, which relates its momentum to its wavelength. To calculate the

momentum, the relativistic energy-momentum relation can be exploited:

$$E^2 + p^2c^2 = m^2c^4 \tag{3.1}$$

where m is the particle mass and c is the speed of light. The usual value for the applied voltage of 20 kV has been used, so $E = q * V = 2 * 10^4\ eV = 3,2 * 10^{-15}\ J$. By using the de Broglie relation, the electron wavelength, which governs the spatial resolution, is obtained as:

$$\lambda = \frac{h}{p} \simeq 2,45 * 10^{-12} m \tag{3.2}$$

where h is the Planck constant.

In order to write the contacts, the substrate is first covered with a positive resist, which is chemically modified by the e-beam in the exposed areas into a predefined pattern and is subsequently removed by a developer solvent. Metal contacts are then thermally evaporated onto this resist mask and after the lift-off process, the deposited metal adheres to the substrate in the exposed areas, while the rest of the underlying resist is removed.

The e-beam writing process requires the initial setup of the beam, that has to be focused and aligned, then the process of writing follows the contact design defined before. For the smallest structures like the contact on the flakes (see fig. 3.6(a)), the beam with an acceleration of 20 kV and an aperture of 10 μm is used, while for the larger structures (fig. 3.6(b)) respective values of 20 kV and 120 μm are chosen.

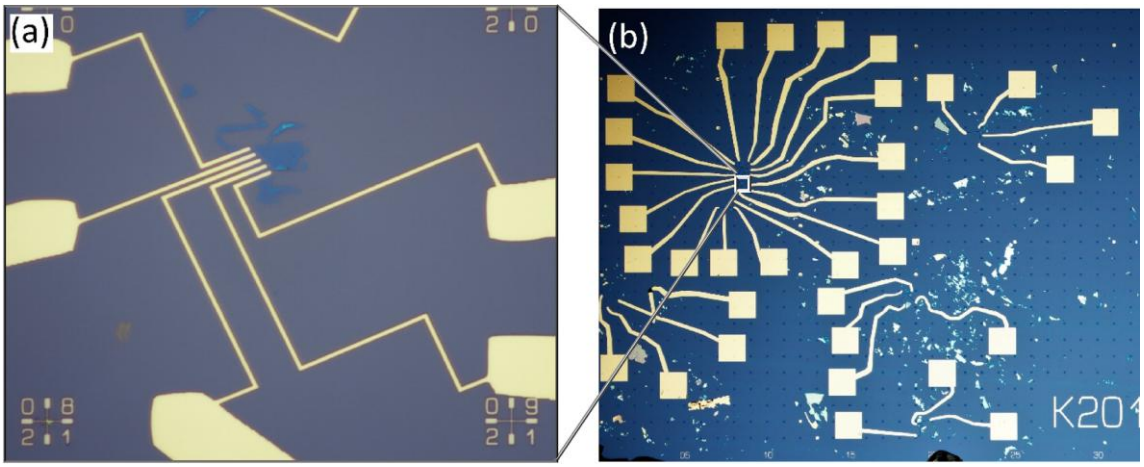

Figure 3.6: *(a) Optical image of a contacted WS_2 flake, with the metal electrodes arranged in series. (b) Optical overview image (zoom out), revealing the connection between the pads that are needed for the wire-bonding and the smaller structure in (a).*

The e-beam writing process is schematically illustrated in fig. 3.5(b). In this work, polymethyl methacrylate (PMMA) resist, dissolved in chlorobenzene, is spin-coated onto

the substrate at 6000 rpm for 35 seconds, and then it is baked at 160 °C for 4 minutes. A two-layer system is used, comprising a bottom PMMA layer with a molecular weight of 200K and a concentration of 3.5%, followed by a second, higher molecular weight layer (950K) at 2.5%. The PMMA bilayer ensures the formation of an undercut during the development, which facilitates access of the solvent during the lift-off process. The former step is performed with a methyl isobutyl ketone (MIBK) - isopropyl alcohol (IPA) mixture (1:3 ratio) for 105 seconds (step (i) in fig. 3.6) and then rinsed with isopropyl alcohol.

Besides lithography, the e-beam writer can also be used as an imaging tool (i.e., a scanning electron microscope, SEM) across the sample surface in order to accurately align the sample with the contact design and focus the beam. SEM imaging relies upon the detection of secondary and backscattered electrons are collected by a detector, yielding a surface image with high spatial resolution and excellent topographic contrast.

In the next section, the contact evaporation (step (iii) in fig. 3.5(b)) will be explained.

3.4 Evaporation and connection of the contacts

The electrode metals are deposited by thermal evaporation in a vacuum chamber (fig. 3.7). Different contact metals are used to facilitate current injection into the WS_2 flakes. Titanium (1 nm) serves as an adhesion layer for the gold contacts (60 nm). Other metals that have been tested are chromium, permalloy, and ferromagnetic contacts like cobalt.

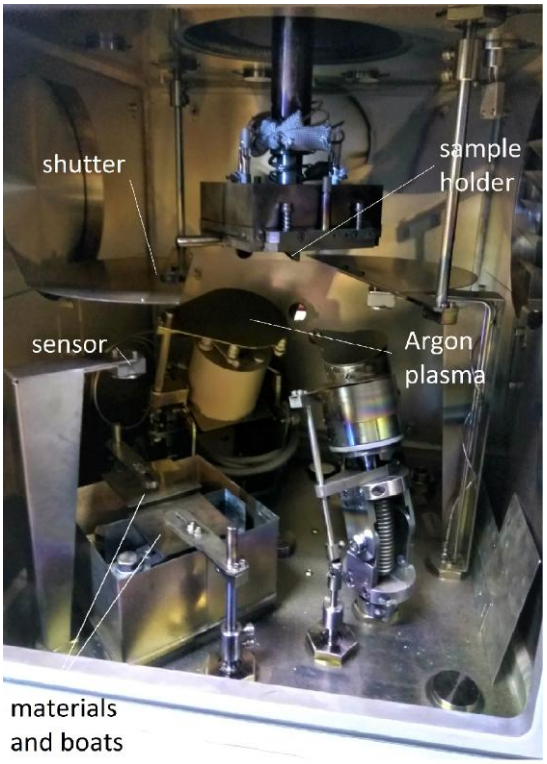

Figure 3.7: *Optical image of the ultrahigh vacuum chamber of the evaporation machine.*

For contact metal evaporation, the sample holder is rotated in front of the boats in order that the evaporated material will be uniform and will not create any shade on the sample. Then the chamber is evacuated overnight (about 12 hrs) to obtain a residual pressure of $5 * 10^{-8} mbar$. To ensure Ohmic contacts and to clean the flake surface from any residuals before the evaporation, some samples were subjected to a surface cleaning process. For this purpose, the developed sample is exposed to Ar-plasma (100 Watt, 0.4 mbar) for five seconds. This short time is necessary to avoid breaking or damaging of the flakes. Importantly, this process is directly followed by metal evaporation without breaking the vacuum.

Initially the boats are heated up by passing a current of few Ampéres, and when the evaporated gas flow has reached the optimal rate (e.g. $1,8 \mathring{A}/s$, for gold contacts), then the shutter opens and the evaporation begins, with a quartzbalance sensor generating a feedback loop to maintain the constant evaporation rate automatically.

Once the one or two metal layers have been evaporated, the lift-off is done using acetone for one hour roughly and residual metal films on the edges of the sample are removed with a toothpick. Then the sample is rinsed with isopropyl alcohol. In some cases (especially for contacts made only of gold) the lift-off required 2 hrs on the hot-plate at 45 °C.

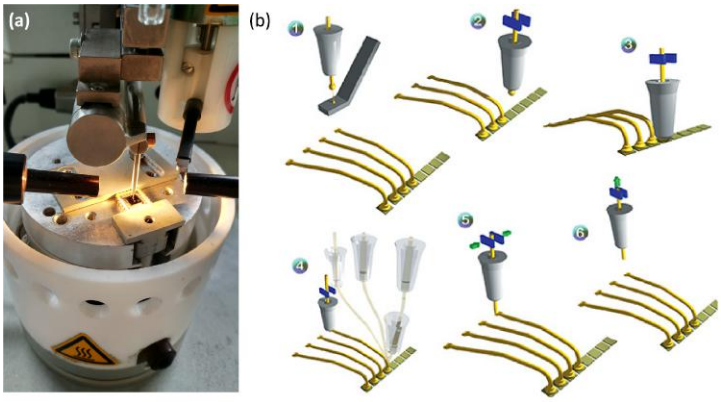

Figure 3.8: *(a) Optical image of the bonder head. (b) Schematic depiction of the steps needed to complete one of the connections between the chip carrier and the sample.*

Some samples gave improved results after annealing at 200 °C (reached using a heating rate of 50 °C per min), This temperature is maintained for at least 2 hrs. During ramping up, the system is cleaned by exposure to forming gas (Ar/H_2). When the temperature is reached, the forming gas gas is introduced at a pressure of 10^{-4} mbar and then maintained constant in the chamber.

The substrates are glued with conducting silver paste into a chip carrier which allows for 19 electrical connections, plus the one used for the backgate voltage. The bond pads are connected to the chip carrier via ultrasound-assisted wedge bonding of gold wires (fig. 3.8(a)).

The wirebonder heats up the sample and the chip carrier to 65 °C, then the tip presses the gold wire on one contact of the chip carrier, and then moves over the corresponding big pads of the sample and presses again in order to release the wire attached to the sample (see fig. 3.8(b)).

To minimize reaction with ambient air, all the devices were kept in a vacuum desiccator.

3.5 Electrical measurements

Once the sample is connected to the chip carrier, it can be mounted into the chip socket. The latter is equipped with 20 metal pins, one of which is electrically connected with the metalized bottom side of the sample for application of a backgate voltage. Low-noise coaxial cables (MCX connector to BNC) with an additional semiconducting layer between the insulation and the shield provide the electrical connection between the breakout box and the amplifier stage or the AC/DC input. The amplifier stage consists of individual modules (Keithley 2400), which are connected and operated by a bus board transmitting the control and measurement signals from and to the computer. The latter communicates

with the measurement setup (sourcemeters and multimeters) and then processes and store the received data, using the Labview software. The overall system is sketched in fig.3.9.

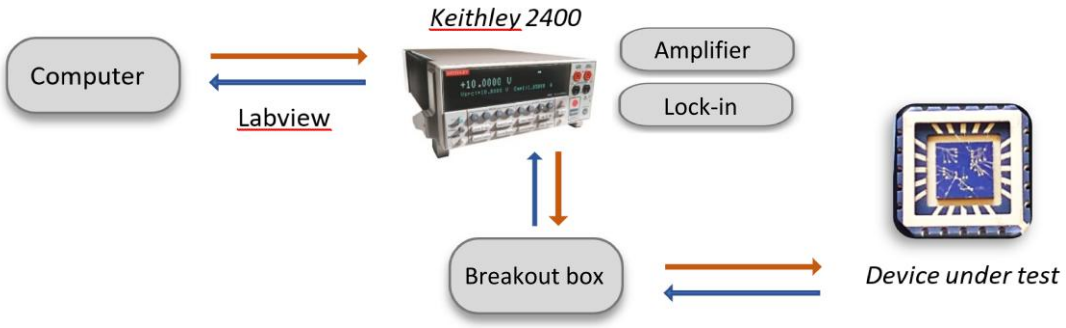

Figure 3.9: *Schematic representation of the AC/DC input starting from the input from the computer through the Labview VI (virtual instrument), which communicates with the Keithley sourcemeter (DC measurements) or the lock-in (AC measurements) to apply a gate voltage and a drain-source voltage. This signal is transmitted to the designated ports of the breakout box and then to the sample, where a voltage drop under current flow is detected (in case of 4-probe measurements). Via an additional amplifier and the Keithley instrument, the signals go back to the computer where they are registered by the Labview VI.*

The voltage-source module provides voltages in the ranges 100 mV/V, 10 mV/V, 1mV/V, and 100 V/V over the DC input. A differential amplifier module measures the voltage drop between two signals, can apply some low-pass and high-pass filters, and provides high impedance signal amplification before digitalization with gains in the range of 1-1000. A separate current-meter module (Keithley 2400 multimeter) measures the signal with the help of a high-resistance, low-noise operational amplifier, which provides the feedback resistance for the set current range. Gate voltage is applied with a Keithley 2000 source-meter, which supplies up to 100 V with 3 mV resolution.

3.5.1 Cryogenic transport measurements

The electrical transport measurements presented in chapter 4 needed to be carried out at low temperatures in order to reduce thermal noise and with the aim of distinguishing the signals from different valleys (see section 2.3). To this end, the measurements have also been performed in an Oxford cryostat equipped with a 12 T magnet (see fig.3.10). The sample is mounted on an insert directly connected to the breakout box for measurements in the range of 1.4-300 K. The insert is then slowly lowered directly into the ^4He bath. By pumping on the ^4He reservoir, the temperature decreases to 1.4 K.

Temperature control is performed by the ITC503 from Oxford Instruments, combined with three cartridge heaters and four sensors, like Cernox ones which monitor the temperature at the 1 K pot.

The operation of the cryostat relies upon the continuous presence of liquid helium into the cryostat heat exchanger. Every few days this requires the liquid Helium to be pulled from the Dewar all the way through the system. The heat exchanger thus removes heat from the column of gas and the metal in the sample space which in turn removes heat from the sample. The temperature control is accomplished through a heater at the cryostat heat exchanger, the current to which is proportionally controlled by a sensor on the latter and a set point on the temperature controller in the rack.

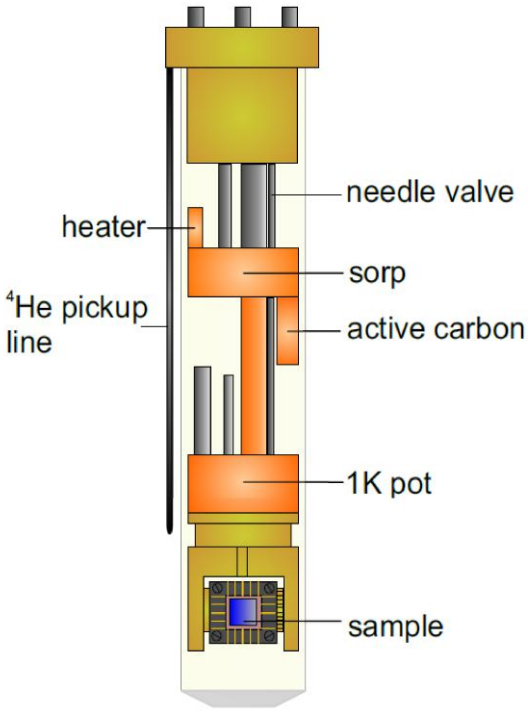

Figure 3.10: *Schematic diagram of the HelioxVL 3He insert with rotatable chip socket.*

3.5.2 Lock-in Amplifier

The measurements inside the cryostat have been performed in DC and AC mode. In the latter case, a low frequency AC-voltage is applied via a 7265 dual phase DSP lock-in amplifier, which can be combined with a Keithley 2400 DC-input via a home-built DC offset adder module running on batteries. As previously described, a differential amplifier module measures the voltage drop between the two inner probes (see section 3.6), applies some low-pass and high-pass filters, and provides high impedance signal amplification to a similar lock-in synchronized with the first one. All electrical measurements are controlled and recorded via a LabView interface.

In its most basic form the lock-in amplifier is an instrument with dual capability. It can recover signals in the presence of a strong noise background, or alternatively enable high resolution measurements of relatively clean signals over several orders of magnitude and frequency.

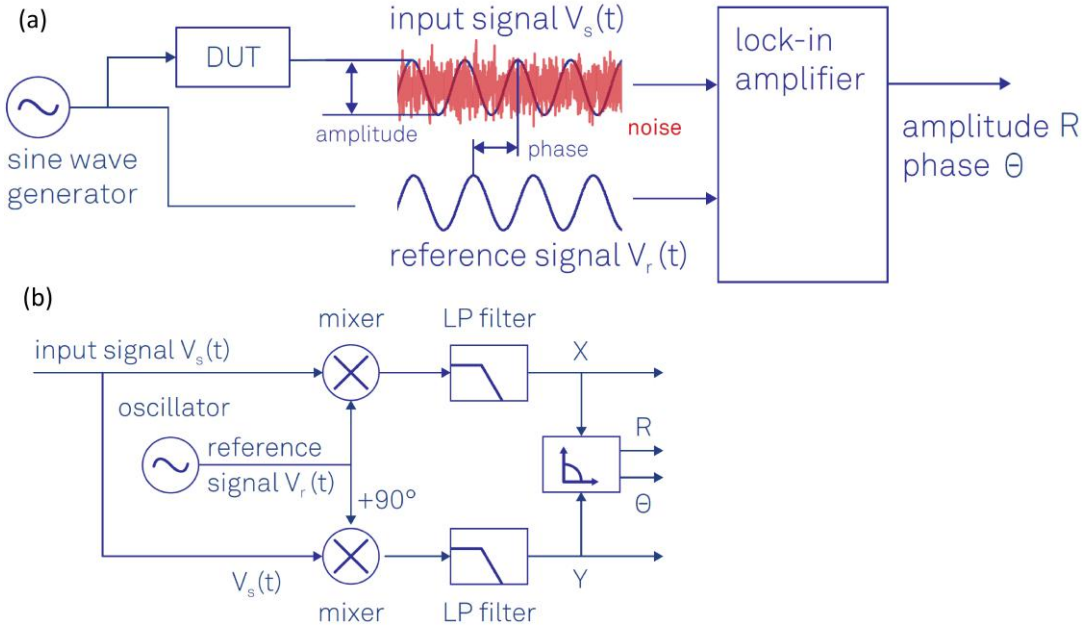

Figure 3.11: *(a) Sketch of a typical lock-in measurement. A sinusoidal signal drives the DUT and serves as a reference signal. The response of the DUT is analyzed by the lock-in which outputs the amplitude and phase of the signal relative to the reference signal. (b) Schematic illustration of the lock-in amplification principle: the input signal is multiplied by the reference signal and a 90° phase-shifted version of the reference signal. The mixer outputs are low-pass filtered to eliminate the noise and the $\omega_r + \omega_s = 2\omega$ component, and finally converted into polar coordinates. Adapted from [55]*

During the measurements, the device under test (DUT) is stimulated by a sinusoidal signal, as shown in fig. 3.11. The device response $V_s(t)$ as well as the reference signal $V_r(t)$ are used by the lock-in amplifier to determine the amplitude R and phase Θ. This is achieved using a so-called dual-phase demodulation circuit, where the input signal is split and separately multiplied with the reference signal and a 90° phase-shifted copy of it. Based upon the basic relations:

$$V_s(t) = \sqrt{2}Rcos(\omega_s t + \theta) \tag{3.3}$$

$$V_r(t) = \sqrt{2}e^{-i\omega_r t} \tag{3.4}$$

the complex signal after mixing is given by [55]:

$$Z(t) = V_s(t) \cdot V_r(t) = R\left[e^{i[(\omega_s - \omega_r)t + \theta]} + e^{-i[(\omega_s + \omega_r)t + \theta]}\right] = X(t) + iY(t) \tag{3.5}$$

The outputs of the mixers pass through configurable low-pass filters; this process is represented in fig. 3.12(c)(d) and mathematically expressed as an averaging of the moving vectors over time (red line), stripping away the noise and the fast rotating term at

$|\omega_s - \omega_r|$ (blue line) by setting $\langle e^{-i[(\omega_s+\omega_r)t+\Theta]}\rangle = 0$. The averaged signal after filtering becomes

$$Z(t) = Re^{i[(\omega_s-\omega_r)t+\theta]} \tag{3.6}$$

Since normally the frequency of the output signal is equal to the signal imposed on the DUT, then $\omega_s = \omega_r$, whereby the above equation further simplifies to:

$$Z(t) = Re^{i\theta} \tag{3.7}$$

where the absolute value R is the root-mean-square amplitude of the signal and the phase Θ is relative to the reference signal. To be more precise, in the demodulation process, the reference signals are mixed with the device output in the forms $V_r = cos(\omega_r t)$ (fig. 3.12(a)(b)) and its 90 degrees phase-rotation $V_r = -sen(\omega_r t)$. Mixing these, the outputs of the lock-in are the in-phase component X and the quadrature component Y, which are given by:

$$X = Re(Z) = Rcos\Theta \tag{3.8}$$

$$Y = Im(Z) = Rsen\Theta \tag{3.9}$$

Therefore, the absolute value R of the device signal can be derived from X through[55]:

$$R = \frac{X}{cos\Theta} \tag{3.10}$$

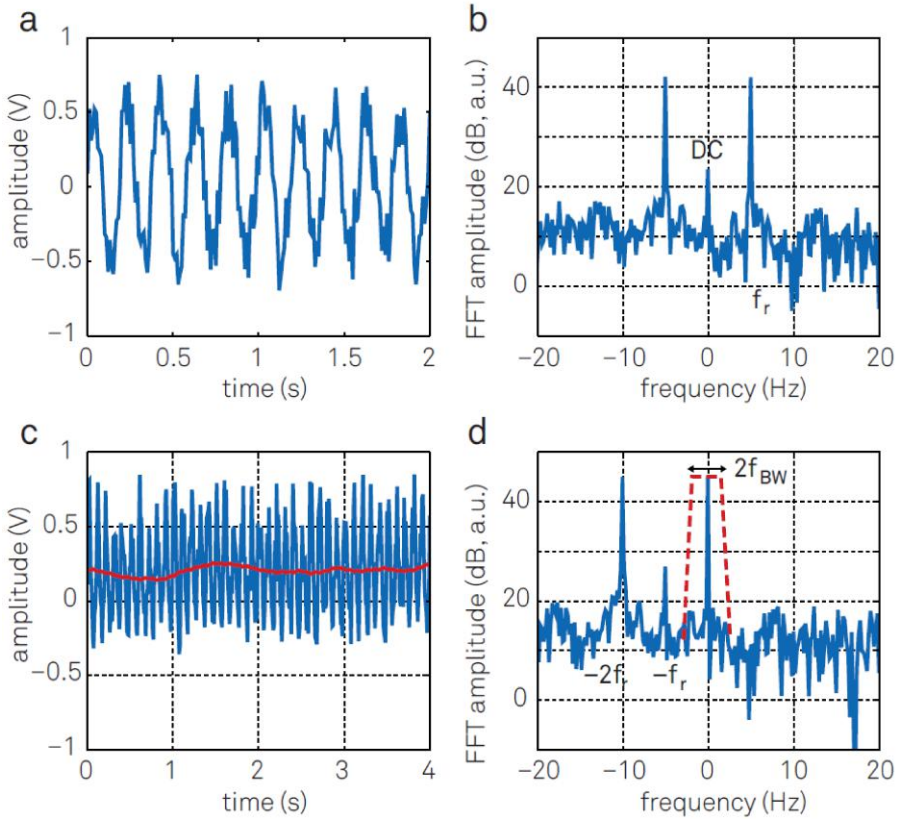

Figure 3.12: *Relationship between time and frequency domain representation before and after demodulation. (a) Sinusoidal input signal superimposed with noise displayed over time. (b) Same signal as in (a) represented in the frequency domain. (c) After mixing with the reference signal (blue trace) and low-pass filtering (red trace), the signal spectrum up to f_{BW} remains. (d) In the frequency representation, the frequency-mixing shifts the frequency components by $-\omega_r$. The filter then picks out a narrow band of f_{BW} around zero. Note the component at frequency $-\omega_s$, which comes from offset and 1/f noise in the input signal. For accurate measurements this component has to be suppressed by proper filtering. Adapted from [55]*

3.6 4-probe measurements

In two-terminal electrical measurements, a voltage is applied between two contacts, and the induced current is measured via the same electrode pair (see 3.13 (a)). Thus, the two-terminal resistance is the sum of the internal resistance R_{ch} (channel resistance), and the contact resistances R_c at the two contacts. For low resistance measurements, where R_{ch} and R_c are comparable, this introduces a significant source of noise and error. Especially because the Schottky barrier and other capacitive interface effects sensitively influence such measurements.

This problem can be avoided by performing the measurements in a four-terminal

configuration, in which the outer electrode pair is used to pass a current through the sample, and the resulting voltage drop is measured between the inner pair, called sense leads (see 3.13 (b)). In this manner, there is essentially no voltage drop due to R_c, and the measured voltage V_{ab} is equivalent to the voltage drop across $R_c h$. On this basis, the channel (material) resistance can be derived as the ratio between V_{ab} and the applied current.

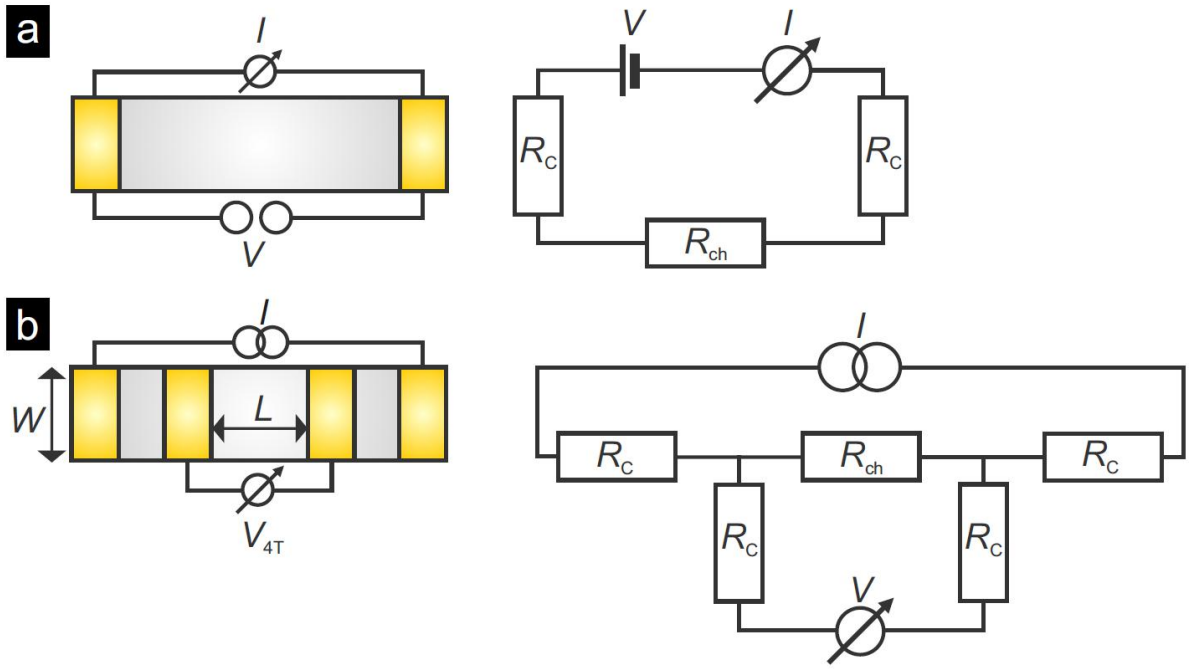

Figure 3.13: *Contact configuration and corresponding equivalent circuit for (a) 2-probe and (b) 4-probe electrical measurements.*

Due to the intricate electrical behavior of the metal/TMDC interface, the best results in this thesis have been achieved with the van der Pauw configuration, where the contact area is reduced to its minimum and there are no parallel contacts. The van der Pauw method comprises a four-point probe placed around the perimeter of the sample (fig. 3.14(b-d)), rather than linear four point probe. In this manner, a (geometrically) averaged resistivity of the sample is obtained, whereas a linear array provides the resistivity in the sensing direction.

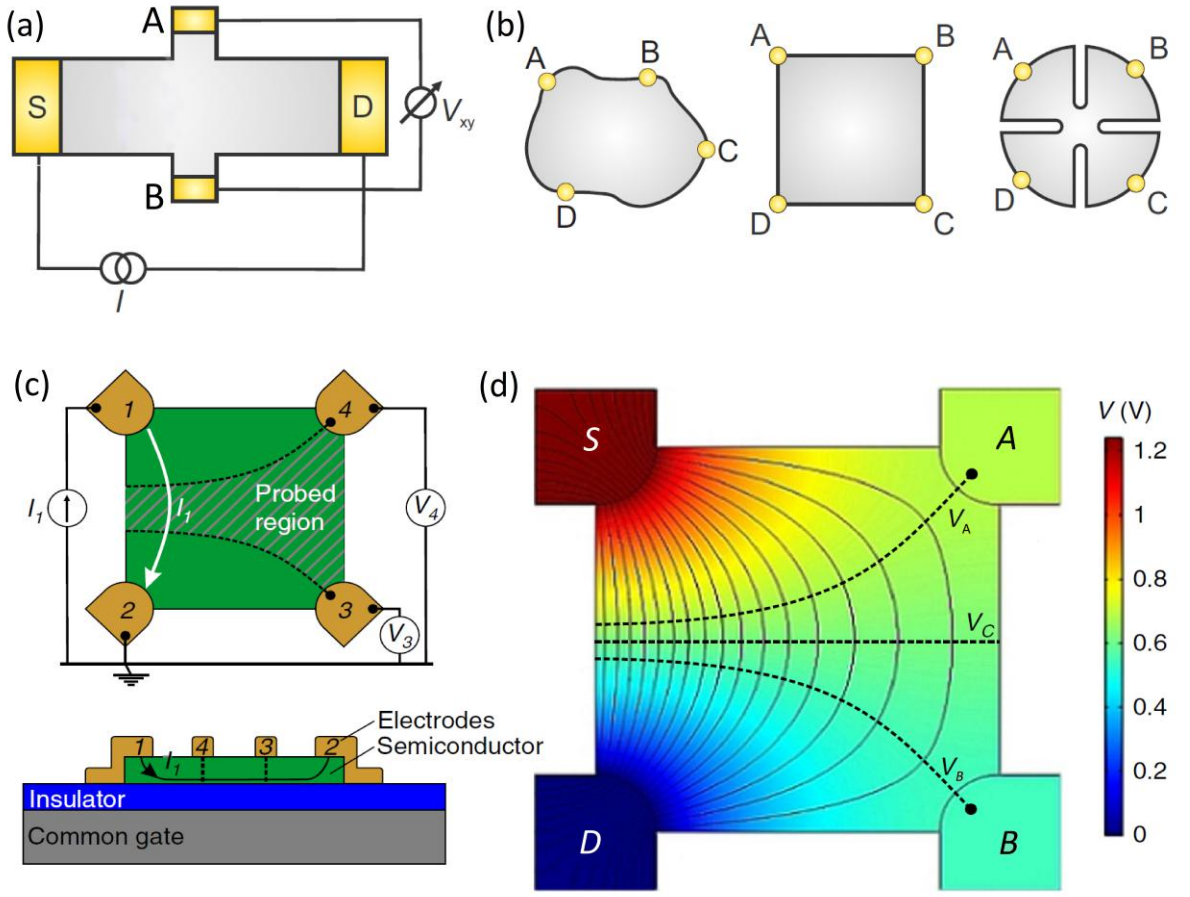

Figure 3.14: *Hall bar and van der Pauw transport measurement geometries. (a) 4-probe measurement schematic for the Hall bar configuration. (b) Different geometries of the van der Pauw method. The third one is optimal, while the other two provide only approximate results. In this thesis, the flake geometry could not be defined and the first two situations are the most common. (c) Top view of a van der Pauw device fabricated on a common gate and insulator. At the bottom, the related pseudo-cross-section view, where all contacts are projected on the same plane for convenience. (d) Potential map and current density streamlines in the van der Pauw device in linear regime. The dashed lines are equipotential lines* V_3, V_4 *and* $V_C = (V_3 + V_4)/2$*. Adapted from [56].*

As shown in fig.3.14 (d),the current induced between source (S) and drain (D) creates an electric field in the sample, and correspondingly a potential drop V_{AB} on the opposite two contacts A and B. In the case of an arbitrarily shaped flake (as commonly obtained by mechanical exfoliation), at least two sets of measurements are required to account for geometrical errors and possible material anisotropies. In this thesis, four sets of measurements have been carried out by subsequently rotating the sample leads by 90°, in order to obtain average values for the horizontal and vertical resistance. From the

schematic depiction in fig. 3.14(c), it follows:

$$R_{12,34} = \frac{V_{34}}{i_{12}} \tag{3.11}$$

where i_{12} is the current between source (1) and drain (2), and V_{34} is the voltage drop $V_4 - V_3$ across the opposite edge between the contacts 4 and 3. Thus, the vertical and horizontal average resistances can be calculated as:

$$R_{\text{vertical}} = \frac{R_{12,34} + R_{34,12}}{2} \tag{3.12}$$

$$R_{\text{horizontal}} = \frac{R_{23,41} + R_{41,23}}{2} \tag{3.13}$$

The sheet resistance R_s can then be accessed through the van der Pauw formula[57]:

$$e^{-\pi \frac{R_{\text{vertical}}}{R_S}} + e^{-\pi \frac{R_{\text{horizontal}}}{R_S}} = 1 \tag{3.14}$$

Moreover, a magnetic field can be applied in order to characterize new materials in terms of charge carrier density, doping level, mobility, as well as magnetoresistance effects. The most commonly employed configuration is the Hall bar, where a current is imposed using opposite source and drain contacts and the voltage drop is measured between the two remaining contacts (see fig. 3.14(a)). On the other hand, it is also possible to measure magnetoresistance effects with van der Pauw geometry.

4 Results

In practice, electrical transport experiments on TMDCs are challenging due to the difficulty to achieve high-quality, quasi-Ohmic electrical contacts. In fact, recent studies of TMDC-based FETs have shown that they behave like Schottky barrier transistors whose switching is controlled by the tuning of the Schottky barrier at the contacts ([64] and [46]). For Schottky barrier transistors, the intrinsic properties of the TMDCs channel are masked by the Schottky contacts. In the past few years, numerous attempts have been made to overcome this limitation. A major focus has been on testing different contact metals including Al, Ti, Cr, Ni, Au, Pt, and many others. Unfortunately, most of the metal-semiconductor (M-S) contacts showed non-negligible Schottky barriers regardless of the contact metals. . Recent works have reached a contact resistance on the order of $R_{contact}$ of 0.8 $k\Omega \cdot \mu m$ for TItanium on 15 layers of MoS_2; however, much larger values up to 740 $k\Omega \cdot \mu m$ were observed in case of monolayer MoS_2 [65]. In general, it is difficult to achieve a low contact resistance even for low work function metals on TMDCs, because the Fermi-level gets pinned at the charge neutrality level (CNL) as shown in fig.2.17. For WS_2, achieving low contact resistance is even more challenging than for most TMDC, as its CNL is located in the middle of the bandgap, which leads to larger Schottky barriers for electrons compared with MoS_2. As described in section 2.8, the biggest issues are related to Fermi level pinning and the interaction between the metals and the TMDCs in the first layers. Accordingly, current research is focusing on optimizing the contact between WS_2 and different metals, in order to reproducibly obtain stable Ohmic contacts.

Within the scope of this work, the most relevant parameters like doping, substrate preparation, type and geometry of the metal contacts, and the thicknesses of the WS_2 flakes were varied with the aim of optimizing the electrical contact properties.

4.1 Doping

For a suitable comparison, it is convenient to describe the measurement of WS_2 with gold contacts.

4.1.1 Reference measurement with gold contacts

As previously described, a WS_2 single crystal was exfoliated onto a Si/SiO_2substrate, , which was pre-treated with oxygen plasma for 10 min to remove surface contaminations. The bulk crystals were purchased from the company *2D semiconductors*. As a reference, a linear array of gold contacts was deposited, since gold has little interaction with the TMDC. The electrical measurements were carried out with a Keithley 2400 to apply a fixed drain-source voltage Vds between two adjacent contacts, while the back-gate voltage V_g was varied between -60 to 60 V.

The current between drain and source was found to be $i_{ds} \sim 3-7nA$ at $V_{drain-source} = -5V$ and $V_{gate} = 60V$, largely independent of the flake thickness (between 3 and 8 layers). These currents are much lower than those previously reported ($i_{ds} \sim 10\mu A$ [46] under similar bias)and do not allow for reliable device characterization. In order to get better results, other contact metals and also chemical doping of the WS_2 sheets were tested.

4.1.2 Different metals and Argon Plasma

As alternative contact metals, titanium, cobalt, chromium and permalloy (a nickel/iron magnetic alloy, with about 80% nickel and 20% iron content) were chosen. Approximately 5 nm of these metals, which should be sufficient to form a continuous layer, were evaporated onto the flakes, and then 55-60 nm of gold were added on top. As apparent from fig. 2.19(c), the work functions of Au, Ti, Cr , Co and permalloy are low enough to help reduce the Schottky barrier, according to the Schottky-Mott rule represented by eq. 2.36 (see table 4.1).

Table 4.1: Vacuum work functions of the metals used as contacts on WS_2. These values need to be considered in the Schottky-Mott rule comparing these with the electron affinity of WS_2. Values reported by [58] and [59].

contact material	work function
Gold	5.47 eV
Titanium	4.33 eV
Permalloy	4.8 eV
Cobalt	5.0 eV
Chromium	4.5 eV

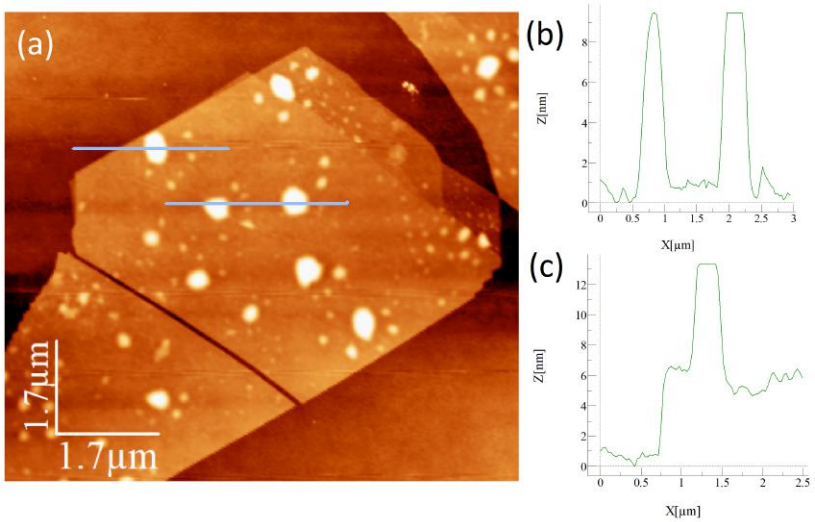

Figure 4.1: *(a) Topographic AFM image of a WS_2 flake mechanically exfoliated onto a silicon substrate. Many residuals are visible on the surface, which may prevent the metal contact from sticking to the surface. (b,c) Section profiles along the upper and the lower line in (a), respectively. These yield the height of the flake ($\simeq 5-6nm$) and of the residuals ($\simeq 10nm$) .*

Considering the electron affinity of 4.5 eV of WS_2 [60], titanium seems best suited for optimizing the contact interface, with a theoretically negative Schottky barrier. On the other hand, as explained before with the fig. 2.17. However, WS_2 at the same time is especially prone to Fermi level pinning. Consequently, only little differences could be observed between the different types of metal contacts. The best current that could be achieved was a few nA for $V_{drain-source} = -5V$ and $V_{gate} = 60V$.

Another possible obstacle in obtaining an Ohmic contact is related to the surface of the WS_2 which, as apparent from the AFM image in fig. 4.1, are partially covered by residuals (possibly glue from the mechanical exfoliation using the blue tape) with height of up to 10-20 nm. Since the evaporated metal tends to form clusters, the residuals likely prevent the metal contacts to stick uniformly to the TMDC surface and also create local barriers. With the aim of removing the residuals, the WS_2 flakes were cleaned by argon plasma performed within the high vacuum chamber. In order to avoid damage of the flake, the plasma time was restricted to 10 s. For flakes pre-treated in this manner, I-V curves like exemplified in fig. 4.2 were obtained. Although the current increases with increasing magnitude of the applied back-gate voltage, the maximum current reaches only $\simeq 16nA$, which is still not suitable for further measurements (especially compared to other works [46]).

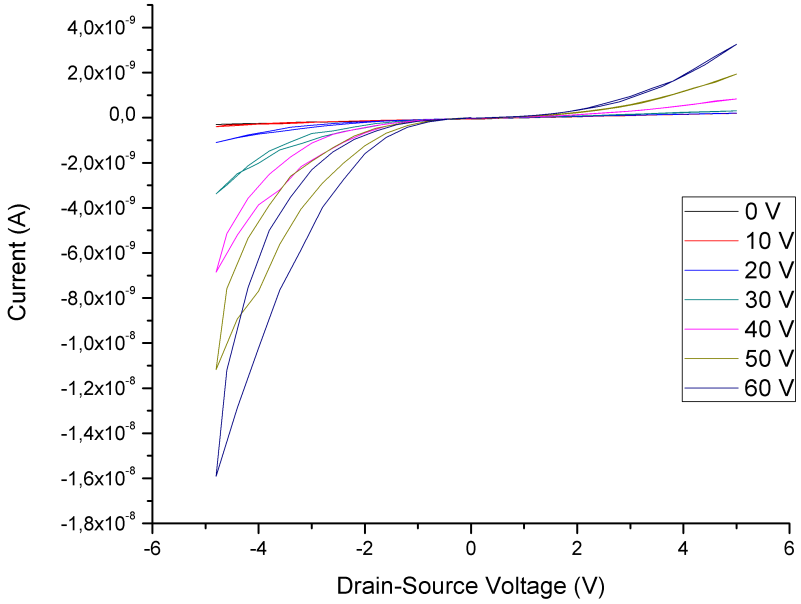

Figure 4.2: *Room temperature I-V curve acquired from a WS_2 flake whose contact regions were pre-treated by 10 s of argon plasma. The different colors denote the different applied back-gate voltages. Although the transistor can be switched on, a sizable Schottky barrier is present and the maximum current is therefore only low.*

4.1.3 Dichloroethane doping

Another possible strategy to reduce the contact resistance is to heavily dope the TMDC under the metal. This is expected to reduce the Schottky barrier width, which in turn can enhance the tunnelling current through the M-S contact. In conventional semiconductors, such doping can be achieved by dopant diffusion or ion implantation. For atomically thin TMDC sheets, by comparison, it is a challenge to precisely control the doping density with the ion implantation.

Following these considerations, the WS_2 doping could be exploited to move the Fermi energy level in the semiconductor to optimize the contact.One suitable doping agent is 1,2-dichloroethane (DCE), as previously described [62].

In the present experiments, SiO_2/Si substrates with exfoliated WS_2 flakes were immersed in undiluted DCE (99.8% pure)for 12 to 20 hrs at room temperature. Here again, thin flakes (1-4 layers) will lead to higher contact resistance. The samples were then rinsed with acetone and isopropanol, followed by e-beam lithography (see chapter 3) and evaporation of first 5 nm of chromium and finally 60 nm of gold. The maximum measured current after 20 hours of DCE doping was $\simeq 0.37nA$, which is still quite low.

Repeating the DCE doping step (20 hrs), yielded a one order of magnitude increased maximum current (3.2 nA) for some flakes, and up to $1.4 * 10^{-7} A$ in the best case.

The observed negative shift of threshold voltage indicates an enhanced electron density in the DCE-treated TMCD sheets, corresponding to an n-type doping. While the precise doping mechanism by DCE is not yet understood, it may involve replacement of S vacancy by Cl atom, whereupon the discrete impurity energy levels merge with the conduction band, thus narrowing the band gap (see fig. 4.3) [62].

Further experiments with other contact metals did not provide better results. For example, contacts made of 10 nm of titanium and 40 nm of gold gave a maximum current of 3.8 nA under the usual conditions $3.8nA$ in the usual conditions ($V_{drain-source} = -4V$ and $V_{gate} = 60V$).

Despite the limited success, the DCE doping enabled a notable improvement, which motivated testing another doping method.

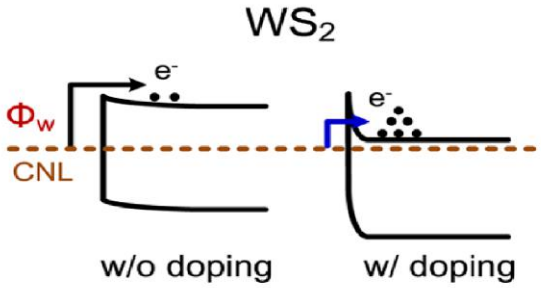

Figure 4.3: *Band structure of the a metal-WS_2 contact without and with doping. The Cl-doped WS_2 presents new discrete impurity energy levels merging with the conducting band and leading to a band gap reduction. Adapted from [62]*

4.1.4 LiF doping

LiF is a widely used n-dopant for organic semiconductors due to its strong electron-donating ability [63]. For doping of the WS_2 FET devices, the substrates were immersed in LiF solution at room temperature for 1 hour, followed by soft baking at 80°C for 2 min and blowing dry underN_2. The doping solution consisted of 0.01 M LiF ($\geq$ 99.9%) in deionized water, dissolved by stirring at 80°C for 5 min [63]. The metal contacts on the WS_2 consisted of 5 nm of chromium and 55 nm of gold.

Doping by LiF (before or after defining the electrical contacts) gave even better results than the DCE doping. In particular, LiF doping after the contact deposition revealed to be the most effective. This may be due to the LiF residues left on the flake, since these could constitute a barrier between the contacts and the flake which prevents the current from flowing. The results of the different tests are summarized in table 4.2.

It is apparent that the LiF doping has improved the currents by three orders of magnitude, especially when doing the procedure after the contacts evaporation. This may indicate that the WS_2 has low intrinsic charge carrier concentration and that the residuals prevent the contact from sticking to the WS_2 surface, blocking the current flow. These hypotheses will be clarified within the next section.

Annealing for 1 hr at 200°C resulted in a good improvement on the sample, as further confirmed in the next section 4.2.3.

4.1.5 Silanization

As explained in section 3.1, the silicon substrate are cleaned by rinsing with N-ethyl-2-pyrrolidon (NEP), acetone and isopropanol. This procedure may still leave some residuals, which might interfere with the exfoliation and the electrical measurements of the WS_2 flakes. For this reason, oxygen plasma was applied in addition, in order to clean the silicon surface to the maximally possible extent. However, the oxygen plasma creates many OH groups, which may interfere with the WS_2 flakes and modify the structure band and the carrier concentration. Particularly the presence of OH groups may attract some negative charges towards to SiO_2 substrate and this may reduce the charge carrier concentration, despite of the doping or the intrinsic concentration.

In order to prevent this, the silicon substrate is immersed in a 50% solution of Bis(trimethylsilyl)amine, also known as hexamethyldisilazane or HMDS, in chloroform for 30 minutes on a hotplate (40°C). Then the substrate is rinsed with isopropyl alcohol (or IPA) and blown dry with Argon. HDMS is an organosilicon compound with the chemical formula $[(CH_3)_3Si]_2NH$. It can transfer trimethylsilyl groups to the OH groups on the silicon surface, thus eliminating negatively charged Si-O^- groups on the surface.

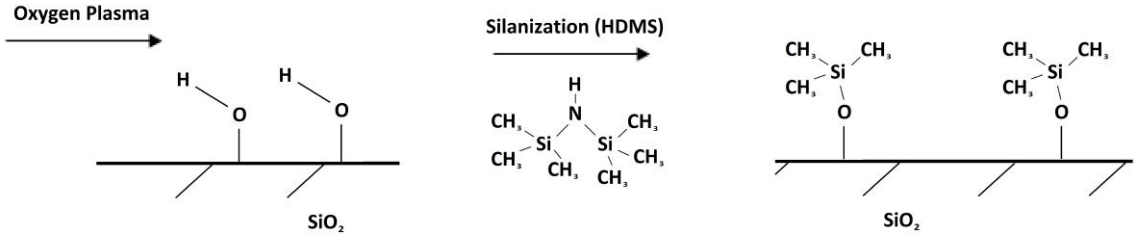

Figure 4.4: *Oxygen plasma-induced creation of OH groups on a silicon substrate, and chemical reaction between these and HDMS. Further reactions may occur to form an uniform layer as described in [47].*

It proved difficult to investigate the silanized substrates by AFM due to considerable electrostatic interactions between the substrate surface and the AFM tip. Hence, the flake thickness could not be accurately determined.

Silanization was also combined with the previously described LiF doping process (third entry in table 4.2. As the major result, the silanization contributes only little to

Table 4.2: *Maximum currents measured after LiF doping, performed before or after evaporating the contacts (comprising 5 nm of chromium and 55 nm of Gold). When doping was performed before and after contact deposition on the same sample, the final result is provided in the doping after evaporation column. 1 M concentration corresponds to 1 mol/l.*

Oxygen Plasma	LiF molar concentration	silanization	doping before evaporation	doping after evaporation	notes
10 min	0.01 M	NO		up to 8 μA	annealing 1h at 200°C
10 min	0.01 M	NO	few nA	few nA	
10 min	0.05 M	YES		few nA	slightly turning on
2 min	0.1 M	NO		$0.7 - 6\ \mu A$	

the improved conductivity, indicating that the surface OH groups do not significantly impede the current flow through the flakes.

4.1.6 Thickness of the flakes

Another important parameter is the thickness of the flakes to be contacted. As noted before (section 2.3.2), WS_2 displays broken spatial inversion symmetry and associated high valley polarization not only for the monolayer case, but even for few layers.

This is the reason why for this thesis, flakes with a thickness of 3.5 to 6 nm (5-9 layers) were selected, as they are easier to contact and at the same time still show the desired physical properties. A few thinner flakes (3 nm) were also included, but they did not yield high and stable currents like the thicker ones.

From the device point of view, the thinner flakes (1-4 layers) have the following three disadvantages [62]:

1. the larger band gap increases the Schottky barrier
2. less charge screening leads to a reduced mobility compared to the bulk
3. the charge density of the channel decreases, which limits the saturation drain current.

As mentioned before (section 2.8), another major complication in case of the thinnest flakes is the (partial) degradation of the layers in proximity to the contact metal.

As a result, both the channel resistance and the contact resistance become larger when a thinner flake is used as the channel. The main disadvantage of the thick flakes (>8 layers) is the difficulty to influence the heavily doped layer at the top of the flake (which is farthest away from bottom gate)[62].

t

Table 4.3: *Summary of the maximum currents (detected with $V_{drain-source} = -5V$ and $V_{backgate} = 60V$, unless otherwise specified) observed for Re-doped WS_2 flakes (supplied by 2Dsemiconductors) using different contact metals.*

Contacts	Maximum measured current	Notes
Au (50 nm)	$25 \div 80\ \mu A$	5 nm flake
Ti (5 nm) + Au (50 nm)	$2 \div 5\ nA$	
Cr (5 nm) + Au (55 nm)	$\sim 1\ \mu A$	
Co (50 nm) + Au (30 nm)	$\sim 0.7 \div 2.5\ \mu A$	measured with $V_{ds} = -4\ V$ and $V_g = 50\ V$

4.2 N-type WS_2

Motivated by the positive results of the chemical doping, also intrinsically doped WS_2 sheets were studied. To this end, n-doped WS_2 was purchased from the company $2D - semiconductors$. This material is doped by rhenium (Re) with a concentration in the range of 10^{17} - $5 * 10^{18}$ $\frac{atoms}{cm^3}$. The atomic configuration of Re is $[Xe]\ 4f^{14}\ 5d^5\ 6s^2$, its electron affinity is 14.5 kJ/mol and its first ionization energy is 755.82 kJ/mol [48] [49].

For comparison with previous result, devices with gold contacts were first fabricated. They yielded a maximum current of $\simeq 20 - 80\mu A$ (at $V_{ds} = -5V$ and $V_g = 60V$) for different flakes.

with a thickness of approximately 5 nm. Subsequently, also other contact metals were tested, with the results summarized in table 4.3. It should be mentioned that for every substrate 4 or 5 flakes were contacted and measured, but usually only few contacts were working and even fewer were reaching the maximum current specified.

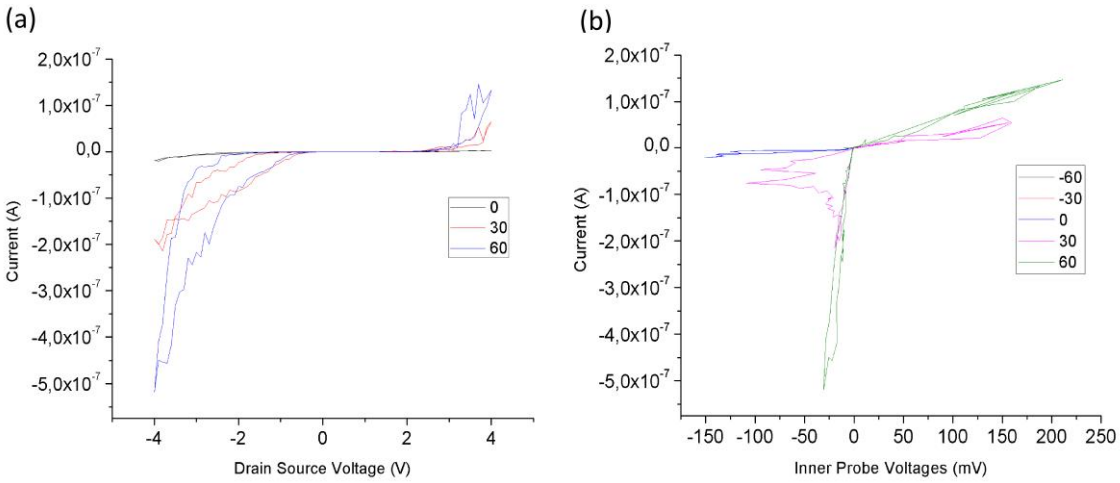

Figure 4.5: *Room temperature electrical characterisation of a Re-doped WS_2 sheet with Co/Au (50/30 nm) contacts. (a) I-V curves obtained in 2-probe configuration (current measured between two adjacent contacts). The colors code different back-gate voltages. (b) I-V curves acquired from the same sheet in 4-probe configuration (current injected from the two outer electrodes, and voltage detected between the two inner electrodes). The colors again code different back-gate voltages.*

The n-doped WS_2 sheets show quite high currents in 2-probe configuration (fig. 4.5 (a)). Further measurements in 4-probe configuration, shown in fig. 4.5(b), unexpectedly gave only non-linear I/V curves. From their approximately linear sections, one can estimate a channel resistance on the order of $400k\Omega \div 10M\Omega$.

However, due to the unusual loop-like characteristic, these values have to be taken with care. In order to avoid such problems, a different contact configuration was investigated, as described in the following section.

4.2.1 Van der Pauw measurements

While promising results could be obtained on WS2 sheets in two-probe configuration, more elaborate charge transport experiments e.g. under magnetic field require reliable measurements in 4-probe configuration. The non-linear curves obtained in the 4-probe measurements using a linear electrode array (see previous section) indicate issues with the contact resistance (e.g., an unusual bias dependence). This may be explainable by a chemical reaction between the contact metal and the WS2, which deteriorates the crystalline periodicity and modifies the band structure of the TMDC, thus creating a local Schottky barrier. As described in section 2.8, such reaction has been documented for the interface between titanium and MoS_2 [30], and may likewise occur between WS2 and the metal atoms arriving from the gas phase [43] (see fig. 5.1).

As a workaround, devices in van der Pauw geometry were fabricated. This configuration offers the advantages that (i) the contact area can be reduced, and (ii) that the

voltage probes are located at the sample edges (see fig. 4.7(a)) rather than extending across the entire sheet width. As described in section 3.6, the channel resistance is calculated from the current flowing within the flake between two neighbouring contacts and the voltage drop induced between the two remaining contacts.

The van der Pauw configuration was first realized with four cobalt contacts (Co/Au, 50/25 nm). For these devices, only few nA could be detected. By contrast, when the electrodes were replaced by Cr/Au (5/50 nm), a maximum current of $7\mu A$ was obtained (fig. 4.6). In this case, although the 2-probe measurements were not perfectly linear (fig. 4.6 (a)), 4-probe measurements could be performed at least on some flakes (fig. 4.6 (b)). In the latter case, linear curve fits (in the low bias regime) yield a channel resistance value of between 5 and 150 kΩ, depending on the flake and the detailed contact configuration.

Compared to the Cr/Au contacts, better results were obtained with pure gold contacts gave better results, as apparent from the close-to-Ohmic contact behaviour (see fig.4.7(d)). However, such I-V curves were observed only for some flakes, while others on the same substrate displayed non-linear I-V curves, which also exhibited unusual loop-like characteristics (again a signature of unstable contacts properties). This hints toward the presence of (e.g., glue or PMMA) residuals on the flakes which reduce the quality of the WS_2 – gold interface.

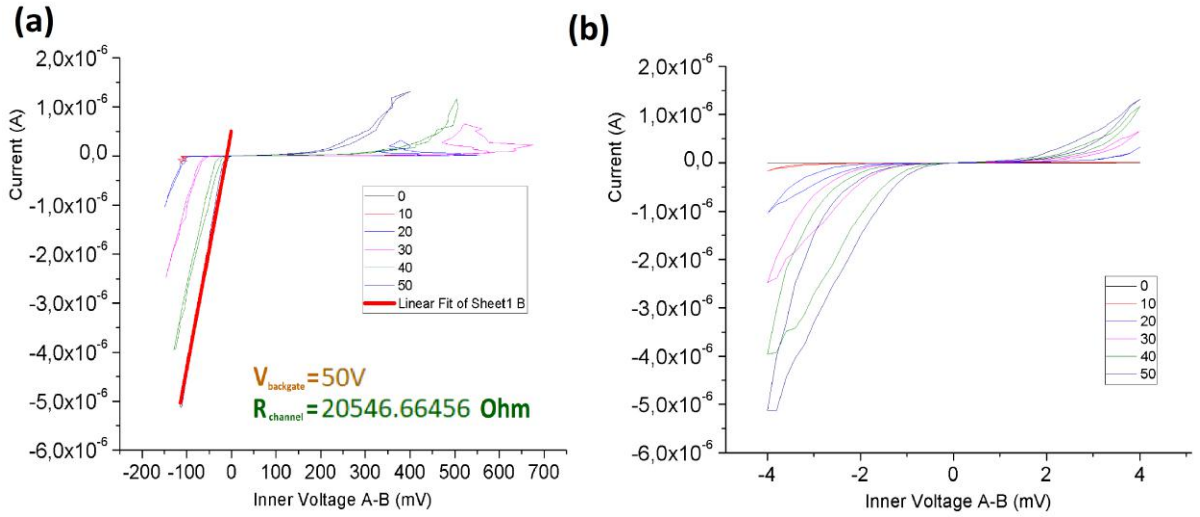

Figure 4.6: *Results of electrical measurements on a few layer WS_2 sheet with Cr/Au contacts in van der Pauw geometry. (a) A notable maximum current is observed in the 2-probe measurements, although the hysteresis indicates capacitive effects at the contact interface. (b) In 4-probe configuration, a linear curve occurs only for negative drain-source voltage, where the current is higher. However, there is an unexpected offset, indicating that the contacts are non-ideal.*

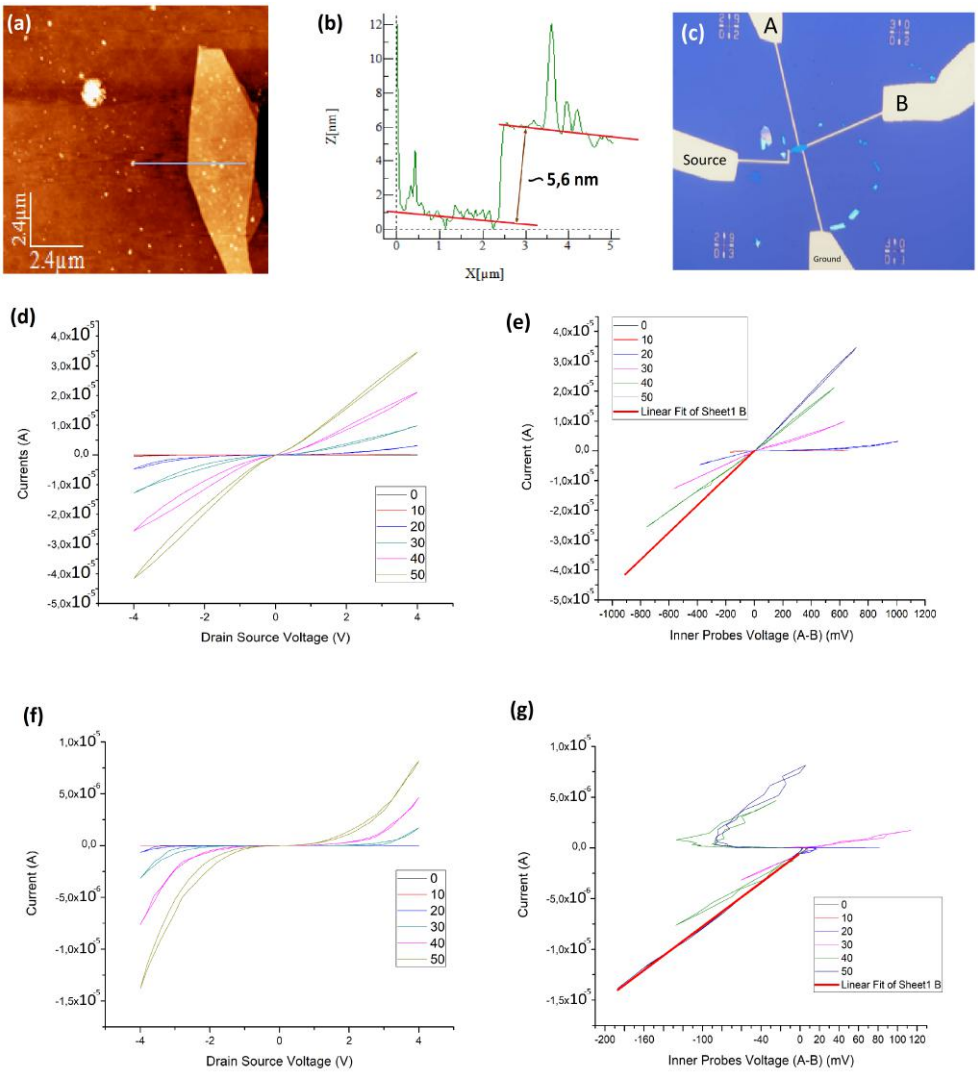

Figure 4.7: *Electrical behaviour of a few layer WS2 flake with gold contacts (room temperature). (a) Topographic AFM image of the used flake. (b) AFM height profile along the horizontal line in (a). The height of the flake is* $\simeq 5.6$ *nm, corresponding to 8 layers. (c) Optical image of the flake with four contacts in van der Pauw geometry. (d,f) Results of 2-probe measurements performed at room temperature (300 K) and 1.4 K, respectively. (e,g) Results of 4-probe measurements at room temperature (300 K) and 1.4 K, respectively. The plot in (g) clearly displays an S-shape. The different colors denote different gate voltages.*

Comparison between fig.4.6 and fig.4.7 reveals that the Au contacts are associated with a lower Schottky barrier than the Cr/Au contacts. This difference could be due to the higher work function of gold, although this may not exclude Fermi level pinning also in this case (see the section 2.8). Another possible reason may be a lower chemical reactivity between the gold contacts and the WS_2.

It should be emphasized that while the 4-probe measurements can yield close-to-linear I-V curves, in many cases unexpected behaviours were observed, in particular offsets at low currents. The latter may arise from capacitive effects on the contact interface.

4.2.2 Low Temperature Measurements

Since the gold contacts showed good results, the same sample was electrically characterized also at low temperature, including the application of a magnetic field. As shown in fig. 4.8, the electrical behaviour at low temperature is quite different from that at room temperature. Specifically, the 2-probe measurements yield a lower conductivity as a consequence of the lowered charge carrier concentration at low temperature.

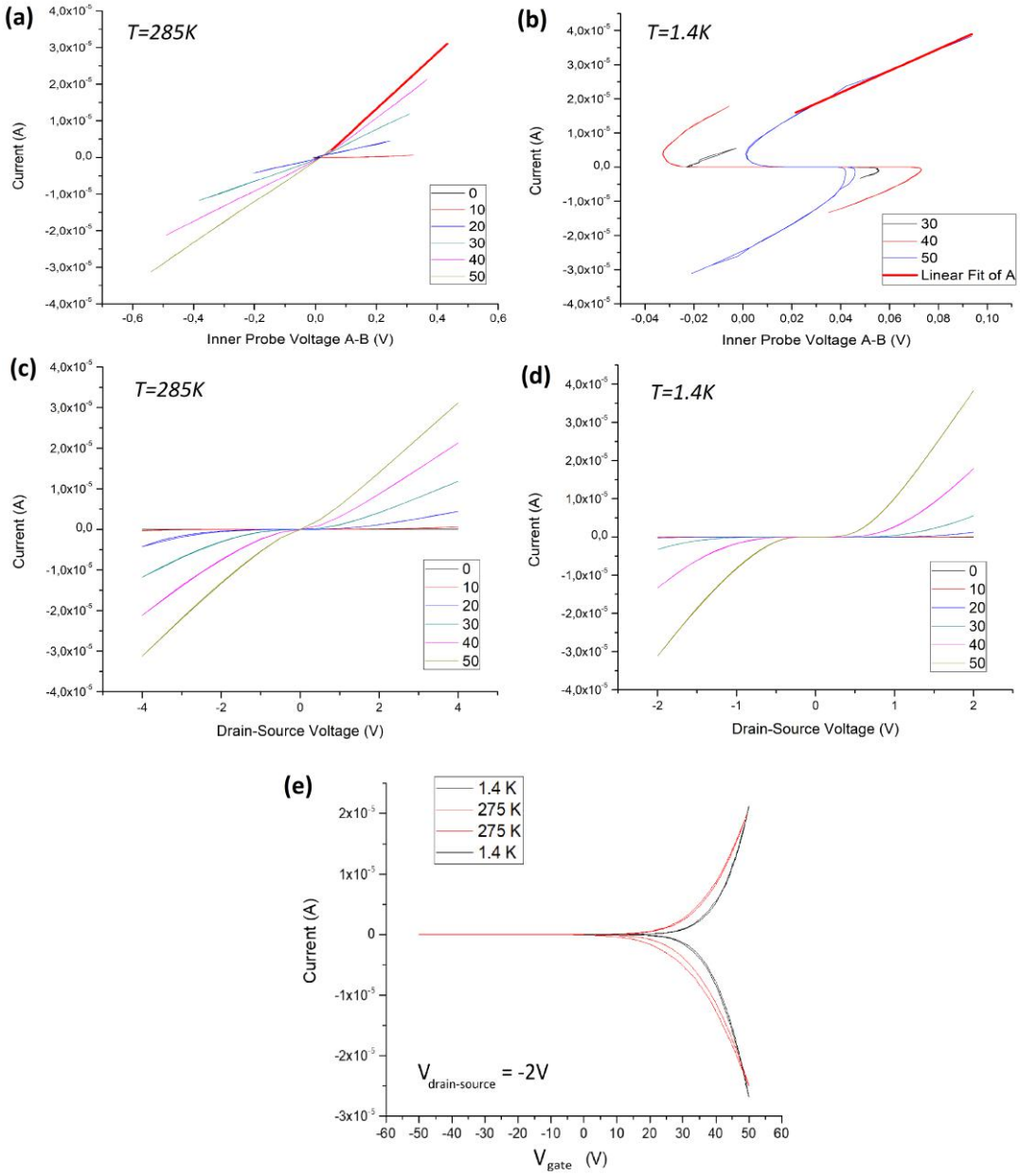

Figure 4.8: *Electrical characterisation of a few layer WS_2 sheet at two different temperatures. (a,b) I-V curves obtained at the indicated temperatures by 4-probe measurements, using the inner voltage probes (A-B) to detect the potential drop. The red lines have been used for the fits to estimate the sheet resistance. The different colors denote the different gate voltages. The S-shape observed at low temperature is a common characteristic for all these measurements, irrespective of the flake or the configuration. (c,d) I-V curves obtained by 2-probe measurements at the indicated temperatures. (e) Current recorded at $V_{ds} = -2V$ while varying the back-gate voltage V_{gate}. The FET channel is in the off-state for negative gate voltages.*

Moreover, according to other previous studies like [46], the $I - V_{ds}$ curves recorded at the two different temperatures with $V_g = 50V$ intersect each other at $V_{ds} = 0.7V$. After that value of the drain-source voltage, the current at low temperature is higher, probably due to the higher mobility at lower temperature. This may represent a signal of a good contact obtained onto WS_2 sheets. For this reason, the drain-source voltage have been swept from -2V to 2V, in order to limit the current flowing in the flake and to prevent the flake from breakup.

In case of the 4-probe measurements, for every flake and electrode configuration, an *S-shape* was observed at low-temperature. This unusual behaviour shows that for very low currents, the potential drop between the voltage probes (on the opposite side of drain and source) is inverted. This finding again signifies the unstable contact properties, which in addition depend on temperature. In the next section, one approach to solve the issue will be described.

4.2.3 Annealing

Annealing has proven useful to improve the electrical contacts on WS_2 [46]. It is assumed that the annealing removes the residuals or impurities at the metal-WS_2 interface, thereby rendering the latter more transparent for the current flow. In the present experiments, the samples were annealed for 2 hrs in forming gas (a mixture of 10% of H_2 and 90% of N_2) at 200°C, and then immediately electrically characterized. This process notably improved the conductivity, as can be seen from fig. 4.9(d) and (e). Specifically, the annealed device shows a more linear I-V curve and a slightly higher current, in close agreement with previous studies [46].

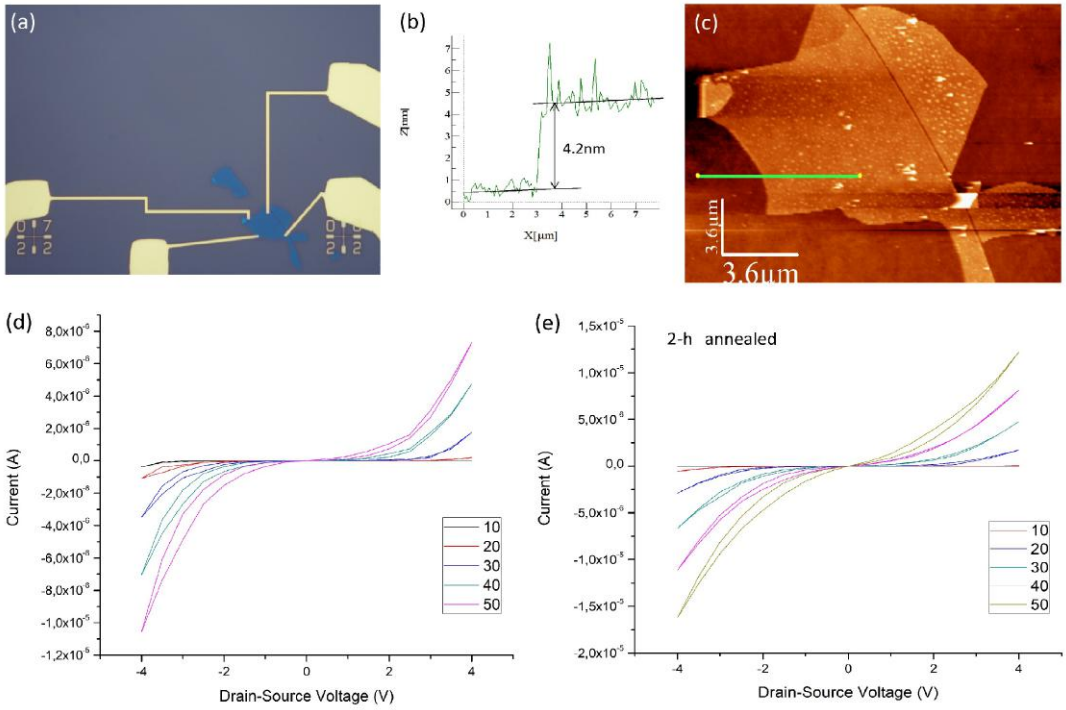

Figure 4.9: *Electrical characterisation of the annealed WS_2 sample with gold contacts. (a) Optical image of the flake used for the measurements. (c) Topographic AFM image of the flake. (b) Height profile along the green line in (c). The thickness of the flake is $\simeq 4.2$ nm, corresponding to 6 layers. (d,e) 2-probe I-V curves obtained at room temperature before (d) and after (e) annealing of the device. After annealing, the curves display a larger current. The colors denote the applied gate voltages.*

Based upon the above data, the charge carrier concentration and mobility can be derived. The latter is accessible via the following equation:

$$\mu = \frac{dI_{ds}}{dV_{bg}} * \frac{L}{W * C_i * V_{ds}} = 3.72 \frac{cm^2}{V * s} \tag{4.1}$$

where W is the width of the WS_2 flake (6.2 μm), and L is the channel length, i.e. the distance between the inner voltage probes (4.58 μm). The capacitance C_i between the channel and the back-gate per unit area can be estimated as

$$\epsilon_0 * \frac{\epsilon_r}{d} = 1.15 * 10^{-4} \frac{F}{m^2}$$

with the vacuum permeability, $\epsilon_0 = 8.85 * 10^{-12} \frac{F}{m}$, the relative permeability of the SiO_2, $\epsilon_r = 3.9$ and d as the thickness of the silicon oxide layer (300nm). Comparison with previous investigations shows that the obtained mobility of a few $\frac{cm^2}{Vs}$ falls into a reasonable range [46].

The resistivity can be calculated as

$$\rho = R_{channel} * W * \frac{t}{L} = 1.95 * 10^{-5} \Omega m \tag{4.2}$$

where t is its thickness of the flake (4 nm), and L is the channel length (see above). Finally, the charge carrier concentration can be obtained from:

$$\sigma = n * e * \mu \tag{4.3}$$

$$n = \frac{\sigma}{e * \mu} = \frac{1}{\rho * e * \mu} = 8.611 * 10^{26} m^{-3} = 8.611 * 10^{20} cm^{-3} \tag{4.4}$$

This value is significantly larger than expected. In fact, the dopant concentration is documented to be between $10^{17} \div 10^{18} cm^{-3}$ [66]. Further studies are thus required to confirm and clarify this result.

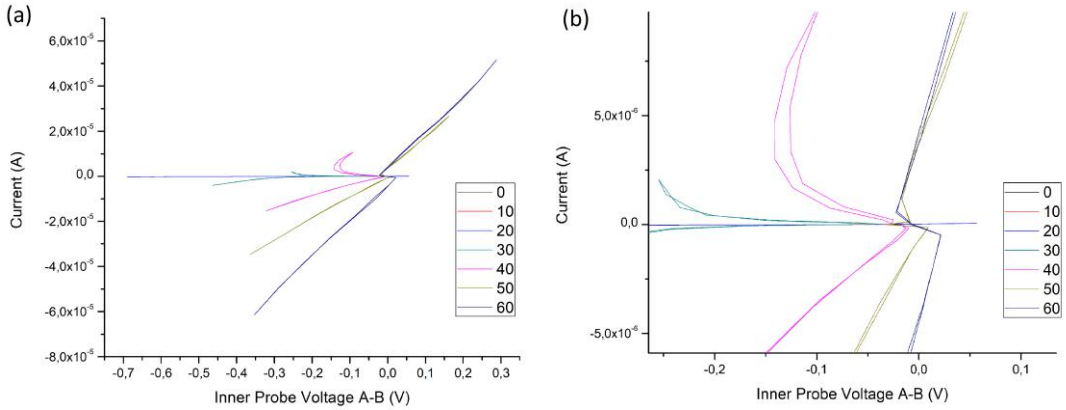

Figure 4.10: *4-probe I-V curves recorded at 1.4 K. The "S-shape" can be identified in graph (a) and (b). The figure (b) is the enlarged copy of (a) for low current values. The different colors correspond to different gate voltage values.*

Moreover, when the device is cooled down, the measured I-V curves again display the S-shape (fig. 4.10(a)(b)). It is noticed that the voltage detected between the inner probes gets inverted, and that this inversion is stronger for smaller gate voltages, when the depletion region is thinner. This phenomenon was observed on every flake at low temperature, even with different contacts (as previously discussed), whereas it is entirely absent at room temperature. One possible explanation could be related to the mean free path, with ballistic transport occurring along the flake diagonal, thereby inverting the potential drop between the voltage probes. However, according to recent studies on TMDCs [50], the mean free path is only few tens of nm, much shorter than the contact distance of approximately $\sim 1 \mu m$. Even though at low temperature the mean free path should become longer, it is unlikely to approach the μm range. It rather seems

that upon cooling, the metal-WS2 interface changes its band profile, whereby an electric field-dependent tunnelling characteristic emerges. The underlying mechanism of this change, however, remains to be clarified.

On the other hand, once the sample is heated up, the contacts work the same as before cooling them down.

4.2.4 Measurements under Magnetic Field

Despite their general "S-shape", the I-V curves in fig. 4.10 are close-to-linear when a back-gate voltage of 60 V is applied. Therefore, using this gate voltage, the device was further electrically characterized under an externally applied magnetic field, which was varied from -8 to 8 T.

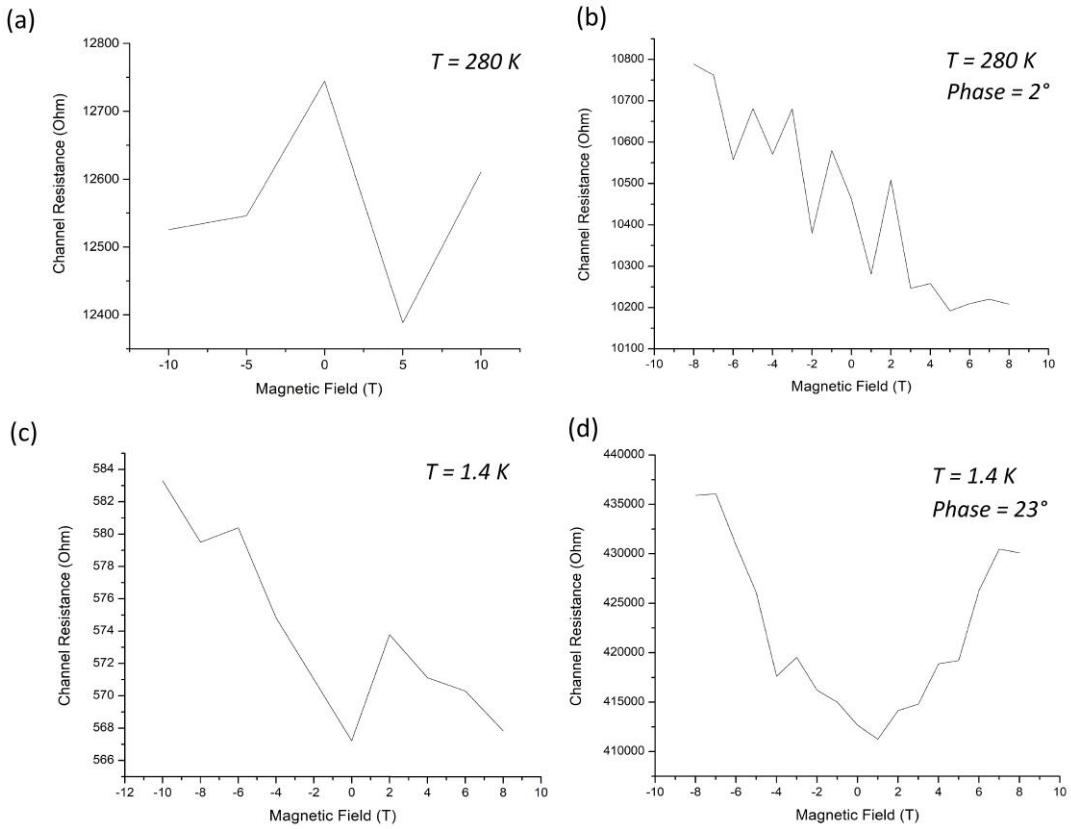

Figure 4.11: *Results of van der Pauw measurements on a WS_2 sheet, performed in DC or AC mode. (a,b) Plot of resistance vs. B-field, measured close to room temperature in DC (a) and AC (b) mode, respectively. (c,d) Plot of resistance vs. B-field, acquired in DC (c) and AC (d) mode at 1.4 K, respectively.*

The results from van der Pauw measurements close to room temperature in DC mode are shown in fig. 4.11 (a). The calculated channel resistance is about 12 $k\Omega$.

Since the two valleys of the valence band are not split or excited by circularly polarized light, they are equally populated and the total magnetic moment is zero (see eq. 2.9). On the other hand, the anisotropic magnetization is not recognizable in van der Pauw measurements in DC mode and the resistance is varying in a narrow range, relatively to the magnetic field.

AC measurements

In addition, the resistance of the WS_2 flake was also measured in AC mode. To this end, the lock-in amplifier (see section 3.5.2) was used.

After adjusting the phase synchronization of the AC signal applied to source and drain, the induced current and the potential difference between the inner voltage probes were used to determine the channel resistance. These measurements were carried out as a function of applied magnetic field. As apparent from fig. 4.11 (b), the AC measurements close to room temperature the results are in reasonable agreement with the DC ones. However, at low temperatures the AC data in general displayed a much higher resistance, and a phase shift between the induced voltage and the A-B voltage of more than 23°. These observations point toward capacitive effects at the contact interface, which are likely to obscure the actual channel resistance.

Furthermore, the Hall measurements performed in AC mode at room temperature show a linear curve that signifies p-type character of the FET channel, as apparent from the positive slope of the Hall resistance vs. B-field plot in fig. 4.12(a). A magnetic field applied perpendicular to the substrate plane causes the holes to deviate toward the A contact through the Lorentz force:

$$\mathbf{F_L} = q\mathbf{v} \times \mathbf{B} \tag{4.5}$$

where q is the charge of the holes and $\mathbf{v}$ is the velocity. Thus, with increasing B-field, more holes move to contact A, thus leading to a larger voltage drop $V_A - V_B$ and correspondingly a larger Hall resistance.

By contrast, the DC measurements have shown increased currents for positive voltages (see fig. 4.8(e)), suggesting that the channel is n-type.

Clearly, the contradictory conclusions from the Hall and gate dependent measurements require further clarification. The large phase difference (117°) observed between the input and output signals in the AC Hall measurements,suggests that the corresponding data should be considered with care. In any case, these complications once more underscore the need to further optimize the electrical contacts on the WS_2 sheets.

Moreover, the charge carrier concentration and mobility was extracted from the Hall data and compared to the values gained from the DC measurements (see eq. 4.4).

Specifically, the Hall voltage, based upon the balance between the two forces acting on the charge carriers, i.e., the electric field in the sample and the Lorentz force, is

obtained as:

$$V_H = \frac{IB}{qnt} \tag{4.6}$$

where I is the current through the flake, B the applied magnetic field, q is the charge of the single carrier (i.e., the electron charge), n is their carrier concentration and t is the thickness of the sample. It follows that the carrier concentration can be calculated from the slope of the Hall curve according to

$$n = \left(\frac{\partial (V_H/I)}{\partial B} qt \right)^{-1} = 3,054 * 10^{24} m^{-3} = 3,054 * 10^{18} cm^{-3} \tag{4.7}$$

This value is in reasonable agreement with the WS_2 producer report [66]. Furthermore, the mobility is obtained by inverting eq. 4.4, in combination with the resistivity gained from the van der Pauw measurements in AC mode on the same flake (eq. 4.2):

$$\mu = \frac{1}{\rho \cdot e \cdot n} = 0,08793 \frac{m^2}{Vs} = 878,93 \frac{cm^2}{Vs} \tag{4.8}$$

The comparison with previously reported mobility values for WS_2 sheets, which are on the order of tens of cm^2/Vs(see fig. 4.12 (c)) shows that the present mobility is approximately one order of magnitude larger. Here again, due to the problems with the contact interface, the mobility obtained from the DC measurements (see section 4.2.3) should be considered as more reliable. But it should be kept in mind that also in the DC case, upon cooling the contact properties are significantly changing, possibly due to mechanical strain resulting from the different thermal expansion coefficients of the contact metal and the WS_2 (although warming again up to room temperature restores the original device behavior).

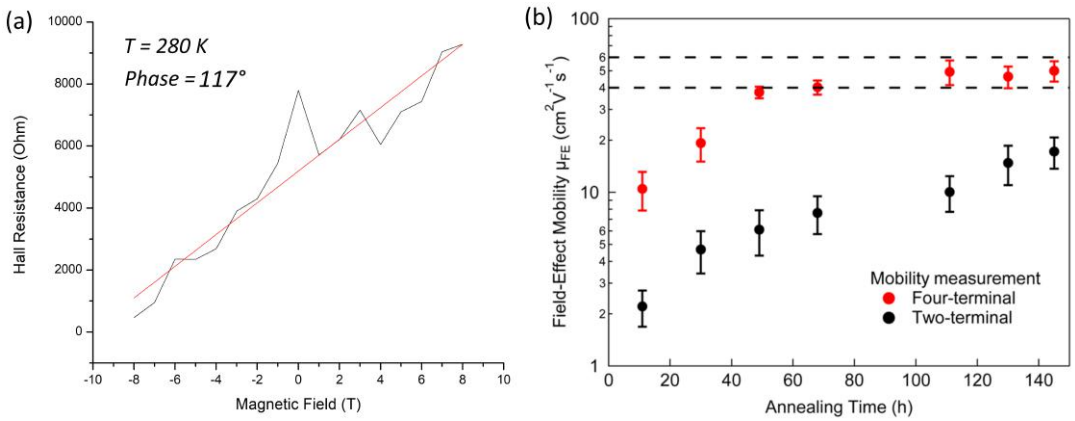

Figure 4.12: *Results of the Hall measurements in AC mode at different temperatures. (a) Data obtained at room temperature. The red line is a linear fit, used calculate the carrier concentration. There is a sizeable phase shift between the two detected signals. (b) Literature values for comparison with the present results. The plot shows the field-effect mobility of a single-layer WS_2 sheet as a function of annealing time of the device. Red data points: four-terminal mobility, black data points: two-terminal mobility. Panel (b) is adapted from [46].*

As mentioned at the beginning of the chapter, many studies have been performed with the aim of optimizing the contact interface to TMDCs [30], [40],[43],[44]. The main objective of the present experiments was to achieve contacts of similar quality as the best one reported in the literature. This task has been reached with respect to electrical measurements at room temperature, whereas for reliable measurements at low temperature, the contacts still need to be further improved.

4.3 WS_2 transfer onto $RuCl_3$

The ultimate aim of this thesis work would have been to fabricate and investigate a van der Waals heterostructure composed of WS_2 and $RuCl_3$, the latter of which is a magnetic insulator below 100 K. Such type of heterostructure, as described in section 2.7, is of interest for increasing the valley splitting in WS_2 through the magnetic exchange field (MEF). The first fabrication step consists of mechanically exfoliating WS_2 onto a PDMS layer. This step poses a great challenge due to the limited adhesion of the WS_2 on the PDMS, and the difficulty to optically identify the thinnest flakes on the PDMS. The identifiable flakes have a thickness around 5-6 nm, which is the lower limit to achieve a significant conductivity.

Another option is to follow the usual procedure to exfoliate WS_2 onto the silicon substrate and then to pick up selected flakes by the PDMS using the micromanipulator (fig. 4.13). However, despite several attempts performed at different temperatures, such pick-up was not possible without mechanically breaking the flake.

By comparison, mechanical exfoliation of $RuCl_3$ onto the Si/SiO_2 substrates is easier to achieve than for WS_2, but the magnetic exchange field is significantly easier to induce for ten layers of the material. Therefore this is the thickness, chosen to be used in this project.

After obtaining the exfoliated WS_2 on PDMS (fig. 4.13(f)) and $RuCl_3$ on the silicon substrate, the transfer was performed by the micromanipulator which allows to align the two flakes and to position the WS_2 on top of the $RuCl_3$. The next step consists of heating the substrate up to 70-80 °C, while keeping the PDMS attached to it. This process weakens the adhesion of the WS_2 flake on the PDMS, thus facilitating its transfer onto the $RuCl_3$ on the substrate.

15 minutes after reaching the temperature, the substrate is cooled down in order to make the PDMS retract from the WS_2 and, when the sample has reached room temperature, the PDMS and the substrate can be slowly separated.

This procedure provided the best results, even though the PDMS leaves a sizeable density of residues on the WS_2 flake (see fig. 4.13(a)). Therefore, the substrate needs to be annealed at 200 ∘C for 2 hours, after which its surface looks more clean (fig. 4.13(d)).

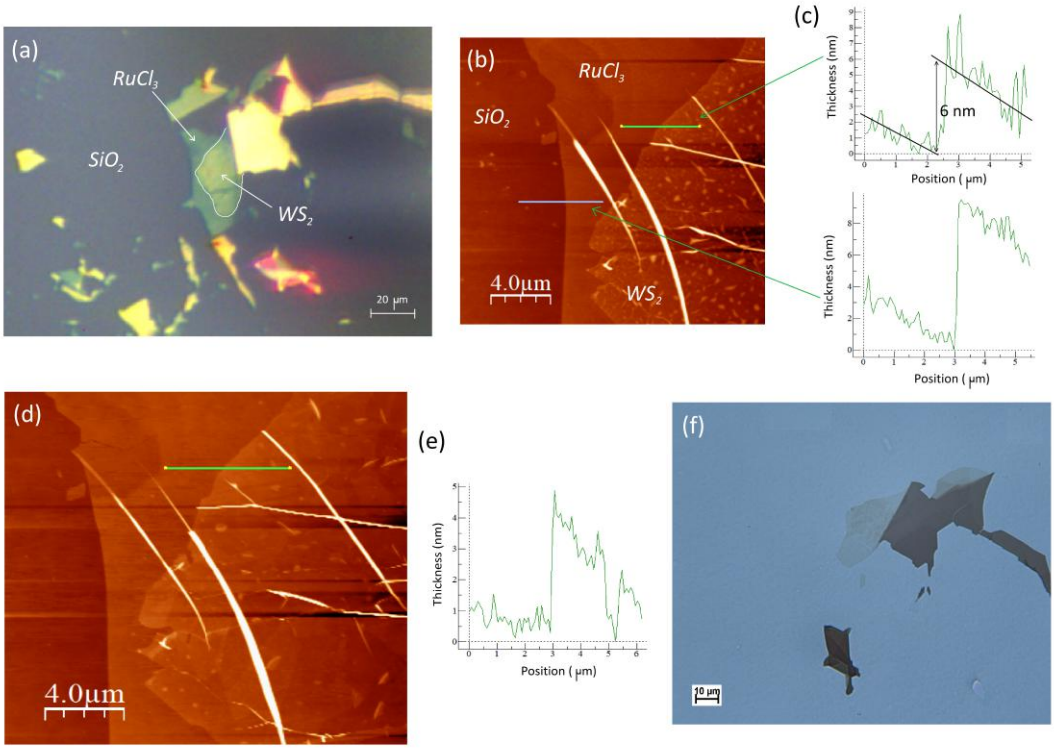

Figure 4.13: *Fabrication of a $WS_2/RuCl_3$ heterostructure via mechanical transfer using a micromanipulator. (a) Optical and (b) topographic AFM image of a fabricated heterostructure. (c) AFM section profiles along the two horizontal lines in (b). (d) Topographic AFM image and relative section profile (e) of the same heterostructure after 2-hours annealing. The sheets can be noted to be more uniform and flat. (f) Optical image of the exfoliated WS_2 on top of the PDMS, before the transfer onto the $RuCl_3$.*

5 Summary and Outlook

The significant recent advances in the fields of spintronics and valleytronics have been enabled by the improved understanding and control of spin dynamics in novel materials. Of particular interest in this context are transition metal dichalcogenides, for which spatial inversion symmetry breaking opens up exciting opportunities towards the development of novel nanoscale valleytronic devices. In particular, TMDCs allow the transport of charge carriers with different valley indices, which may be used as another degree of freedom of electrons. Valley-specific spin-polarized currents may be excited by circularly polarized photons with the appropriate frequency. This spin-valley coupling provides access to the valley Hall effect, where electrons drift to one specific edge of the sample according to their valley index. The spin-valley coupling is enabled by the strong spin-orbit coupling in TMDCs even at room temperature. The spin-orbit coupling introduces an energy gap for different spin values (related to the valley ones) and this splitting of the valence band tops couples the valley to the spin, such that the valley optical selection rule becomes spin-dependent.

In this thesis work, the properties of metal contacts on WS2 sheets have been investigated and optimized as important prerequisites for the practical implementation of the above described phenomena. High quality electrical contacts are also important for exploring TMDC-based heterostructures which are devised to exploit interfacial effects like for instance a magnetic exchange field. As a first step in the latter direction, heterostructures made of WS_2 and the magnetic insulator $RuCl_3$ have been fabricated for the first time.

After discussing the theoretical background on TMDCs in chapter 2, and the principles of the employed experimental techniques in 3, the obtained results are summarized in chapter 4. As a major achievement, metal contacts of good quality and stability have been achieved on few layer WS_2 sheets, as documented by close-to-linear I-V characteristics obtained by 2-probe electrical measurements.

To be more specific, recollecting the results described in chapter 4, a good improve-

ment has been firstly obtained when the device have been doped with high concentration of LiF after the contact evaporation. A further improvement has then been achieved with n-type WS_2, purchased from *2Dsemiconductor* company, which has provided high currents. Finally the annealing procedure has improved the contacts making the interface between gold and WS_2 sheets more transparent and the I-V curves almost linear.

By contrast, the I-V curves obtained by 4-probe measurements commonly displayed an unexpected behaviour (especially at low temperatures) such as the emergence of an S-shape. This observation highlights the delicate nature of the TMCD-metal contact interface, whose charge transport characteristic may change as a function of temperature and/or applied bias. The complicated situation furthermore manifests itself in differences between 4-probe measurements in the AC and DC mode, which makes it difficult to extract reliable values for the carrier concentration and mobility. In fact, the resistivity of the WS_2 sheets determined in DC mode was $\sim 10^5 \Omega m$, while using the AC mode, the resistivity values between $\sim 10^2 \div 10^3 \Omega m$ were obtained, in comparison to previous studies which found values on the order of $10^2 \Omega m$ [46].

Another issue which requires further clarification is the discrepancy regarding the type of majority carriers in the WS_2 sheets. Specifically, while AC Hall measurements favoured holes as majority carriers, in the DC measurements application of a positive back-gate voltage resulted in increased conductivity, pointing toward electrons as majority carriers.

In the future, alternative approaches may be tested to further improve the quality of the contacts. One option would be to increase the annealing time (see fig. 4.12(c)) [46].

Based on the previous results and a recent work [43], another possibility would be to cool the substrate during evaporation of the contact metal, in order to minimize the damage of the topmost layers of the TMDC sheet (see fig. 5.1)

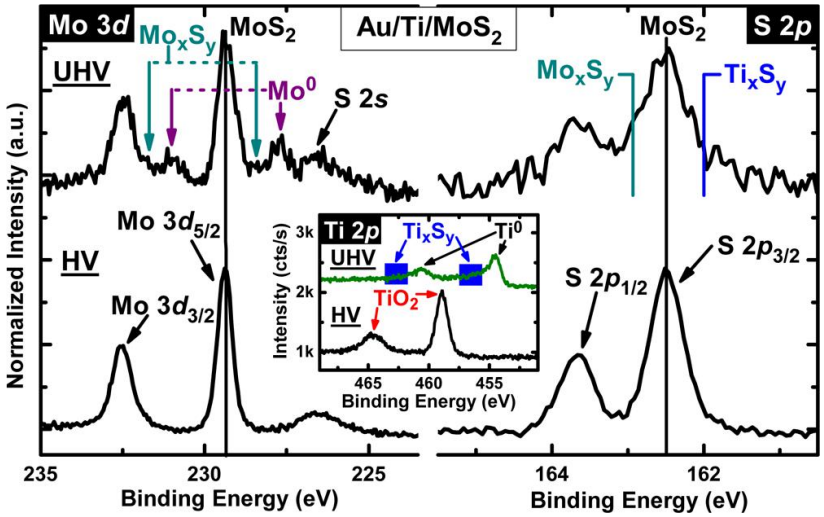

Figure 5.1: *Mo 3d, S 2p, and Ti 2p (inset) core-level spectra for Au- $Ti - MoS_2$ stacks fabricated under high vacuum (HV) and ultrahigh vacuum (UHV). In both cases, sequential depositions were performed without breaking vacuum. After deposition of the final Au layer, both samples are exposed to air for 20 min prior to XPS analysis. The Ti deposited in HV exists as TiO_2 which does not react with the MoS_2. The Ti deposited in UHV remains metallic and hence reacts with the MoS_2. Adapted from [43].*

Further microscopic analysis may be necessary to gain a better understanding of the (chemical) reaction mechanisms at the interface between WS_2 and gold, or other metals. To this end, ADF-STEM imaging like described in section 2.8 may prove useful [30].

Once the challenge of obtaining high quality contacts would have been solved, many interesting measurements could be performed. For example, the photoresponse of the WS_2 sheet could be studied under local laser illumination with a confocal microscope. When circularly polarized light is used in such experiments, valley currents could be optically pumped and then electrically detected after lateral diffusion along the WS_2. The very strong spin-orbit coupling in WS_2 renders this TMDC particularly promising for valleytronics at room temperature. By combining it with a magnetic insulator like $RuCl_3$ increased valley splitting with a high valley polarization and long valley decoherence could be achievable. The ultimate goal of such research would be an all-valley-based information processing, and in the future maybe a quantum computer based on these materials. In fact, using the valley index as a binary value may solve the important issue related to power consumption and thermal production. Other possible applications are photodetectors for polarized light, or conversely polarized light emission (electroluminescence), as a suitable basis for optoelectronic applications or quantum computer data transmission. In summary, owing to their strong spin-orbit coupling and symmetry properties, ultrathin sheets of TMDCs emerge as one of the most promising material candidates for the post silicon electronic era.

Bibliography

[1] Elías, A. L.; Perea-López, N.; Castro-Beltrán, A.; Berkdemir, A.; Lv, R.; Feng, S.; Long, A. D.; Hayashi, T.; Kim, Y. A.; Endo, M.; et al. *Controlled Synthesis and Transfer of Large-Area WS2 Sheets: From Single Layer to Few Layers*, ACS Nano 2013, 7, 5235–5242

[2] Zhu, Z. Y.; Cheng, Y. C.; Schwingenschlögl, U. *Giant Spin- Orbit-Induced Spin Splitting in Two-Dimensional Transition- Metal Dichalcogenide Semiconductors*, Phys. Rev. B 2011, 84, 153402.

[3] Di Xiao, Gui-Bin Liu, Wanxiang Feng, Xiaodong Xu, Wang Yao, *Coupled Spin and Valley Physics in Monolayers of MoS_2 and other group-VI Dichalcogenides* Physical Review Letters 108, 196802 (2012)

[4] Mark Bohr, Intel senior fellow, *14 nm Process Technology: Opening New Horizons*, Intel's presentation, 2015, https://www.intel.it/content/www/it/it/silicon-innovations/intel-14nm-technology.html

[5] Ben Sin, *Huawei's Kirin 980 Is The World's First 7-Nanometer Mobile Chipset With 5G Support* Sep 1, 2018, https://www.forbes.com/sites/bensin/2018/09/01/huaweis-kirin-980-is-the-worlds-first-7-nanometer-mobile-chipset-with-5g-support/19abb5fd175e

[6] Adam Malecek, *For first time, carbon nanotube transistors outperform silicon*, Science Advances, DOI: 10.1126/sciadv.1601240, September 2, 2016, https://phys.org/news/2016-09-carbon-nanotube-transistors-outperform-silicon.html

[7] Krishnamurthy. V., Chen. Y., Ho S.-T. *Photonic transistor design principles for switching gain >=2*, Journal of Lightwave Technology 31, 2086–2098 (2013). dx.doi.org/10.1109/JLT.2013.2262134

[8] Yamashita, Yoshiro *Organic semiconductors for organic field-effect transistors*, Science and Technology of Advanced Materials, Volume 10, 2009 - Issue 2, doi:10.1088/1468-6996/10/2/024313

[9] Ohkawa, F., Uemura, Y. *Theory of valley splitting in an N-channel (100) inversion layer of Si III. Enhancement of splittings by many-body effects* J. Phys. Soc. Jpn 43, 925-932 (1977).

[10] Sham, L., Allen, S., Kamgar, A., Tsui, D. *Valley-valley splitting in inversion layers on a high-index surface of silicon*, Phys. Rev. Lett. 40, 472-475 (1978).

[11] Xiaodong Xu,Wang Yao, Di Xiao and Tony F. Heinz *Spin and pseudospins in layered transition metal dichalcogenides* Nature Physics, 2942 (2014) DOI: 10.1038/NPHYS2942

[12] Dickinson, R. G. & Pauling, L. *The crystal structure of molybdenite.* J. Am. Chem. Soc. 45, 1466–1471 (1923).

[13] Ming-Che Chang and Qian Niu, *Berry phase, hyperorbits, and the Hofstadter spectrum: Semiclassical dynamics in magnetic Bloch bands.* Phys. Rev. B 53, 7010 (1996)

[14] Wilson, J. A. & Yoffe, A. D. *The transition metal dichalcogenides discussion and interpretation of the observed optical, electrical and structural properties.* Adv. Phys. 18, 193–335 (1969).

[15] Joensen, P., Frindt, R. F. & Morrison, S. R. *Single-layer MoS2.* Mater. Res. Bull. 21, 457–461 (1986).

[16] Tenne, R., Margulis, L., Genut, M. & Hodes, G. *Polyhedral and cylindrical structures of tungsten disulfide.* Nature 360, 444–446 (1992).

[17] A. K. Geim & K. S. Novoselov, *The rise of graphene* Nature Materials Vol. 6, 183 - 192 (2007), doi:10.1038/nmat1849

[18] Deep Jariwala, Vinod K. Sangwan, Lincoln J. Lauhon, Tobin J. Marks, and Mark C. Hersam *Emerging Device Applications for Semiconducting Two-Dimensional Transition Metal Dichalcogenides* ACS nano, DOI: 10.1021/nn500064s (2014)

[19] Podberezskaya, N. V.; Magarill, S. A.; Pervukhina, N. V.; Borisov, S. V. *Crystal Chemistry of Dichalcogenides MX2.* J. Struct. Chem. 2001, 42, 654–681.

[20] Eda, G.; Yamaguchi, H.; Voiry, D.; Fujita, T.; Chen, M.; Chhowalla, M. *Photoluminescence from Chemically Exfoliated MoS2.* Nano Lett. 2011, 11, 5111–5116.

[21] Q. H. Wang, K. Kalantar-Zadeh, A. Kis, J. N. Coleman, and M. S. Strano, *Electronics and optoelectronics of two-dimensional transition metal dichalcogenides* Nature nanotechnology, vol. 7, pp. 699-712, 2012.

[22] Di Xiao, Wang Yao, and Qian Niu *Valley-Contrasting Physics in Graphene: Magnetic Moment and Topological Transport* Physical Review Letters 99, 236809 (2007)

[23] J.A. Silva-Guillén, P. San-Jose, R.Roldàn *Electronic Band Structure of TMDCs from Ab Initio and Slater-Koster Tight-Binding Model.* Applied Sciences, 2016

[24] A. Kuc, N. Zibouche, and T. Heine, *Influence of quantum confinement on the electronic structure of the transition metal sulfide TS2* Phys. Rev. B 83, 245213

[25] Hualing Zeng, Gui-Bin Liu, Junfeng Dai, et altera, *Optical signature of symmetry variations and spin-valley coupling in atomically thin tungsten dichalcogenides* Nature Scientific Reports 3, 1608 (2013), DOI: 10.1038/srep01608

[26] L.F. Mattheiss, *Band Structures of Transition-Metal-Dichalcogenide Layer Compounds*, Phys Rev. B 8, 3719 (1973)

[27] C. L. Kane and E. J. Mele, *Quantum Spin Hall effect in Graphene* Physical Review Letters 95, 226801 (2005)

[28] Ashwin Ramasubramaniam, *Large excitonic effects in monolayers of molybdenum and tungsten dichalcogenides* Phys. Rev. B 86, 115409 (2012)

[29] Xu Cui, En-Min Shih, Luis A. Jauregui, et al., *Low-Temperature Ohmic Contact to Monolayer MoS_2 by van der Waals Bonded Co/h-BN Electrodes*, Nano Lett., 2017, 17 (8), pp 4781–4786 DOI: 10.1021/acs.nanolett.7b01536

[30] Ryan J. Wu, Sagar Udyavara, Rui Ma, Yan Wang, Manish Chhowalla, Steven J. Koester, Matthew Neurock, K. Andre Mkhoyan *An Inside Look at the Ti-MoS2 Contact in Ultra-thin Field Effect Transistor with Atomic Resolution* arXiv:1807.01377 [cond-mat.mtrl-sci]

[31] R. Karplus and J. M. Luttinger, *Hall Effect in Ferromagnetics* Phys. Rev. 95, 1154 (1954).

[32] T. Jungwirth, Q. Niu, and A. H. MacDonald, *Anomalous Hall Effect in Ferromagnetic Semiconductors* Phys. Rev. Lett. 88, 207208 (2002).

[33] Sajedeh Manzeli, Dmitry Ovchinnikov, Diego Pasquier, Oleg V. Yazyev and Andras Kis *2D transition metal dichalcogenides* Nature Reviews, vol.2, 17033 doi:10.1038/natrevmats.2017.33

[34] A. Kumara and P.K. Ahluwalia *Electronic structure of transition metal dichalcogenides monolayers 1H-MX2 (M = Mo, W; X = S, Se, Te) from ab-initio theory: new direct band gap semiconductors* European Physical Journal B, (2012) 85: 186 DOI: 10.1140/epjb/e2012-30070-x

[35] Jose Ángel Silva-Guillén, Pablo San-Jose, and Rafael Roldán *Electronic Band Structure of Transition Metal Dichalcogenides from ab initio and Slater-Koster Tight-Binding Model*

[36] Chuan Zhao, Tenzin Norden, Peiyao Zhang, Puqin Zhao et al. *Enhanced valley splitting in monolayer WSe2 due to magnetic exchange field* Nature Nanotechnology, DOI: 10.1038/NNANO.2017.68, (2017)

[37] Huimin Su, Chengrong Wei, Aiying Deng, Dongmei Deng, Chunlei Yang, and Jun-Feng Dai, *Anomalous enhancement of valley polarization in multilayer WS_2 at room temperature* Nanoscale, 2017, 9, 5148, DOI: 10.1039/c7nr00554g

[38] Srivastava, A. et al. *Valley Zeeman effect in elementary optical excitations of monolayer WSe2.* Nature Physics, 11, 141–147 (2015).

[39] Jingshan Qi, Xiao Li, Qian Niu and Ji Feng *Giant and tunable valley degeneracy splitting in MoTe2* Physical Review B 92, 121403(R) (2015)

[40] Adrien Allain, Jiahao Kang, Kaustav Banerjee and Andras Kis *Electrical contacts to two-dimensional semiconductors* Nature Materials, 14 (2015) DOI: 10.1038/NMAT4452

[41] Sallen G. et al. *Robust optical emission polarization in MoS_2 monolayers through selective valley excitation*, Physical review, B86,081301(2012)

[42] Jones, A.M. et al. *Optical generation of excitonic valley coherence in monolayer WSe2.* Nature Nanotechnology, 8, 634–638 (2013)

[43] McDonnell, C. Smyth, C. L. Hinkle, R. M. Wallace, *MoS2–titanium contact interface reactions.* ACS Applied Materials and Interfaces 8, 8289-8294 (2016)

[44] Changsik Kim, Inyong Moon, Daeyeong Lee, et al. *Fermi Level Pinning at Electrical Metal Contacts of Monolayer Molybdenum Dichalcogenides* ACS Nano 2017, 11, 1588-1596, DOI: 10.1021/acsnano.6b07159

[45] C. Gong, L. Colombo, R. M. Wallace, K. Cho, *The unusual mechanism of partial Fermi level pinning at metal–MoS2 interfaces.* Nano Letters 14, 1714-1720 (2014).

[46] Dmitry Ovchinnikov, Adrien Allain, Ying-Sheng Huang, Dumitru Dumcenco, and Andras Kis *Electrical Transport Properties of Single-Layer WS2* vol.8, num. 8, 8174-8181 (2018)

[47] Florent Gauvin, Patrice Cousin, and Mathieu Robert *Improvement of the Interphase Between Basalt Fibers and Vinylester by Nano-Reinforced Post-Sizing* Fibers and Polymers 2015, Vol.16, No.2, 434-442

[48] D.R. Lide, *(Ed.) in Chemical Rubber Company handbook of chemistry and physics*, CRC Press, Boca Raton, Florida, USA, 81st edition, 2000

[49] J. A. Bearden and A. F. Burr, *Reevaluation of X-Ray Atomic Energy Levels*, Rev. Mod. Phys., 1967, 39, 125

[50] Darshana Wickramaratne, Ferdows Zahid, and Roger K. Lake *Electronic and thermoelectric properties of few-layer transition metal dichalcogenides*, THE JOURNAL OF CHEMICAL PHYSICS 140, 124710 (2014)

[51] Long-Cheng Tang, Li Zhao and Li-Zhi Guan, *7 Graphene/Polymer Composite Materials: Processing, Properties and Applications* In book: Advanced Composite Materials: Properties and Applications, 2017, DOI: 10.1515/9783110574432-007

[52] Ming-Yang Li, Chang-Hsiao Chen, Yumeng Shi1 and Lain-Jong Li, *Heterostructures based on two-dimensional layered materials and their potential applications*, Materials Today, Volume 19, Issue 6, July–August 2016, Pages 322-335 DOI: 10.1016/j.mattod.2015.11.003

[53] Jonathan Roberts, *Langmuir-Blodgett Deposition of 2D Materials for Unique Identification*, in book: Using Imperfect Semiconductor Systems for Unique Identification pp 63-88

[54] *Probes and Accessories*, 2011, Bruker

[55] *Principles of lock-in detection and the state of the art*, White Paper, Zurich Instruments, 2016

[56] Cedric Rolin, Enpu Kang, Jeong-Hwan Lee, *Charge carrier mobility in thin films of organic semiconductors by the gated van der Pauw method*, Nature Communications, 2017, DOI: 10.1038/ncomms14975

[57] van der Pauw, L.J. *A method of measuring specific resistivity and Hall effect of discs of arbitrary shape* (1958), Philips Research Reports, 13: 1–9.

[58] J. Holzl, F. K. Schulte, *Work functions of metals in Solid Surface Physics*, edited by G. Hohler (Springer-Verlag, Berlin, 1979), pp. 1–150

[59] Weiyi Wang, Yanwen Liu, Lei Tang, Yibo Jin, Tongtong Zhao, Faxian Xiu *Controllable Schottky Barriers between MoS_2 and Permalloy* Scientific Reports volume 4, Article number 6928 (2014)

[60] Seung Hwan Lee, Daeyeong Lee, Wan Sik Hwang, Euyheon Hwang, Debdeep Jena, and Won Jong Yoo *High-performance photocurrent generation from two-dimensional WS_2 field-effect transistors* Applied Physics Letters, n.104, 193113 (2014)

[61] I. Horcas, R. Fernandez, J.M. Gomez-Rodriguez, J. Colchero, J. Gomez-Herrero, A. M. Baro *WSXM: A software for scanning probe microscopy and a tool for nanotechnology* Rev. Sci. Instrum. 78, 013705 (2007)

[62] Lingming Yang, Kausik Majumdar, Han Liu, Yuchen Du, Heng Wu, Michael Hatzistergos, P. Y. Hung, Robert Tieckelmann, Wilman Tsai, Chris Hobbs, and Peide D. Ye *Chloride Molecular Doping Technique on 2D Materials: WS2 and MoS2* Nano Lett. 2014, 14, 6275-6280, dx.doi.org/10.1021/nl502603d

[63] Hafiz M. W. Khalil, Muhammad Farooq Khan, Jonghwa Eom, and Hwayong Noh *Highly Stable and Tunable Chemical Doping of Multilayer WS2 Field Effect Transistor: Reduction in Contact Resistance*, ACS Appl. Mater. Interfaces 2015, 7, 23589-23596, DOI: 10.1021/acsami.5b06825

[64] Liu, H.; Si, M.; Deng, Y.; Neal, A. T.; Du, Y.; Najmaei, S.; Ajayan, P. M.; Lou, J.; Ye, P. D. *Switching Mechanism in Single-Layer Molybdenum Disulfide Transistors: An Insight into Current Flow across Schottky Barriers.* ACS Nano 2013, 8 (1), 1031-1038.

[65] Wei, L.; Jiahao, K.; Wei, C.; Sarkar, D.; Khatami, Y.; Jena, D.; Banerjee, K. *High-Performance Few-Layer-MoS2 Field-Effect-Transistor with Record Low Contact-Resistance.* IEEE International Electron Devices Meeting (IEDM); IEEE: New York, 2013; p 19.14.11.

[66] *http://www.2dsemiconductors.com/p-type-ws-crystals/*

[67] S. Wu, J. S. Ross, G.-B. Liu, G. Aivazian, A. Jones, Z. Fei, W. Zhu, D. Xiao, W. Yao, D. Cobden and X. Xu, *Electrical tuning of valley magnetic moment through symmetry control in bilayer MoS2*, Nature Physics, 2013, 9(3), 149–153

[68] H. Zeng, J. Dai, W. Yao, D. Xiao and X. Cui, Valley polarization in MoS2 monolayers by optical pumping Nature Nanotechnology, 2012, 7(8), 490–493.

[69] P. K. Nayak, F. C. Lin, C. H. Yeh, J. S. Huang and P. W. Chiu, *Robust room temperature valley polarization in monolayer and bilayer WS2* Nanoscale, 2016, 8(11), 6035–6042